

FORMATION AND CONTROL OF HELICAL STATES IN 2D
GASES AND TOPOLOGICAL INSULATOR

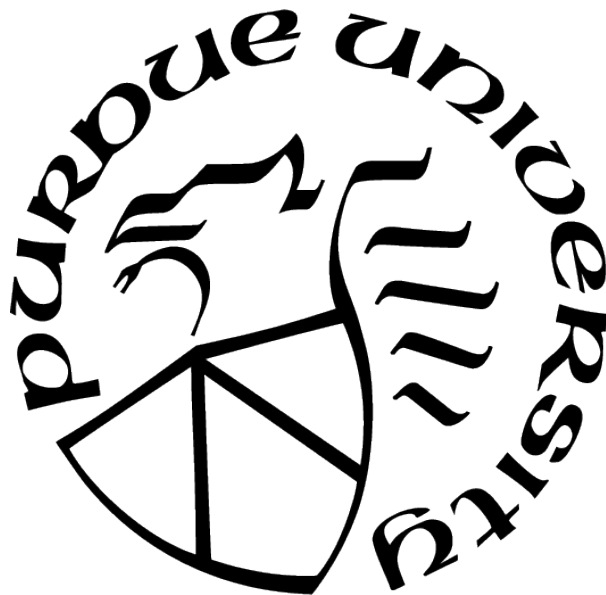
by
Ying Wang

A Dissertation

Submitted to the Faculty of Purdue University

In Partial Fulfillment of the Requirements for the degree of

Doctor of Philosophy



Department of Physics and Astronomy

West Lafayette, Indiana

August 2021

**THE PURDUE UNIVERSITY GRADUATE SCHOOL
STATEMENT OF COMMITTEE APPROVAL**

Dr. Leonid P. Rokhinson, Chair
Department of Physics and Astronomy

Dr. Gabor A. Csáthy
Department of Physics and Astronomy

Dr. Yuli Lyanda-Geller
Department of Physics and Astronomy

Dr. Haiyan Wang
Department of Materials Engineering

Approved by:
Dr. John P. Finley

To my parents, to my husband.

ACKNOWLEDGMENTS

First and foremost, I thank my advisor Professor Leonid Rokhinson, who gave me valuable research opportunities, and helped me a lot in understanding physics and building up experiments. I learned a lot from his hard work and enthusiasm for physics. His physics insight will continue influencing me over my life.

Besides, I would like to thank the rest of my committee members Professor Gabor Csáthy, Professor Yuli Lyanda-Geller, and Professor Haiyan Wang, for their time, interest, helpful suggestions, theoretical support, reviewing my thesis and sitting through the oral presentation.

Over the years, I have greatly benefited from many former and current members of the group. I acknowledge Dr. Tailung Wu, Dr. Aleksandr Kazakov, Dr. Zhong Wan, and Ananthesh Sundaresh, I can't overstate how much I have benefited from the insightful discussions with them. They were also directly involved in the research of this thesis. I would like to thank Dr. Zhong Wan and Ananthesh Sundaresh for their assistance during my measurements and device processing.

I want to thank Professor Loren Pfeiffer, Professor Ken West for growing the state-of-the-art 2DEGs wafers, without them I cannot work with well-developed quantum Hall effect regimes. Besides, I would like to thank Professor Xinyu Liu for growing heterostructure consisting of the metamagnetic insulator and topological insulator and helping me in understanding its corresponding magnetic properties.

I also want to acknowledge funding agencies which this work possible: the National Science Foundation under award DMR-1836758 and the Department of Energy under award DE-SC0008630. Polarized Nuclear Reflectometry experiments were performed at the Spallation Neutron Source, a DOE Office of Science User Facility operated by the Oak Ridge National Laboratory.

I appreciated the help from our graduate secretary Sandy Formica, our business secretary Redding Carla, our shipping and receiving clerk Howe Kasey, and building technician Keith Schmitter in Physics Department, they provide a strong backup on my research and academic life.

Lastly, I would like to thank my parents and husband, and for their selfless love, encouragement, trust, and support. Thank you!

TABLE OF CONTENTS

LIST OF TABLES	9
LIST OF FIGURES	10
ABSTRACT	13
1 INTRODUCTION	14
1.1 Heterostructures and a Two-Dimensional Electron Gas (2DEG)	14
1.2 Integer Quantum Hall Effect (IQHE)	16
1.3 Fractional quantum Hall effect (FQHE) and composite fermion (CF) theory	21
1.4 $\nu = 2/3$ edge states	24
1.5 Spin transition of $\nu = 2/3$ states in CF picture	25
1.6 Possible experimental platform to reveal Parafermions (PFs)	27
1.7 Electrons-Nuclei interactions	29
1.8 Skyrmions	31
1.9 Topological insulators	32
2 FORMATION AND CONTROL OF HELICAL STATES IN CHIRAL SYSTEM	35
2.1 Introduction	35
2.2 Wafers, devices and measurements	37
2.3 Devices characterization	38
2.3.1 Quality of 2DEGs	38
2.3.2 Spin transition within $\nu = 2/3$ plateau	40
2.3.3 Gate voltage and filling factor	40
2.4 Transport in the presence of a chiral channel	41
2.5 Formation of helical domain walls at $\nu = 2/3$	43
2.5.1 Field dependence of helical domain wall	43
2.5.2 Temperature dependence of helical domain wall	44
2.5.3 Length dependence of helical domain wall	46
2.6 Transport study of the Domain wall in $\nu = 2/3$ plateau	46

2.7	Spin pumping with a dc current	51
2.8	Transport discussion of Quasi-Corbino (qC) device	59
2.9	Conclusions	65
3	CONTROL OF HELICAL STATES IN TOPOLOGICAL INSULATOR	67
3.1	Introduction	67
3.2	Material growth and structural characterization.	69
3.3	Magnetic properties	78
3.3.1	Magnetization studies of SB: <i>EuSe</i> (111) and SD: <i>EuSe</i> (001)/ <i>Bi₂Se₃</i>	78
3.3.2	Comparison of magnetic phase diagram and structural characteriza- tion between <i>EuSe</i> (001)/ <i>Bi₂Se₃</i> samples SD1 and SD3	86
3.3.3	Magnetization studies of SC and SE: <i>Bi₂Se₃</i> / <i>EuSe</i> (111)	87
3.4	Spin-polarized neutron reflectivity (PNR) of <i>EuSe</i> (001)/ <i>Bi₂Se₃</i> /Sapphire sam- ples	89
3.5	Transport	92
3.5.1	Characterization of <i>Bi₂Se₃</i> thin film from samples SD1 and SD3	92
3.5.2	Magneto-resistance of <i>EuSe</i> (001)/ <i>Bi₂Se₃</i> without hysteresis in small field range below 300mT for both B_{\parallel} and B_{\perp}	97
3.5.3	Modulation of magneto-conductance of <i>EuSe</i> (001)/ <i>Bi₂Se₃</i>	98
3.6	Conclusions	100
4	SUMMARY AND PERSPECTIVES	102
4.1	Transport in helical Luttinger liquids in the fractional quantum Hall regime	102
4.2	Experimental investigation of parafermion in FQHE regime	102
4.3	Experimental investigation of the superconducting contacts in the IQHE regime	103
4.4	Studies of possible formation of a fractional skyrmion crystal near filling factor $\nu = 2/3$	103
4.5	Magnetic and transport studies of a metamagnetic insulator/topological in- sulator system	105
	REFERENCES	107

A LIST OF QUANTUM WELL (QW) WAFERS USED IN THIS THESIS	127
B DETAILED PROCESS OF DEVICE FABRICATION FOR WAFER A (LE40) . .	128
C DETAILED PROCESS OF DEVICE FABRICATION FOR <i>EuSe/Bi₂Se₃/Sapphire</i>	131
VITA	133

LIST OF TABLES

1.1	Properties of the three types of nuclei in <i>GaAs</i>	29
3.1	List of studied <i>EuSe</i> films.	70
3.2	Density and mobility of 20nm thick <i>Bi₂Se₃</i> thin film.	92
A.1	List of samples used in this thesis.	127

LIST OF FIGURES

1.1	Comparison between conventional heterostructure and inverted single interface heterojunction.	15
1.2	Landau levels.	18
1.3	Shubnikov-de Hass (SdH) oscillations.	19
1.4	Edge modes.	20
1.5	The discovery of FQHE.	21
1.6	Schematic illustration of the composite Fermion model.	23
1.7	Schematic illustration of the edge state construction in $\nu = 2/3$	25
1.8	Spin-split CF Landau levels for $\nu = 2/3$	26
1.9	Possible platform to realize parafermions.	28
1.10	Skyrmions.	32
2.1	A typical Hall bar device with helical domain walls (hDWs) length of $L = 7\mu m$	37
2.2	Magneto-resistance R_{xx} of a 2D gas as a function of magnetic field.	39
2.3	Magneto-resistance R_{xx} of a 2D gas as a function of gate voltage.	40
2.4	Chiral channels in integer quantum Hall effect (IQHE) and fractional quantum Hall effect (FQHE) regimes.	41
2.5	Formation of helical domain walls at $\nu = 2/3$	42
2.6	Stability of helical domain wall (hDW) resistance R_{34} under magnetic field inversion.	44
2.7	Evolution of spin transition boundaries with magnetic field.	45
2.8	Activation gap.	46
2.9	Resistance R_{34} as a function of filling factors for other gates boundary lengths	47
2.10	Conduction of helical domain walls (hDWs).	48
2.11	Schematic representation of currents for a helical domain wall system in Luttinger liquid theory.	49
2.12	Schematic diagrams of spin pumping.	51
2.13	Density relaxation.	53
2.14	Shift of spin transition boundary.	54
2.15	Electron spin flip and nuclear-electron hyperfine interaction.	55
2.16	Overhauser field change with nuclear-electron hyperfine interaction only.	56

2.17	Schematic diagram of spin wave picture.	57
2.18	Sign of angular momentum change of spin wave.	58
2.19	Photography of a quasi-Corbino (qC) device.	60
2.20	Formation of chiral edge channel in gated quasi-Corbino (qC) device.	61
2.21	Gate and field dependence of spin transition around $\nu = 2/3$ in a quasi-Corbino (qC) device.	62
2.22	Helical channel measurement at $\nu = 2/3$ for quasi-Corbino (qC) geometry.	63
2.23	Length dependence of conductance of the helical channel for quasi-Corbino (qC) geometry	64
3.1	Structural and magnetic orderings of <i>EuSe</i>	69
3.2	Surface roughness of <i>EuSe</i> on different substrates.	71
3.3	RHEED patterns of <i>EuSe</i> films grown with various crystalline orientations.	72
3.4	High-resolution XRD $\omega - 2\theta$ scan for (001) growth <i>EuSe</i>	73
3.5	High-resolution XRD $\omega - 2\theta$ scan for (001) mixed with (111) growth <i>EuSe</i>	74
3.6	Structural Characterization of <i>EuSe</i> growth on different substrates.	76
3.7	Structural Structural characterization of <i>EuSe</i> growth on <i>Bi₂Se₃</i>	77
3.8	Temperature dependence of magnetic susceptibilities of <i>EuSe</i>	79
3.9	Magnetic moment per <i>Eu²⁺</i> ion.	80
3.10	Normalized magnetic moment loops for <i>EuSe</i> (111)/ <i>BaF₂</i> (111).	81
3.11	Magnetic properties of <i>EuSe</i> (111).	82
3.12	Magnetic phase diagram of <i>EuSe</i> (111).	83
3.13	Magnetic phase diagram of <i>EuSe</i> (001)/ <i>Bi₂Se₃</i>	84
3.14	Analysis of higher order terms in susceptibility for <i>EuSe</i> (001)/ <i>Bi₂Se₃</i>	85
3.15	Comparison of magnetic and structural characterizations between <i>EuSe</i> (001)/ <i>Bi₂Se₃</i> samples.	86
3.16	Magnetic properties of <i>Bi₂Se₃</i> / <i>EuSe</i> (111).	87
3.17	Magnetic phase diagrams of <i>Bi₂Se₃</i> / <i>EuSe</i> (111).	88
3.18	Comparison of in-plane differential magnetic susceptibilities between <i>EuSe</i> (111) and <i>Bi₂Se₃</i> / <i>EuSe</i> (111)	89
3.19	Polarized neutron reflectometry (PNR) results for <i>EuSe</i> (001)/ <i>Bi₂Se₃</i>	90
3.20	Magnetization comparison between PNR and SQUID measurements.	91

3.21	Transport characterization of Bi_2Se_3 for $EuSe(001)/Bi_2Se_3$	93
3.22	Weak anti-localization (WAL) of Bi_2Se_3 for $EuSe(001)/Bi_2Se_3$	94
3.23	Linear transverse magneto-resistance for $EuSe(001)/Bi_2Se_3$	95
3.24	Cross field B_{cross} for $EuSe(001)/Bi_2Se_3$	96
3.25	Longitude resistance below 300mT for $EuSe(001)/Bi_2Se_3$	97
3.26	Multiple domains in a macroscopic sample of $EuSe(001)/Bi_2Se_3$	98
3.27	Single domain in a microscopic sample of $EuSe(001)/Bi_2Se_3$	99
3.28	Temperature dependence of single domain for $EuSe(001)/Bi_2Se_3$	100
4.1	Design of future device for further studies of spin pumping.	104
B.1	Device fabrication of wafer A (LE40).	130
B.2	Device fabrication of wafer A (LE40).	130
C.1	Device fabrication of $EuSe(001)/Bi_2Se_3/Sapphire$	132

ABSTRACT

It has been realized that a p-wave order parameter can emerge in a synthetic superconductor constructed from a semiconductor and an s-wave superconductor, provided that fermion doubling is removed [1], [2]. In one dimension, the required electron spectrum consists of two counter-propagating modes with opposite spin orientations, so-called helical channels. Helical channels can be realized in nanowires with spin-orbit interactions in the presence of magnetic field [3], [4], topological insulators [5], at the edges of the quantum spin Hall system [6], or in the integer and fractional quantum Hall effect regimes [7]–[10]. This thesis will discuss the formation and control of helical states in different systems.

The thesis will begin with a brief review of the quantum Hall effect and fractional quantum Hall effect, the theoretical and experimental study of $\nu = 2/3$ edge states, and spin polarization of the $\nu = 2/3$ state. Chapter 2 will discuss the investigation of transport properties of helical domain walls between incompressible spin-polarized $\nu = 2/3$ and spin unpolarized $\nu = 2/3$. Experimentally, the current carried by helical domain walls is found to be substantially smaller than the prediction of the naive model. The experimental results are compared with detailed Luttinger liquid theory and it is showed that inclusion of spin non-conserving tunneling process reconciles theory with experiment.

Chapter 3 will discuss the magnetic and transport properties of $EuSe/Bi_2Se_3$, which may enable a control of helical states related to topological surface states in topological insulators by using magnetic proximity effect. A metamagnetic insulator $EuSe$, which consists of various magnetic phases, is proven to grow on Bi_2Se_3 in (001) direction. The magnetic and transport results indicate that the interfacial exchange between $EuSe$ and Bi_2Se_3 is antiferromagnetic, which may modify the surface states and result in even more nontrivial physics that are not observed before.

1. INTRODUCTION

The first system discussed in this thesis for forming helical channels is the 2DEG in fractional quantum Hall effect (FQHE) regime. Some basic concepts of the quantum Hall effect (QHE) and a two-dimensional electron gas system (2DEG) are introduced in this chapter. The first section discusses 2DEG in heterostructures. Section 2 reviews the quantum-mechanical transport characteristics of a 2DEG subjected to electric and magnetic fields and presents Landau Levels (LLs), quantum Hall effect (QHE), and the formation of edge states. The FQHE and the composite fermion (CF) theory are discussed in section 3. Sections 4 and 5 focus on the $\nu = 2/3$ spin transition. This section also includes an introduction to the transport properties of the longitudinal resistance peak, which relates to a spin transition. Section 6 briefly discusses an experimental platform to realize parafermions with $\nu = 2/3$ spin-polarized and unpolarized states. Section 7 and 8 discuss the spin degree of freedom in the FQHE including electron-nuclear interactions and formation of skyrmions. The last section will introduce another system - a topological insulator (TI) - where helical states related to topological surface states can be controlled.

1.1 Heterostructures and a Two-Dimensional Electron Gas (2DEG)

In a 2DEG system, electrons are free to move within two dimensions (2D) but are confined in the dimension perpendicular to this 2D plane. This system is a fundamental low-dimensional system [11] for condensed matter physics and many critical physical phenomena, such as integral and the fractional quantum Hall effects (IQHE and FQHE), which were discovered in high-quality 2DEG [12], [13]. The two-dimensional behaviors of 2DEG are observed in materials like *Si - MOSFETS* and heterojunctions of III-V compounds such as *GaAs/Ga_{1-x}Al_xAs* and 2-dimensional van-der-Waals materials. These materials or heterostructures with atomic precision can usually be grown using molecular-beam epitaxy (MBE) or metal-organic chemical vapor deposition (MOCVD).

A record of high electron mobility $\mu \sim 35 \times 10^6 \text{cm}^2(\text{Vs})$ with a mean free path of $\sim 300 \mu\text{m}$ was reported in an AlGaAs/GaAs 2DEG at $T < 1\text{K}$ without illumination [14]. The difference in lattice constant between GaAs and AlAs is less than 0.15%. This small

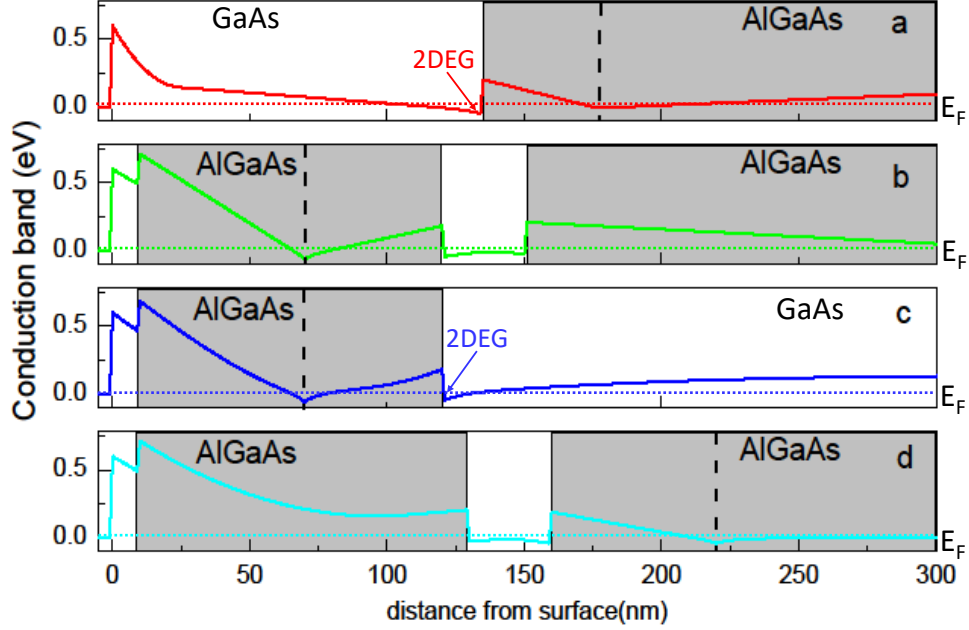


Figure 1.1. Comparison between conventional heterostructure and inverted single interface heterojunction: Conduction band profile is plotted for (a) inverted single interface heterojunction used in our experiments and (b) typical modulation-doped quantum well, (c) single heterojunction, and (d) inverted quantum well. Dash lines indicate positions of modulation doping. Short dash lines indicate positions of Fermi energy. The figure is adapted from ref. [15].

mismatch can result in a multi-layers sample of GaAs/AlGaAs without much strain and with high electron mobility.

In our work, an inverted heterostructure, where the AlGaAs barrier with modulation doping is placed below the 2DEG as shown in Figure 1.1a, was used for increasing the contact area of side contacts (130 nm in our inverted heterostructure (Figure 1.1a) vs. 20 – 30 nm in typical quantum wells (Figure 1.1bcd)). The carrier density n and mobility μ of our sample are increased at cryogenic temperatures by shining light using the persistent photoconductivity (PPC) effect. The carrier density of 2DEG can be tuned by a metal gate deposited on the oxide layer grown on the top of the sample within the $0.5 \cdot 10^{11} \text{cm}^{-2}$ to $0.9 \cdot 10^{11} \text{cm}^{-2}$ range.

1.2 Integer Quantum Hall Effect (IQHE)

The Hamiltonian for an electron of a two-dimensional system in the presence of magnetic field $\hat{B} = \nabla \times \hat{A}$ within Landau gauge $\hat{A} = xB\hat{y}$ is:

$$H = \frac{(\hat{p} + e\hat{A})^2}{2m^*} + V(x, y) = \frac{1}{2m^*}\hat{p}_x^2 + \frac{1}{2m^*}(\hat{p}_y - eB\hat{x})^2 + V(x, y) + \text{disorder}, \quad (1.1)$$

where \hat{p} is the momentum operator $\frac{i}{\hbar}\nabla$ and \hat{A} is the electromagnetic vector potential and $V(x, y)$ is a boundary potential function. When sample is far away from the boundary ($V(x, y) = 0$), an wave function is $\psi_k(x, y) = e^{iky}f_k(x)$, where k is wave vector. The Hamiltonian can be rewritten as a Hamiltonian for a harmonic oscillator:

$$H_k = \frac{1}{2m^*}\hat{p}_x^2 + \frac{m^*\omega_c^2(x + kl_B^2)^2}{2}, \quad (1.2)$$

where $\omega_c = \frac{eB}{m^*}$ is the cyclotron energy, m^* is the effective mass of the electrons ($m^* = 0.067m_0$ for GaAs) and B is the magnetic field strength applied perpendicular to sample plane and $l_B = \sqrt{\frac{\hbar}{eB}}$ is magnetic length. The corresponding solution for eigenvalues (energy levels) and wave function are:

$$E_{N,k} = \hbar\omega_c(N + \frac{1}{2}), \quad (1.3)$$

$$\psi_k(x, y) \propto H_{N-1}\left(\frac{x - x_k}{l_B}\right) \cdot e^{-\frac{1}{2}\left(\frac{x - x_k}{l_B}\right)^2} \cdot e^{iky}, \quad (1.4)$$

where n is a positive integer, $x_k = -k(l_B)^2$ and $H_{N-1}(x)$ is an integer Hermite function. The energy of the electron here depends only on N but not on k , which indicates degenerate states with different k for the same energy level. The density of states is shown in Figure 1.2b. The number of states in each Landau level is $n_L = \frac{B}{h/e}$, where $\frac{h}{e}$ is a flux quanta. Filling factor $\nu = n/n_L$, where n is the carrier density, indicates the number of filled Landau levels. In reality, the broadening of the Landau level is the result of both temperature and disorder, as shown in Figure 1.2b. There also can be splitting of Landau levels due to the Zeeman effect. At $B = 0$, the two spin levels are degenerate. With Zeeman energy term, $E_N = \hbar\omega_c(N + \frac{1}{2}) + sg^*\mu_B B$, where g^* is effective g factor ($g^* \approx -0.44$ for GaAs), μ_B is Bohr

magneton and s is spin quantum number ($\pm\frac{1}{2}$ for electron). As B increases, the density of state (DOS) at Fermi energy (E_F) varies, as shown in Figure 1.2c, and the resistance oscillates periodically in $1/B$. This phenomenon is known as Shubnikov-de Hass (SdH) oscillations, as shown in Figure 1.3. If using the corresponding magnetic fields B_i and B_{i+1} for the consecutive minima in ρ_{xx} , the carrier density can be calculated as $n = \frac{e}{h} \frac{1}{\frac{1}{B_i} - \frac{1}{B_{i+1}}}$. The amplitude of SdH oscillations can be described by the Dingle formula [16]:

$$\frac{R_{xx}(B)}{R_{xx}(B=0)} \approx 1 + 2 \cdot \cos\left(\frac{2\pi E_F}{\hbar\omega_c} - \pi\right) \cdot e^{\frac{-\pi}{\omega_c\tau_q}} \cdot \frac{\xi}{\sinh(\xi)} \cdot \cos\left(2\pi\left(\frac{g\mu_B B}{2\hbar\omega_c}\right)\right), \quad (1.5)$$

where B is magnetic field, $\omega_c = \frac{eB}{m^*}$ is cyclotron frequency, τ_q is the quantum lifetime, $\xi = \frac{2\pi^2 k_B T}{\hbar\omega_c}$, and n is the carrier density. Scattering leads to a partial lifting of Landau levels degeneracy and results in a Lorentzian broadening of the Landau levels with a full width at half maximum $\Gamma = \frac{\hbar}{2\tau_q}$. The amplitude of the oscillations in R_{xx} is dampened depending on the ratio $\Gamma/\hbar\omega_c$. The $\frac{\xi}{\sinh(\xi)}$ term takes thermal broadening into account. The \cos term incorporates the effect of the Zeeman splitting.

When magnetic field is high, and ν Landau levels are filled, a single particle picture in quantum mechanics indicates that the current in the x-direction (electric field E direction) is $I_x = -\frac{e}{m} \sum_{N=1}^{\nu} \sum_k \langle \psi_{N,k} | -i\hbar \frac{\partial}{\partial x} | \psi_{N,k} \rangle = 0$ and the current in the y-direction is $I_y = -\frac{e}{m} \sum_{N=1}^{\nu} \sum_k \langle \psi_{N,k} | -i\hbar \frac{\partial}{\partial y} + exB | \psi_{N,k} \rangle = -\frac{e}{m} \sum_{N=1}^{\nu} \sum_k \langle \psi_{N,k} | \hbar k + exB | \psi_{N,k} \rangle = e\nu \sum_k \frac{E}{B} = e\nu \frac{AB}{h/e} \frac{E}{B}$. For 2DEG in a magnetic field, the resistivity $\hat{\rho}$ and conductivity $\hat{\sigma}$ are 2×2 tensors:

$$\hat{\rho} = \begin{bmatrix} \rho_{xx} & \rho_{xy} \\ -\rho_{xy} & \rho_{xx} \end{bmatrix}; \hat{\sigma} = \begin{bmatrix} \sigma_{xx} & \sigma_{xy} \\ -\sigma_{xy} & \sigma_{xx} \end{bmatrix} = \hat{\rho}^{-1}$$

Therefore, $\sigma_{xx} = 0$ ($\rho_{xx} = \frac{\sigma_{xx}}{\sigma_{xx}^2 + \sigma_{xy}^2} = 0$) and $\sigma_{xy} = \nu \frac{e^2}{h}$ ($\rho_{xy} = \nu^{-1} \frac{h}{e^2}$), quantized values observed in integer quantum Hall effect (IQHE). Quantized Hall resistance can be explained by introducing the edge states picture [18]. With a finite sample size, there will be a confining potential at the edges of the sample. The number of edge states in the sample will be determined by the number of Landau levels below the Fermi energy E_F .

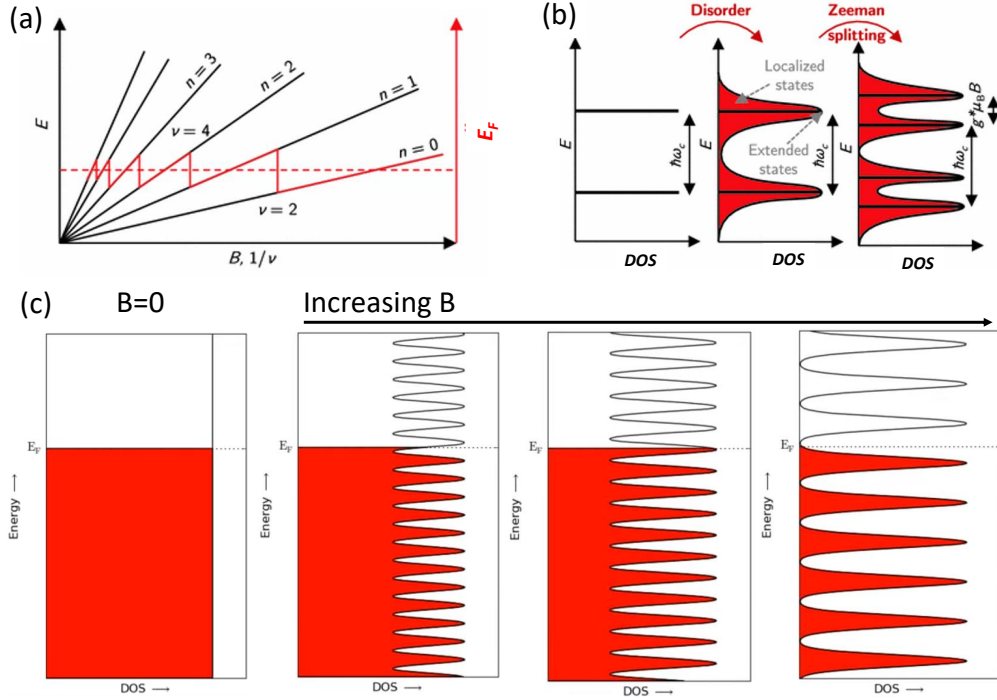


Figure 1.2. Landau levels: (a) Energy vs. magnetic field (B) spectrum and periodically change of Fermi energy. (b) Effect of disorder and Zeeman splitting: extended states are allowed in the center of each Landau level, while the states in the tails of each Landau level are localized. (c) Filled Landau levels with increasing magnetic field. The figures are adapted from ref. [17].

Now only the confining potential $V(x)$ along x -direction is considered. $V(x)$ rises when it is close to the edge of the sample, as shown in Figure 1.4a. The energy of Landau levels becomes:

$$E_{N,k_y} = \left(N + \frac{1}{2}\right)\hbar\omega_c + \langle \psi_{N,k_y} | V(x) | \psi_{N,k_y} \rangle. \quad (1.6)$$

The effect of the confining potential is to lift the energy of the Landau levels towards the edge, forcing them to cross the Fermi energy (E_F) at some finite distance from the edge. When E_F is in the middle of two Landau levels, one will find lines of non-vanishing density of states where the Landau levels cross the E_F along the edge. Near the edge $V(x) \approx V(X) + \frac{\partial V(X)}{\partial X}(x - X)$, then the energy can be written as:

$$E_{N,k_y} \approx \left(N + \frac{1}{2}\right)\hbar\omega_c + V(X(k_y)) \quad (1.7)$$

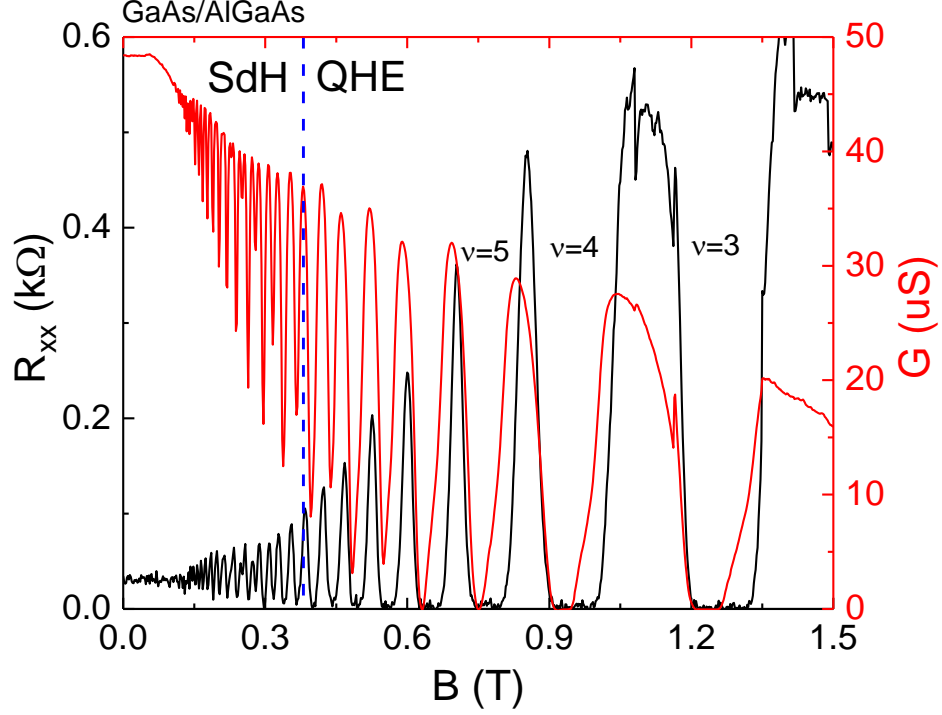


Figure 1.3. Longitudinal resistance and conductance as a function of magnetic field B : Shubnikov-de Hass (SdH) oscillations and IQHE are observed in longitudinal resistance or conductance measurement from our inverted heterostructured sample.

and the drift velocity is

$$v_{N,k_y} = \frac{1}{\hbar} \frac{\partial E_{N,k_y}}{\partial k_y} = \frac{1}{\hbar} \frac{\partial V(X(k_y))}{\partial k_y} = \frac{1}{\hbar} \frac{\partial U(X(k_y))}{\partial X} \frac{\partial X}{\partial k_y} = \frac{-1}{eB} \frac{\partial V(X)}{\partial X}. \quad (1.8)$$

The direction of v_{n,k_y} ($v_{n,k_y} > 0$ or < 0) depends on the sign of $\frac{\partial V(X)}{\partial X}$. Since the sign for $\frac{\partial V(X)}{\partial X}$ at the opposite mesa boundaries is opposite, electrons move along the two mesa boundaries in opposite direction. Now a potential difference ($E_{F_s} - E_{F_d} = \Delta V(X) = -eV$) between source and drain or between the two sides of the sample is introduced, as shown in figure 1.4 b. This means that more states on the right-hand edge are filled than on the left-hand edge. To compute the resulting current, all filled states are summed over. The 1-D

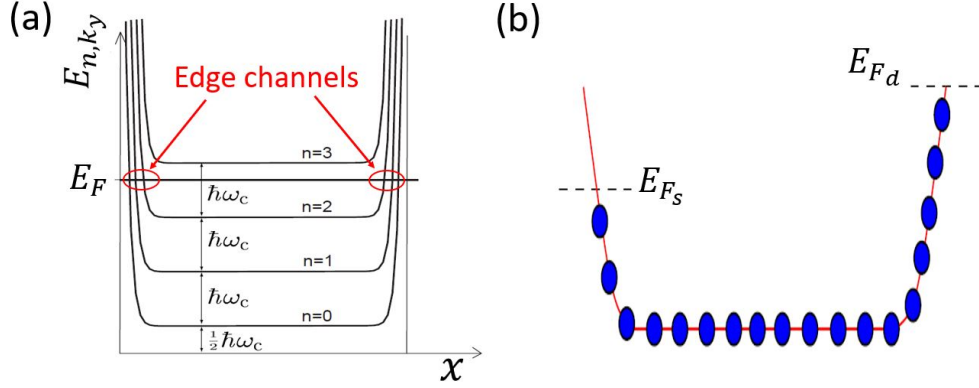


Figure 1.4. Edge modes: (a) Edge channels and confining potential.(b) Potential difference on two edges. The figures are taken from reference [19].

density of states of the edge is $\delta n_e = \frac{1}{2\pi} \Delta k = \frac{1}{2\pi} \left(\frac{1}{l_B}\right)^2 \Delta x = \frac{1}{2\pi} \frac{eB}{\hbar} \Delta x$ and then edge current is:

$$I_y = -\delta n_e e v_{n,k_y} = -e \frac{1}{2\pi} \frac{eB}{\hbar} \Delta x \frac{-1}{eB} \frac{\partial V(X)}{\partial X} = \frac{e}{2\pi\hbar} eV = \frac{e^2}{h} V = \sigma_{xy} V. \quad (1.9)$$

Therefore, a single channel carries a quantized conductance of e^2/h . The edge states transports were widely studied using Hall-bar geometry in the GaAs 2DEG system. Transport complex geometries in the IQHE regime can be modeled using the Landauer-Büttiker formalism [18]. The voltage and current flow in the edge states follow three simple rules: 1. The potential of the downstream channel remains the same unless it is equilibrated by the contacts. 2. Each edge state in IQHE has a conductance of $g = e^2/h$. 3. The conservation of total charge.

An appearance of quantized plateaus in Hall resistance R_{xy} and zero longitude resistance R_{xx} can be explained by the presence of disorder. Some states at the tails of the Landau levels are localized by disorder while the current-carrying extended states are in the center of each Landau level [20]–[22], as shown in Figure 1.2b. If the magnetic field is decreased when all the extended states are filled in a given Landau level, the localized states begin to be populated instead of jumping up to the next Landau level. Since the localized states cannot contribute to the conduction, the conductivity does not change over a range of magnetic fields.

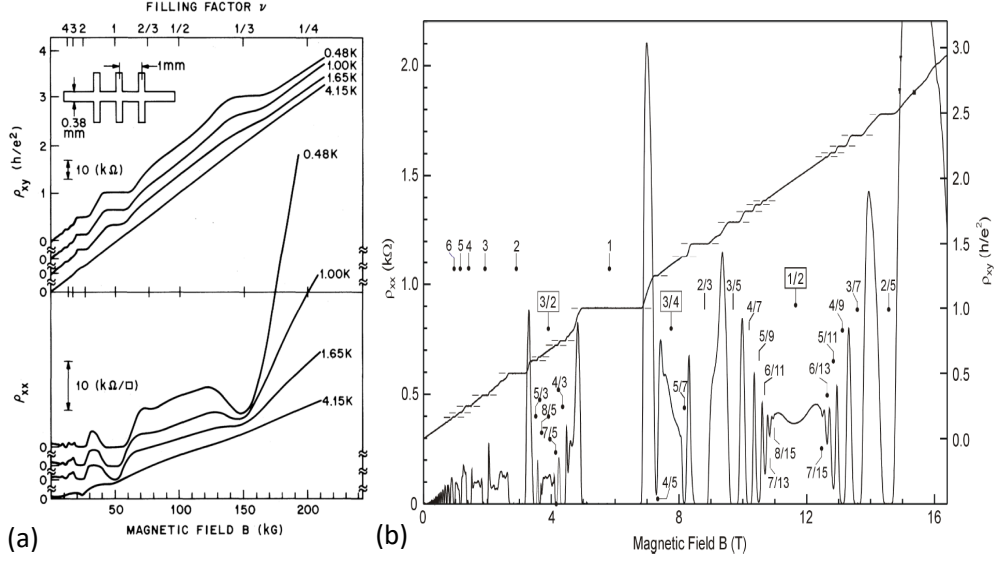


Figure 1.5. The discovery of FQHE. (a) The fractional quantum Hall effect (FQHE) was first observed in an AlGaAs/GaAs heterostructure using a Hall-bar geometry. The Hall resistance shows plateaus in ρ_{xy} quantized to the values of $\frac{3h}{e^2}$ accompanied by a reduced ρ_{xx} at $\nu = 1/3$. Figure was taken from reference [23]. (b) A large number of fractional fillings were observed. These fractional quantum Hall states are caused by Coulomb interactions between the electrons in a strongly correlated system. The figure is adapted from ref. [24].

1.3 Fractional quantum Hall effect (FQHE) and composite fermion (CF) theory

The fractional quantum Hall effect (FQHE) was first observed in an AlGaAs/GaAs heterostructure by D. Tsui, H. Störmer and A. Gossard [23] (Figure 1.5a) shortly after the discovery of IQHE. The ρ_{xy} shows quantized plateau to the value of $\frac{3h}{e^2}$ accompanied by a reduced ρ_{xx} at $\nu = 1/3$. After that, a large number of fractional quantum Hall states with different fractional filling factors were discovered. Figure 1.5b shows a typical plot of the longitudinal resistivity and the Hall resistance as a function of the magnetic field for a high mobility sample. This curve displays the plateaus in ρ_{xy} quantized to values of h/fe^2 with a vanishing ρ_{xx} , where f is an exact rational value with an odd denominator. All of these fractional states are characterized by having odd denominators, being symmetric around $\nu = 1/2$, having a larger gap for small denominators, and occurring only in very high mobility samples at low temperatures (few mK). The discovery of the fractional quantum

Hall states was unexpected since, according to the IQHE picture, there should be no energy gap below $\nu = 1$. However, the theory for the IQHE excludes electron-electron interactions, which are essential for the FQHE. Now the Hamiltonian must include Coulomb energy that results in correlation effects:

$$H = \frac{(\hat{p} + e\hat{A})^2}{2m^*} + \frac{e^2}{4\pi\epsilon_0} \sum_{j < k} \frac{1}{|r_j - r_k|} + \sum_j V(r_j) + g\mu_B B \cdot S, \quad (1.10)$$

Here the second term on the right side represents the Coulomb interaction energy, and the third term indicates the positive background and disorder potential, and the last term is Zeeman energy [25], [26]. Laughlin's proposal of a trial wave function proved to be very successful in describing the strong electron correlations for the $\nu = 1/m$ FQH ground states with m being an odd integer [27], [28]. The expression of the trial wave function is:

$$\Psi_{1/m} = \prod_{i < j} (z_i - z_j)^m \cdot e^{-\frac{1}{4l_B^2} \sum_i |z_i|^2}, \quad (1.11)$$

where $z_{i,j}$ is the position of an electron denoted as a complex number and $m = 2p + 1$ is an odd integer, which forces the orbital part of the wave function to be anti-symmetric and the spin part to be symmetric. The first part ($\prod_{i < j} (z_i - z_j)^m$), which is also called Jastrow factor, includes the Pauli exclusion. When two electrons come together, the Jastrow factor vanishes with a zero of order m . The exponential factor decreases quickly whenever electrons get too far from the origin, thereby keeping the electrons as far as possible. Also, this wave function satisfied the desired filling fraction $\nu = 1/m$. Another assumption here is that spins are fully polarized when electrons occupying the lowest spin-split LL. This assumption holds for $\nu = 1/m$ FQH ground states and depends on the effective g factor. At other fractional filling factors, partial or zero polarization ground states do exist. Laughlin's approach only accounts for the $\nu = 1/m$ FQH ground states.

Because of the apparent similarity of the experimental results between IQHE and FQHE, an instructive theory was developed by Jain [29] to understand the FQHE states in the lowest Landau level (LLL). In this theory, an even number ($2p$) of vortices is bound to each electron, forming a new quasiparticle named composite fermion (CF) after vortex attachment

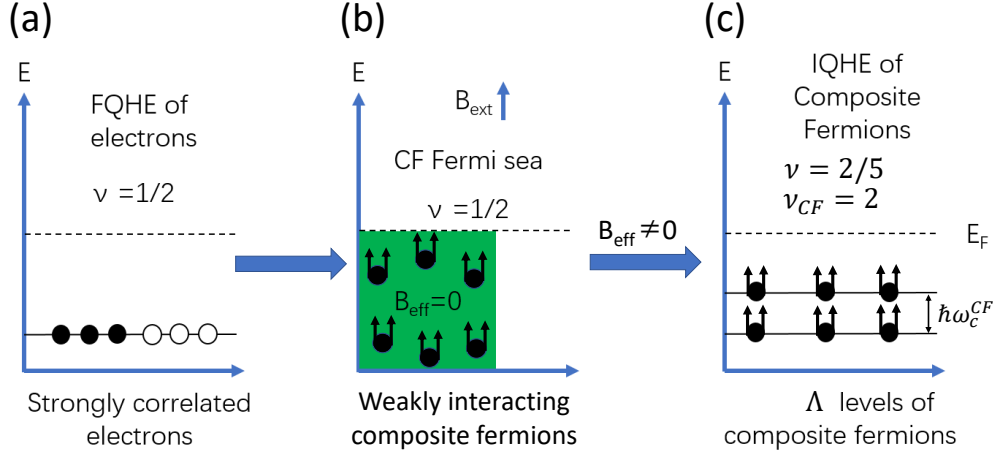


Figure 1.6. Schematic illustration of the composite Fermion model: Half filled Landau level in the picture of IQHE (a) is transformed into a composite Fermion sea (b) after the flux (black arrows) attachment transformation. (c) When $B_{\text{eff}} \neq 0$, Λ levels of composite Fermions are formed, a resemblance of the case in IQHE. The figure is adapted from ref. [24].

transformation. In a simplified picture, $2p$ point flux quanta are attached to an electron. The electrons effectively avoid each other by attaching to these flux quanta. In this way, a strongly correlated electron system is mapped onto a weakly interacting system of CFs [26], [29], [30]. At $\nu = 1/2$, $p = 1$ and for this special case each electron carries exactly 2 flux quanta. The net phase for a closed-loop by a CF enclosing an area A is $2\pi \frac{AB_{\text{eff}}}{\phi_0}$ and it consists of Aharonov-Bohm phase of electron, which is $2\pi \frac{AB_{\text{ext}}}{\phi_0}$, and Berry phase of the 2 vortices bound to CF, which is $2\pi \cdot 2nA$. Here B_{ext} is the external magnetic field, B_{eff} is the effective magnetic field, n is the electron density, and $\phi_0 = \frac{h}{e}$ is the magnetic flux quanta. So the reduced effective magnetic field B_{eff} that CFs are experiencing is:

$$B_{\text{eff}} = B_{\text{ext}} - 2n\phi_0 \quad (1.12)$$

When $\nu = 1/2$, $B_{\text{eff}} = 0$ and CFs form a Fermi sea [31], [32]. The Fermi wave vector is given by: $k_{CF} = \sqrt{4\pi n}$ [33]. Note that B_{eff} can be either negative or positive when $\nu > 1/2$ or $\nu < 1/2$. The filling factor for a composite fermion is:

$$\nu = \frac{\nu_{CF}}{2\nu_{CF} \pm 1} \quad (1.13)$$

where the \pm sign in the denominator indicates the direction of B_{eff} in respect to B_{ext} . For instance, $\nu = 2/3$ and $\nu = 2/5$ is the case when $\nu_{CF} = 2$ with negative and positive B_{eff} respectively. Now, FQHE for electrons can be viewed as IQHE for composite fermions when ν is away from $1/2$ and $B_{\text{eff}} \neq 0$ as shown in Figure 1.6. Similarly, CFs occupy Λ levels separated by an energy gap $\Delta E_{CF} = \gamma E_C \propto \sqrt{B}$, which, in analogy with electrons, can be expressed as $\Delta E_{CF} = \hbar\omega_{CF} = \hbar \frac{eB_{\text{eff}}}{m_{CF}}$, where a field-dependent effective mass m_{CF} is introduced.

1.4 $\nu = 2/3$ edge states

Edge state of $\nu = \frac{2}{3}$ is very complicated and was predicted to have two counter-propagating modes which are downstream $\nu = 1$ charge mode and upstream $\nu = -1/3$ charge mode [34] (see Figure 1.7a). A two-terminal conductance in this case is expected to be $\frac{4e^2}{3h}$, which contradicts experimentally observed $\frac{2e^2}{3h}$ [35], [36]. Later, it was realized that $\nu = 2/3$ charge mode is accompanied by an upstream neutral mode [37], see Figure 1.7b, signatures of an upstream neutral mode has been reported in a number of experiments [35]–[43]. Another interpretation of $\nu = 2/3$ is two co-propagating $\nu = 1/3$ modes [44], see Figure 1.7c, and some experimental observations [45], [46] also indicated this possibility. In general, highly correlated $\nu = 2/3$ state exhibits rich physics beyond an oversimplified model of $\nu^* = 2$ integer QHE for weakly interacting composite fermions and includes observation of upstream neutral modes [39], [41]–[43], short-range upstream charge modes [47], and a crossover from $e^* = 1/3$ to $e^* = 2/3$ charge excitations in shot noise measurements [46].

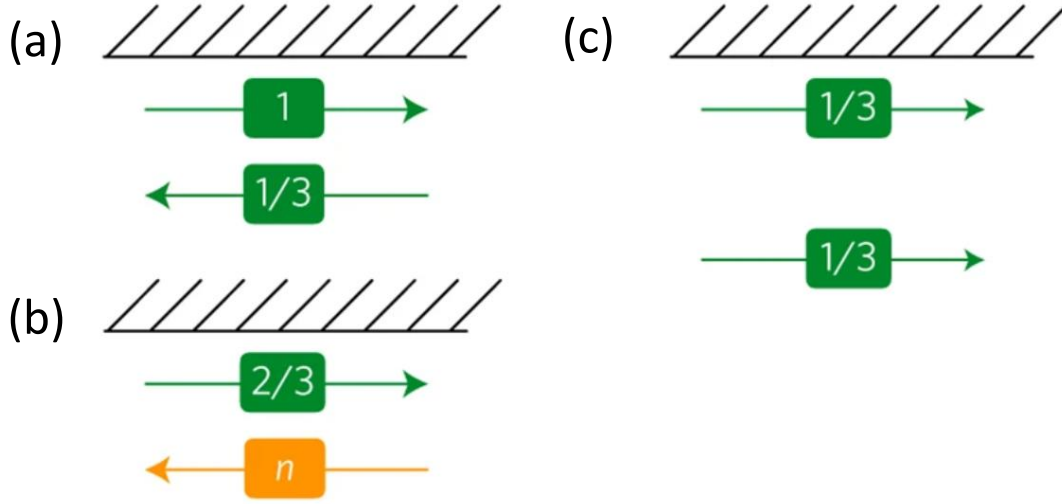


Figure 1.7. Schematic illustration of the edge state construction in $\nu = 2/3$: (a) Edge states of $\nu = 2/3$ with a pair of counter propagating conducting channels, out edge has a conductance of $\frac{e^2}{h}$ and inner edge has a conductance of $-\frac{1}{3}\frac{e^2}{h}$. (b) Edge states of $\nu = 2/3$ with a down stream conducting channel of $\frac{2}{3}\frac{e^2}{h}$ and an up stream neutral mode. (c) Edge states of $\nu = 2/3$ with two down stream channels of $\frac{1}{3}\frac{e^2}{h}$. The figures are adapted from ref. [36].

1.5 Spin transition of $\nu = 2/3$ states in CF picture

Eisenstein et al. first discovered the spin transition at $\nu = 8/5$ [48]. Later, spin transition at $2/3$ was discovered[49]. In a GaAs with $E_Z \ll E_C$, it may be energetically favorable to minimize charging energy at the expense of Zeeman energy. In this case, energy spectrum for spin-full Λ levels for $1/2 < \nu < 1$ can be written as:

$$E^{\uparrow\downarrow} = \hbar\omega_c^{\text{CF}}\left(p - \frac{1}{2}\right) \pm g\mu_B B \quad (1.14)$$

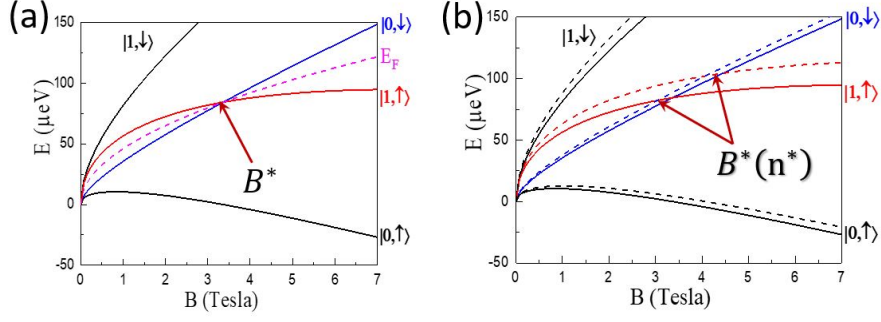


Figure 1.8. Spin transition for $\nu = 2/3$ ($\nu_{CF} = 2$) from CFs picture: CF energy spectrums of $\nu = 2/3$ (two filled Λ levels) for (a) global control of B^* and (b) local control of B^* . The spin polarization of the top level changes at B^* when $\Lambda_{0,\downarrow}$ and $\Lambda_{1,\uparrow}$ crosses. Solid and dotted lines are calculated for two different values of z_0 , which is the extend of the wave function in z direction.

where $\hbar\omega_c^{CF}$ is the CF cyclotron energy which is proportional to the Coulomb energy since only LLL is considered here. Coulomb energy is expressed below:

$$E_C = \frac{e^2}{4\pi\epsilon\sqrt{l_B^2 + z_0^2}} \quad (1.15)$$

where $p = 1, 2, 3, \dots$ is an index number, $l_B = \sqrt{\frac{\hbar}{eB_{\perp}}} \approx \frac{25}{\sqrt{B_{\perp}}} nm$ is the magnetic length and B_{\perp} is the out-of plane component of the magnetic field B , z_0 is the extend of the wave function in z direction. Since CF cyclotron energy is linear in \sqrt{B} while Zeeman energy is linear in B , spin up and spin down levels cross at certain magnetic field B^* . For $\nu_{CF} = 2$ ($\nu = 2/3$) two levels are filled and the polarization of the top-most Λ level for CFs changes at the crossing point B^* , as shown in Figure 1.8a. A spin transition occurs at B^* from unpolarized ($B < B^*$) to fully polarized state ($B > B^*$). The spin polarization change at $\nu = 2/3$ state had been seen and studied by optical probe [50], [51], NMR technique [52], and tunneling spectroscopy [53] etc..

A longitudinal resistance peak at $\nu = 2/3$ plateau is assigned to spin polarization change. When using a small ac current ($< 10nA$), a small longitudinal resistance (SLR) peak appears in the ρ_{xx} minimum plateau. If sweeping gate voltage at a very slow speed in a fixed magnetic field, there is almost no hysteresis. While at a high ac current ($> 25nA$), a huge longitudinal resistance (HLR) is measured with a pronounced hysteresis. Furthermore, the time it takes

for the HLR to relax back to zero after switching off current is from 10 minutes to even hours, indicating typical nuclear relaxation times in *GaAs*. Besides, the time evolution of the HLR peak strongly depends on whether ac or dc current is used. If an ac current is applied, the HLR increases and saturates within minutes. But with a dc current, the HLR collapses after it reaches a maximum. It means that, most likely, the domain structure is influenced by an ac current differently than by a dc current [54], and HLR can only be stabilized changing the current flow direction. Different experimental techniques are also widely used to study the properties related to spin polarization including the study of the activation gap [49], [55], [56], photoexcitation [50], and electron-nuclear spin coupling via hyperfine interactions [57]–[59].

1.6 Possible experimental platform to reveal Parafermions (PFs)

When considering symmetry concerning an exchange of particles, Bose-Einstein statistics (particles with integer spin) and Fermi statistics (particles with half-integer spin) were recognized in the early times. Later, it was found that particles or quasi-particles confined to two dimensions can develop anyonic statistics [60]–[62], for which an exchange results in phases different from 0 and π . Furthermore, the non-abelian statistics, for which exchange or braiding in two dimensions may result in a nontrivial unitary transformation of the corresponding wave functions, can be realized in degenerate ground states [63]. It was recently recognized that the non-abelian statistics open new ways of approaching fault-tolerant quantum computation. Topological quantum computation can be performed with Majorana fermion(MF) [64], but MF-based qubits are not computationally universal. Parafermions(PFs) [65], higher-order non-Abelian excitations, are predicted to have a denser rotation group, and their braiding enables two-qubit entangling gates [66], [67]. A two-dimensional array of parafermions can serve as a building block for a system that supports Fibonacci anyons with universal braiding statistics [68], a holy grail of topological quantum computing. In an essential conceptual paper, Clark et al. proposed that PF excitations can emerge in the fractional quantum Hall effect (FQHE) regime if two counter-propagating fractional chiral edge states with opposite spin polarization are brought into proximity in the presence of superconduct-

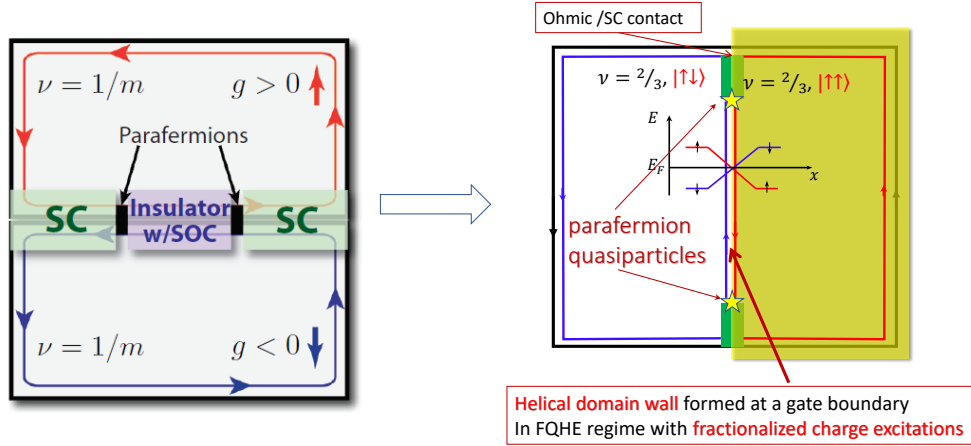


Figure 1.9. Possible platform to realize parafermions at $\nu = 2/3$: Left: Theoretic requirements for obtaining parafermions. Right: Corresponding experimental platform using $\nu = 2/3$ states. The figure on the left is adapted from ref. [69].

ing coupling [69], as shown in Figure 1.9a. A natural system to look for PFs is a 2D electron gas (2DEG) in the FQHE regime, where edge states support fractionally charged excitations, as shown in Figure 1.9b.

It has been predicted that domain walls formed in the integer QHE regime at a filling factor $\nu = 1$ have helical magnetic order [7]. Recently, the formation of helical channels has been reported in the integer and fractional quantum Hall effect regimes (IQHE and FQHE), either as a conducting domain wall formed between two QHE states with different polarizations [8], [9], or counter-propagating chiral channels formed due to charge redistribution in double quantum wells [10]. Domain walls in fractional quantum Hall ferromagnets are gapless helical one-dimensional channels formed at the boundaries of topologically distinct quantum Hall (QH) liquids. Naïvely, these helical domain walls (hDWs) constitute two counter-propagating chiral states with opposite spins. Coupled to an s-wave superconductor, helical channels are expected to lead to topological superconductivity with high order non-Abelian excitations [67], [69]–[71]. In the FQHE regime, spin transitions have been observed at a filling factor $\nu = 2/3$ as well as other fractions [55], [57]. At the transition, the 2DEG

spontaneously phase separates into regions of different spin polarizations, and conducting domain walls are formed along the domain boundaries [72], [73]. An experimental challenge is to devise a system where spin transitions in the FQHE regime can be controlled locally, allowing the formation and manipulation of DWs. Theoretically, neither the magnetic nor electronic structure of these domain walls was known prior to our work and the work of our theory collaborators.

1.7 Electrons-Nuclei interactions

Table 1.1. Properties of the three types of nuclei in *GaAs*.

	^{69}Ga	^{71}Ga	^{75}As
Spin quantum number I	3/2	3/2	3/2
Natural abundance x_n	60.108%	39.892%	100%
Reduced gyromagnetic ratio $\frac{1}{2\pi}\gamma_n(\text{MHz}/T)$	10.2478	13.0208	7.3150
$g_N\mu_N/\mu_B(\times 10^{-3})$	0.732	0.930	0.523
$g_N\mu_N/k_B(\text{mK}/T)$	0.492	0.625	0.351
$ u(0) ^2/v_0(10^{25}\text{cm}^{-3})$	5.8	5.8	9.8
Hyperfine constant $A_H(\mu\text{eV})$	38	49	46
Fully polarization nuclear field $b_N(T)$	-1.37	-1.17	-2.76
$B = 4.2T, E_n = \hbar\gamma_n B(\mu\text{eV})$	0.028	0.036	0.020

This table is adapted from ref.[74]

Although discussion of FQHE phenomena in this thesis is restricted to the lowest Landau level (LLL), $E_Z/\hbar\omega_c \sim 1/60$ in GaAs and even the LLL can be not fully polarized. Some observations cannot be explained by electronic system alone but require inclusion of electron-nuclei coupling. Many experiments [57], [75]–[80] have established the importance of the nuclear system in two-dimensional systems. In general, nuclear spins can interact with electrons nearby via the hyperfine interaction.

The hyperfine interaction between a nuclei spin I and an electron spin S can be written as [74]:

$$H_{HF} = A_H |\Phi(r)|^2 v_0 I \cdot S, \quad (1.16)$$

where A_H is the hyperfine coupling constant, $|\Phi(r)|^2 v_0$ is the wavefunction overlap with a unit cell volume. For *GaAs*, the hyperfine interaction essentially is the Fermi contact

interaction between the nuclei and the s-type conduction band electrons. Therefore, the hyperfine coupling constant can be written as [74]:

$$A_H \approx \frac{2\mu_0}{3} \frac{g_e \mu_B g_N \mu_N}{v_0} |u(0)|^2, \quad (1.17)$$

where μ_0 is the permeability constant, g_e the free electron g -factor, g_N the nuclear g -factor, μ_B the Bohr magneton, μ_N the nuclear magneton, v_0 the volume of the crystal unit cell, and $|u(0)|^2$ is the probability of finding an electron at a nuclear site with the normalization condition $\int |u(0)|^2 d^3r = v_0$. Table 1.1 shows the details of properties of nucleus in *GaAs*.

When the nucleus are polarized, they create a local magnetic field (or nuclear hyperfine field) B_n felt by the spin of an electron through the hyperfine coupling. Summing up contributions from all three types of nuclei, B_n can be written as [74]:

$$B_n = \sum_{i=1}^3 b_{N,i} \frac{\langle I_i \rangle}{I}, \quad (1.18)$$

with

$$b_{N,i} = \frac{2\mu_0}{3} \frac{g_e I_i}{g^*} \gamma_{n,i} \hbar \frac{x_{n,i}}{v_0} |u_i(0)|^2 = \frac{A_H I x_{n,i}}{g^* \mu_B}, \quad (1.19)$$

where $x_{n,i}$ is the natural abundance of the i th type of nuclei, g^* the reduced electron g -factor, $\gamma_{n,i} = \frac{g_N \mu_N}{\hbar}$ the gyromagnetic ratio of the i th type of nuclei. Due to the contact type interaction and the reduced electron g -factor, B_n can be as large as 5.3T in *GaAs* (See Table 1.1). With the nuclear hyperfine field, the Zeeman energy can be written as:

$$E_Z = g^* \mu_B (B_{ext} + B_n), \quad (1.20)$$

where B_{ext} is the external applied magnetic field and B_n the nuclear field. Any spin phenomenon related to the Zeeman energy in the LLL is strongly affected by the hyperfine coupling. The flip-flop processes is the major source for the enhancement of nuclear polarization, which is also called Overhauser effect. Experimentally, dynamical nuclear polarization (DNP) can be achieved by many methods such as current-induced nuclear spin polarization [75], [78] or optical pumping [81].

Similarly, the effective magnetic field B_e , created by polarized electrons can act on the nuclear spins and, for a 2D electron system, can be written as [74]:

$$B_e = b_e \langle S \rangle = -\frac{2\mu_0}{3} g_e \mu_B n_e |u(0)|^2 |\phi(z)|^2 \langle S \rangle, \quad (1.21)$$

where n_e is the 2D electron density and $\phi(z)$ is the 1D envelope of the electron wavefunction of the lowest subband of the potential well forming the 2D electron system. For a typical 2D system with $n_e \sim 10^{11} \text{cm}^{-2}$, B_e is within a few mT even for a fully polarized 2D gas. In nuclear magnetic resonance (NMR) experiments, B_e can be detected and is referred to as the Knight's shift $K_s = \frac{\gamma_n}{2\pi} B_e$, which can be used to measure the electron spin polarization. The interaction between nuclei and electron in our helical system will be discussed in chapter 2.

1.8 Skyrmions

The $\nu = 1$ QH state is also called a Quantum Hall Ferromagnet (QHF) state since it remains spin polarized and is stabilized in a ferromagnetic state due to the Coulomb exchange energy even in the absence of a Zeeman energy. Electron-electron interactions play a major role in this state.

Theoretically, in the limit of a vanishing Zeeman energy, the lowest-lying charged energy excitations of the QHF state are topological objects with an underlying spin-texture. These excitations, called skyrmions, are characterized by having their spins gradually turned from downward at the center to upward at a distance moving away from the center, and hence exhibiting a vortex-like winding configuration (see Figure 1.10a). When the Coulomb exchange energy is much larger than the Zeeman energy, a skyrmion is energetically more favorable than a single spin flip because it prefers locally aligned spins. The energy needed to create a skyrmion is [24]:

$$E = E_{exch} + E_Z = \rho_s E_C k^2 + g^* \mu_B B, \quad (1.22)$$

where E_{exch} is the Coulomb exchange energy, E_Z the Zeeman energy, ρ_s the "spin stiffness", k the wavevector. For $E_Z = 0$, the size of skyrmion should be infinite. When E_Z is large, single spin flips are restored. In between, the size of skyrmion shrinks when increasing the

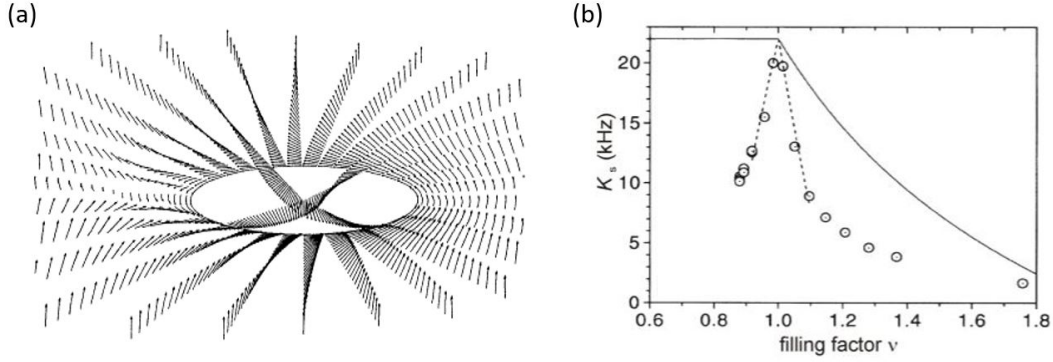


Figure 1.10. Skyrmions around $\nu = 1$: (a) Illustration of a skyrmion spin texture: numerous electron spins are gradually flipped but yet carrying exactly one unit of charge. The size of a skyrmion is determined by the energy competition between E_Z and E_C . This figure is adapted from ref. [82]. (b) Knight's shift as a function of filling factor near $\nu = 1$: the existence of skyrmions was first proved through optically pumped NMR experiments [83]. The polarization deviates on both sides of $\nu = 1$ as expected for skyrmions. The solid line is the expected polarization for a non-interacting system. This figure is adapted from ref. [83].

Zeeman energy for balancing the Zeeman and Coulomb energies. Therefore, deviating from $\nu = 1$ creates skyrmions for $\nu > 1$ or $\nu < 1$.

Experimentally, the first experimental evidence of the existence of skyrmions came from optically pumped NMR (OPNMR) experiments by Barrett's group (see Figure 1.10b, which shows the Knight shift as a function of filling factor) [83]. The Knight's shift is directly proportional to the electron spin polarization. The decrease of Knight shift (or electron spin polarization) was attributed to the formation of spin textures and is consistent with the theoretical prediction that finite-size skyrmions exist around $\nu = 1$. Skyrmions are also expected to exist around the QHF state $\nu = 1/3$ [84] and there has been some indication that they do exist in this regime [85]. Chapter 2 in this thesis will also discuss a possible picture forming skyrmion crystal near $\nu = 2/3$.

1.9 Topological insulators

Study of the quantum Hall effect in 2DEG system has led to a new classification of matter based on their topological order [86]. Quantum Hall states do not break any symmetries, they

define a topological phase where certain fundamental parameters, such as Hall conductance, is quantized and insensitive to any smooth transformation unless the system go through a quantum phase transition. In the past 10 years a new class of topological materials has emerged, so-called topological insulators (TIs) [87]. TIs, like normal insulators, have a bulk energy gap. However, the edge (or surface, depending on the system dimension) holds massless states that are protected against weak perturbations by time-reversal symmetry. In 2005, theorists predicted the existence of the quantum spin Hall (QSH) insulator [88], [89]. In 2007, experimentalists demonstrated such a topological state in HgTe quantum well system [90]. An ideal two-dimensional TI, a quantum spin Hall insulator, features an insulating bulk and a conducting edge. Edge channels consist of two counter-propagating modes with opposite spin orientation, retaining Kramer’s degeneracy. Since the electron spin is locked to its momentum, edge states of TIs are insensitive to any non-magnetic impurity scattering.

Bi_2Se_3 is a prototypical 3D TI with a non-zero bulk conduction. In 3D TIs, the protected conducting state is a surface with a single Dirac cone protected by the time-reversal symmetry. Moreover, the growth of intrinsic Bi_2Se_3 crystal makes the Fermi level close to the Dirac point, which serves as a good candidate for the transport study. Similar to the quantum spin Hall insulator, electrons in the surface states of Bi_2Se_3 feature spin-momentum locking.

Like mentioned above, surface states of TIs are not sensitive to scattering without a spin flip. However, by inducing a long-range magnetic order and breaking the time-reversal symmetry at the surface of the TI one can open a gap in the Dirac spectrum. An ability to modulate topological surface states (TSS) is a prerequisite to create a quantum anomalous Hall insulator (QAHI) or an axion insulator [91], [92]. Such exotic magnetic topological phases may host robust charge and spin currents, which can be used in electronics or spintronics applications [91], [93], [94].

There are several different strategies to induce a long-range magnetic order including magnetic doping, coupling through proximity effect, and magnetic intercalation. This thesis will focus on inducing magnetic order in TIs by proximity coupling to magnetic materials (MM). Unlike an existing challenge of simultaneously optimizing both the TSS and bulk magnetism for observing a QAHI or axion insulator in dilute magnetically-doped TIs or intrinsic magnetic TIs, MM-TI heterostructure allow independent control of TSS and mag-

netism. The MM induces magnetic order in the TI through a proximity coupling. This magnetic proximity effect has a relatively short length-scale of a few Angstroms from the time-reversal symmetry is broken only at the interface of the TI and MM, but not in the bulk of the TI. In addition, the presence of strong spin-orbit coupling may enhance magnetic order in the MM [95]–[98].

The magnetic proximity effect can be regarded as a permeation of the magnetic ground state into a neighboring material through the interaction between magnetic moments in the MM and the electron spins in the neighboring material. There are three major types of interactions in MM-TI heterostructures: direct exchange coupling, magnetic extension, and surface-state-assisted magnetism. This thesis will focus on a metamagnetic-insulator/TI system to study its interfacial interaction mechanism.

2. FORMATION AND CONTROL OF HELICAL STATES IN CHIRAL SYSTEM

Parts of this work have been published in Phys. Rev. B 97, 245304 (2018), and are under review in Nat. Comm., arXiv:2101.00126.

2.1 Introduction

While electrons propagating along chiral channels in the QHE regime are topologically protected from backscattering, there is no such protection for helical channels. In CdTe:Mn quantum wells [99] ferromagnetic transition can be designed to occur at a filling factor $\nu = 2$, and helical domain walls (hDWs) are formed due to the crossing of $|0, \uparrow\rangle$ and $|1, \downarrow\rangle$ Landau levels. These states are coupled by Rashba spin-orbit coupling and, indeed, a 1K anticrossing gap has been measured at low temperatures in the bulk. In short hDW channels, electron transport is carried by in-gap impurity states [8]. These impurity states are expected to retain the helical nature of the parent hDW and, coupled to a superconductor, to support non-Abelian excitations [9]. In double quantum wells helical channels are constructed from two counter-propagating chiral channels which belong to different Landau levels and, as in CdTe: Mn, one would expect Rashba spin-orbit interactions to facilitate inter-channel scattering (these materials have almost identical Rashba constants, 6.93 eV in CdTe vs 5.206 eV in GaAs [100]). Nevertheless, ballistic transport over macroscopically large distances $> 300\mu m$ has been found experimentally [36], indicating that chiral channels are spatially well separated, rendering these channels unsuitable for parafermion formation (inter-channel mixing is required to form parafermions [69]).

Another intriguing possibility to form helical channels with fractionalized charge excitations is based on the spin transition at $\nu = 2/3$ [10]. Superficially, this spin transition between polarized (p) and unpolarized (u) $\nu = 2/3$ FQHE states can be understood as a crossing of $|0, \uparrow\rangle$ and $|1, \downarrow\rangle$ Λ levels for composite fermions [50], [101] and a helical domain wall with fractionalized charge excitations (fhDW) can be associated with two counter-propagating $1/3$ chiral states [55]. Such description of the fhDW is an oversimplification, though, due to a complex nature of the underlying many-body states. Recent theoretical analysis of fhDW

formed between p and u $\nu = 2/3$ states suggested the formation of 2+2 counter-propagating channels, with the inner two channels being fully hybridized and the outer ones having opposite spin polarization [102]. Coupled to an s-wave superconductor this fhDW is expected to form a topological superconductor with parafermionic end modes.

Electron transport are studied in samples where hDWs of different lengths L are formed by electrostatic gating in a Hall bar (HB) geometry. Experimentally, in the limit $L \rightarrow 0$ approximately 12% of the edge current is diverted into the hDW, a number drastically different from the 50%, a prediction for two non-interacting counter-propagating chiral channels. To address this discrepancy theoretically, tunneling between Luttinger liquid modes [103] through a hDW in the strong coupling limit [104]–[106] is considered and it is confirmed that results remain the same if hDW is modeled as an extended object. It is found that in the presence of a strong inter-edge tunneling edge channels in u and p regions populate unequally, both at the boundary of the 2D gas and within the hDW, forming a number of down- and up-stream charge, spin and neutral modes. For spin-conserving tunneling 1/4 of the incoming charge current is diverted into the hDW, while allowing spin-flip processes further reduces hDW current. Indeed, at high bias currents an increase in the current carried by the hDW is observed. This indicates formation of a bottleneck for spin flips due to Overhauser pumping of nuclei and a crossover from spin-non-conserving to spin-conserving transport.

A controllable spin injection experiment is also constructed in this single helical domain wall and use nuclear bath polarization as a detector of low-energy spin waves. Omnidirectional propagation of nuclear polarization, which is consistent with nuclear electron hyperfine interaction, is observed for electron spin-increasing injection. For the electron spin-decreasing injection, a unidirectional propagation of nuclear polarization is observed, indicating generation of low energy spin waves in the polarized state.

In the end, it is found that in a quasi-Corbino (qC) geometry conductance was suppressed by more than an order of magnitude and does not depend on the length of the channel, and, most likely, was limited by a residual conductance through the bulk of the gaped $2/3$ state. The inconsistency between HB device and qC device may be attributed to the enhancement of contact resistance in the qC device. At the same time, the expected quantized value

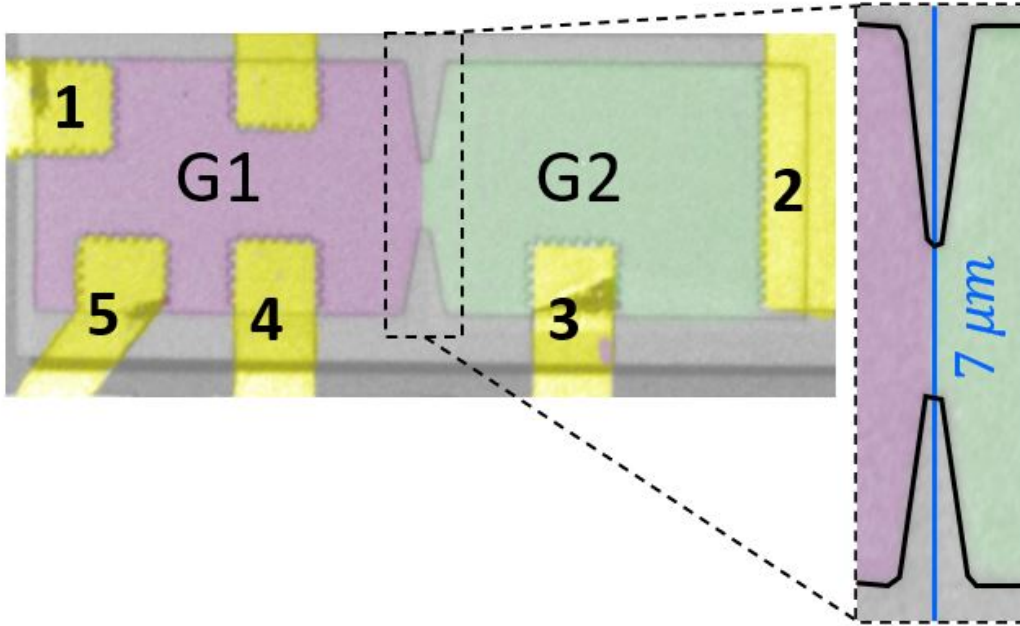


Figure 2.1. A typical Hall bar device with hDWs length of $L = 7\mu\text{m}$: A false color image of a typical device: yellow regions are Ohmic contacts; 2D gas in green and magenta regions is controlled by gates G1 and G2; in the grey area 2D gas is removed. In the enlarged section thick lines outline mesa boundary and thin vertical blue line marks a physical boundary between G1 and G2.

$1/15G_q$ for the topologically protected chiral edge channels formed between $2/3 - 3/5$ and $1/3 - 2/5$ FQHE states are measured. This disparity also raised questions of Fermi level adjustment in the vicinity of Ohmic contacts and stability of a fhDW in the presence of potential gradients.

2.2 Wafers, devices and measurements

A number of wafers with inverted GaAs/AlGaAs interface have been grown by our collaborator Professor Loren Pfeiffer. These inverted GaAs/AlGaAs heterojunctions are grown by molecular beam epitaxy, and the top layer is 130-230nm thick GaAs, Si δ -doping placed 70-300 nm beneath the heterojunction interface. The top 25 nm of GaAs is lightly doped to reduce the surface pinning potential. Inverted heterostructures allow electrostatic gating

of a shallow 2D gas with no hysteresis. A list of quantum well (QW) wafers used in this chapter can be found in Appendix A.

Several devices in a Hall bar (HB) geometry with multiple gates have been fabricated from wafer A (LE40) with electron gas density $0.9 \cdot 10^{11} \text{cm}^{-2}$ and mobility $4.95 \cdot 10^6 \text{cm}^2/\text{Vs}$ in order to study transport through hDWs. Devices are separated into two regions $G1$ and $G2$ by semi-transparent gates (10 nm of Ti), the gates are separated from the surface of the wafer and between each other by 50nm of Al_2O_3 grown by the atomic layer deposition (ALD). Figure. 2.1 displays a typical device with hDWs length $L = 7\mu\text{m}$. Here the hDWs length L is a lithographical length of the gate boundary between physical edges, the actual length is smaller in HB devices by twice the depiction length ($\sim 0.3\mu\text{m}$). In different devices L varies between $2 - 100\mu\text{m}$. A 2DEG is created by shining red LED at ~ 4 K. Contacts are formed by annealing Ni/Ge/Au 30nm/50nm/100nm, in a H_2/N_2 atmosphere. Details of device fabrication can be found in Appendix B. Electron density n under $G1$ and $G2$ are able to be controlled independently by electrostatic gates.

Measurements were performed in a dilution refrigerator at a base temperature of 20 mK using standard lock-in technique at 17.7 Hz in a 4-terminal configuration ($I_{ac} = 0.1 - 10$ nA, limiting the voltage across the device to $< 10 \mu\text{V}$). Gate voltages (V_{g1} and V_{g2}) were applied by a home-made digital-to-analog converter (DAC) to control the electron gas density. Here $V_g = (V_{g1} + \alpha V_{g2})/2$ controls overall densities under gates $G1$ and $G2$ (coefficient $\alpha = 0.75$ accounts for the difference in oxide thickness under the gates), and $\Delta V_g = V_{g1} - \alpha V_{g2}$ controls density difference. Density is uniform across the whole device for $\Delta V_g = 0$.

2.3 Devices characterization

2.3.1 Quality of 2DEGs

After cool down from room temperature to 4 Kelvin devices are illuminated with a red LED at $100 \mu\text{A}$ for 1 min and left to relax for 12 hours before cooling to the base temperature. This sequence is found to result in the best quality and uniformity of a 2D gas in our experiments, with the sharpest spin transition and widest fractional quantum Hall states. With zero gate voltages densities of 2D gases under gates $G1$ and $G2$ are approximately

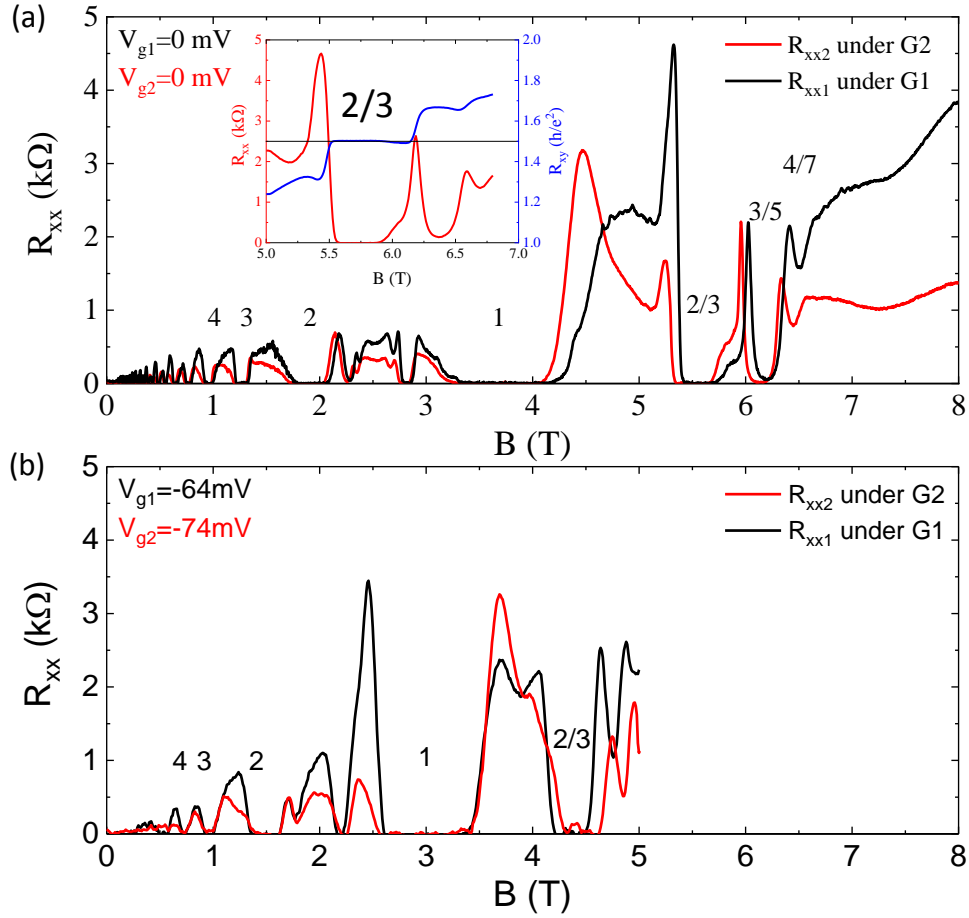


Figure 2.2. Magneto-resistance R_{xx} of a 2D gas as a function of magnetic field: R_{xx} at (a) zero gate voltages and (b) gate voltages where $\nu = 2/3$ is close to the spin transition measured at the base temperature $T=20$ mK. Inset shows R_{xx1} and R_{xy1} for $V_{g1} = 0$ from the same cool-down but with different LED sequence.

$0.9 \cdot 10^{11} \text{ cm}^{-2}$, see Figure 2.2. Small differences in the quality of 2D gases under two gates are attributed to different thicknesses of gate oxides (50nm under G1 and 100nm under G2), as well as to a small difference in the thickness of semi-transparent titanium layers which form gate electrodes. Application of negative gate voltage and reduction of the density to $\approx 0.7 \cdot 10^{11} \text{ cm}^{-2}$ does not degrade the quality of 2D gases as shown in Figure 2.2b.

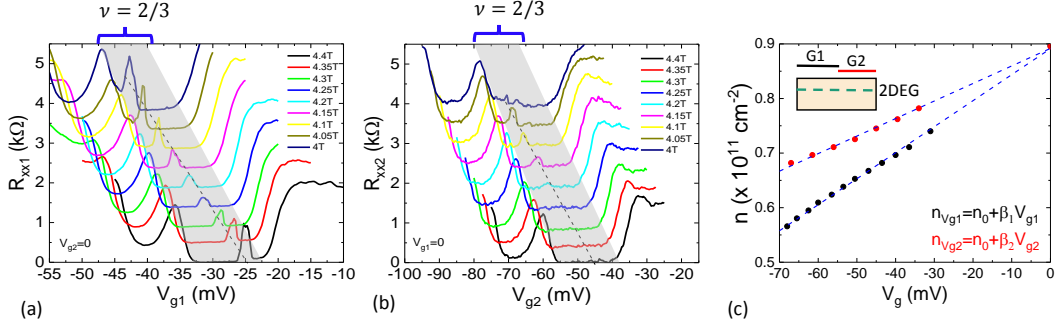


Figure 2.3. Magneto-resistance R_{xx} of a 2D gas as a function of gate voltage: R_{xx} under (a) G1 and (b) G2 as a function of gate voltage at different magnetic fields in the vicinity of $\nu = 2/3$. Grey shading outlines the $\nu = 2/3$ state, dashed lines mark the spin transition. (c) Electron density as a function of gate voltage: dashed lines are linear fits. In the inset there is a schematic of the device cross section which shows difference in gate oxide thicknesses.

2.3.2 Spin transition within $\nu = 2/3$ plateau

As discussed in chapter 1, the CFs' energy levels cross at B^* , which separates $\nu = 2/3$ into polarized and unpolarized states. The energy gap for quasiparticle excitations vanishes providing a mechanism for charge backscattering and, hence, at $B = B^*$ resistance of the 2D gas is no longer zero. In our devices, it is possible to control B^* by electrostatic gating, and small peaks within the $2/3$ plateau in Figure 2.3 ab, an evolution of the 2D gas resistance in the vicinity of $\nu = 2/3$ as a function of magnetic field and gate voltage, are quantum Hall ferromagnetic transitions between polarized (p) and unpolarized (u) regions.

2.3.3 Gate voltage and filling factor

Electron density is extracted from the position of $\nu = 3/5$ state (within this field range $\nu = 3/5$ is far from the spin transition). Electron density is a linear function of gate voltages $n(V_g) = n_0 + \beta V_g$ (see Figure 2.3 c), where coefficients $\beta_1 = 4.76 \cdot 10^8 \text{ cm}^{-2}/\text{mV}$ and $\beta_2 = 3.21 \cdot 10^8 \text{ cm}^{-2}/\text{mV}$ are almost the same for different cooldowns while the zero voltage density n_0 varies within 5%. Here gate voltages can be converted to filling factors $\nu = n\phi_0/B$, where B is an external magnetic field, $\phi_0 = h/e$ is a flux quanta and n is electron

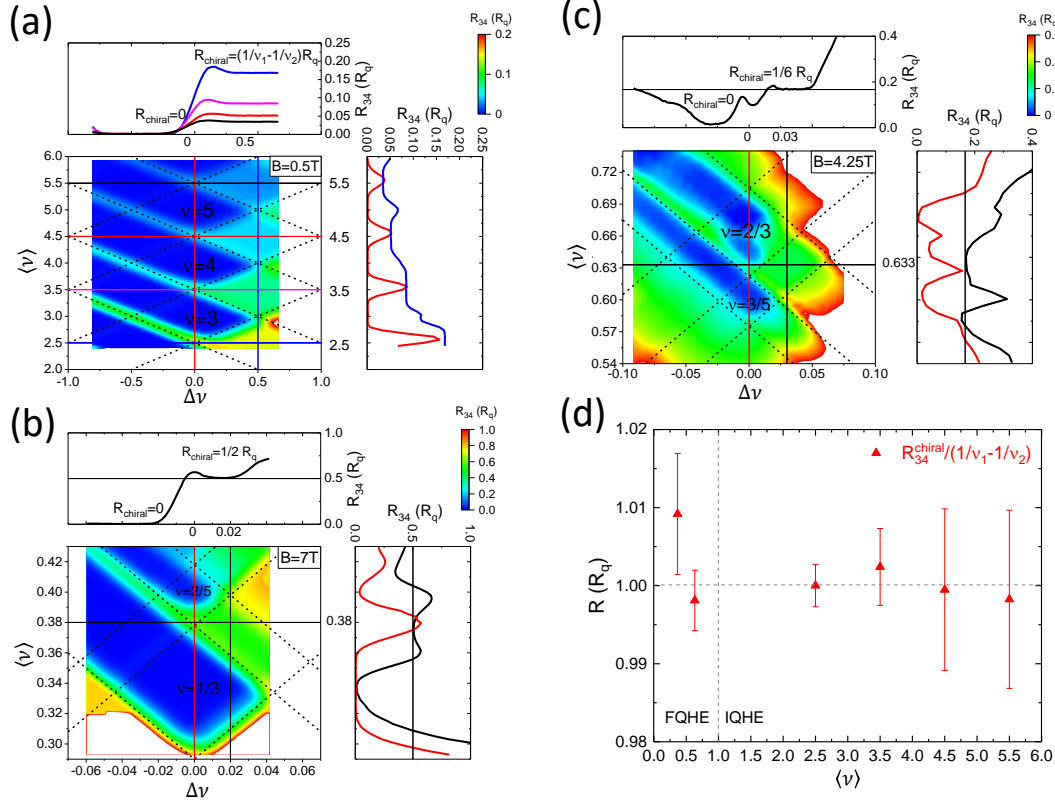


Figure 2.4. Chiral channels in IQHE and FQHE regimes: (a-c) Resistance R_{34} is plotted as a function of $\langle \nu \rangle$ and $\Delta \nu$ for the sample with $20 \mu\text{m}$ gates boundary. The top and right panels in each plot show line cuts indicated by solid lines in color plots. Resistance R_{34} is quantized for $\Delta \nu = +1$ in the IQHE regime and for $\Delta \nu^* = +1$ in the FQHE regime (ν^* is a composite fermion filling factor), $R_{34} = 0$ for $\Delta \nu = -1$ and $\Delta \nu^* = -1$. (d) $R_{34}/(1/\nu_1 - 1/\nu_2)$ for chiral channels is plotted as a function of a filling factor.

density, based on the linear dependence of electron density as a function of gate voltage at a fixed magnetic field.

2.4 Transport in the presence of a chiral channel

Before studying helical channels, chiral channels were first measured for system calibration and self-consistency check. Measurements of R_{34} were performed when filling factors ν_1 and ν_2 under gates $G1$ and $G2$ are different quantum Hall liquids. According to Landauer-Büttiker theory [44], [107] for $B > 0$ $R_{34} = (\frac{1}{\nu_1} - \frac{1}{\nu_2}) \cdot R_q$ for $\Delta \nu > 0$ and $R_{34} = 0$ for $\Delta \nu < 0$ (zero and non-zero values will be switched for $B < 0$). In the IQHE regime when filling

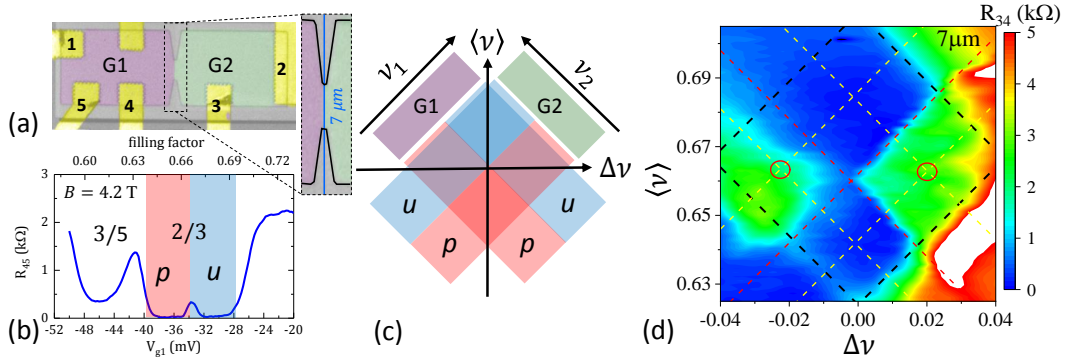


Figure 2.5. Formation of helical domain walls at $\nu = 2/3$: (a) A false color image of a typical device. Yellow regions are ohmic contacts, 2D gas in green and magenta regions is controlled by gates G1 and G2, in the grey area 2D gas is removed. In the enlarged section thick lines outline mesa boundary and thin vertical blue line marks a physical boundary between G1 and G2. (b) Magnetoresistance $R_{45} = (V_5 - V_4)/I$ of a 2D gas is plotted as a function of gate voltage (controlling filling factor ν) at a fixed $B = 4.2$ T. Small peak at -34 mV is the phase transition between unpolarized (u) and polarized (p) $\nu = 2/3$ FQHE liquids. (c) A diagram of u and p states as a function of ν_1 and ν_2 under gates G1 and G2; $\langle \nu \rangle = (\nu_1 + \nu_2)/2$ and $\Delta \nu = (\nu_1 - \nu_2)$. (d) Resistance $R_{34} = (V_4 - V_3)/I$ across a $7 \mu\text{m}$ - long gates boundary is plotted as a function of $\langle \nu \rangle$ and $\Delta \nu$. Black square outlines the $\nu = 2/3$ region, red lines mark u - p transitions and yellow lines mark centers of u and p regions.

factors ν under gates $G1$ and $G2$ differ by one, a single chiral channel is formed along the gates boundary and resistance R_{34} measured across the boundary is either quantized or zero depending on the sign of the filling factor gradient and direction of B . Likewise, a chiral channel is formed when a gates boundary separates two different FQHE states. In Figure 2.4abc, resistance R_{34} is plotted over a range of filling factors in IQHE and FQHE regimes. In (d) it is plotted experimentally measured R_{34} scaled by $(\frac{1}{\nu_1} - \frac{1}{\nu_2})$ as a function of filling factor $\langle \nu \rangle$; the values fall within 1% of the expected values. The R_{34} value is averaged in 1mV vicinity around the QHE state center. The error bar is the corresponding standard deviation.

2.5 Formation of helical domain walls at $\nu = 2/3$

Independent control of filling factors ν_1 and ν_2 under G1 and G2 divides the $2/3$ region into four quadrants uu , pp , up and pu , where the first letter corresponds to polarization of the state under G1 and the second corresponds to polarization under G2. Within the Landauer-Büttiker formalism [44], [107] resistance $R_{34} = (1/\nu_1 - 1/\nu_2)R_q$ should be zero for all combinations of polarizations under the gates, since quantum numbers $\nu_1 = \nu_2 = 2/3$ for both u and p states (here $R_q = h/e^2$, h is the Plank's constant and e is an electron charge). Experimentally, R_{34} is found to be vanishingly small in uu and pp quadrants, consistent with a single FQHE state being extended over the whole device. $R_{34} > 0$ in up and pu quadrants indicates backscattering between edges. Combined with zero longitudinal resistance under G1 and G2, it indicates formation of a conducting channel along the gates boundary. Unlike resistance measured across chiral channels (e.g., between $\nu = 2/3$ and $\nu = 3/5$ FQHE states), resistance measured across the boundary of u and p quantum liquids at $\nu = 2/3$ shows almost no dependence on the direction of the external magnetic field and density gradient, consistent with the formation of a helical domain wall [108].

2.5.1 Field dependence of helical domain wall

Figure 2.6 shows resistance in the vicinity of $\nu = 2/3$ for two opposite-field directions with hDW length of $50\mu m$. As expected for a helical channel hDW resistance does not depend on the field direction, at least close to the center of the $\nu = 2/3$ state (at the edges of the $\nu = 2/3$ state there is an onset of chiral channels formation, the resistance of chiral channels depends strongly on field direction as discussed in more details in the next section).

Field evolution of a $7\mu m$ -long domain wall is shown in Figure 2.7. Here, R_{34} is recorded as a function of V_{g1} and V_{g2} at different magnetic fields. For $B = 4.0T < B^*$ (the lower right corner), states under both gates are unpolarized and $R_{34} = 0$. Similarly, when $B = 4.9T > B^*$, states under both gates are fully polarized with $R_{34} = 0$. By increasing B , the magnetic field is adjusted to position spin transitions under both gates to be close to the middle of the $\nu = 2/3$ state (marked red rectangle), as shown in Figure 2.7.

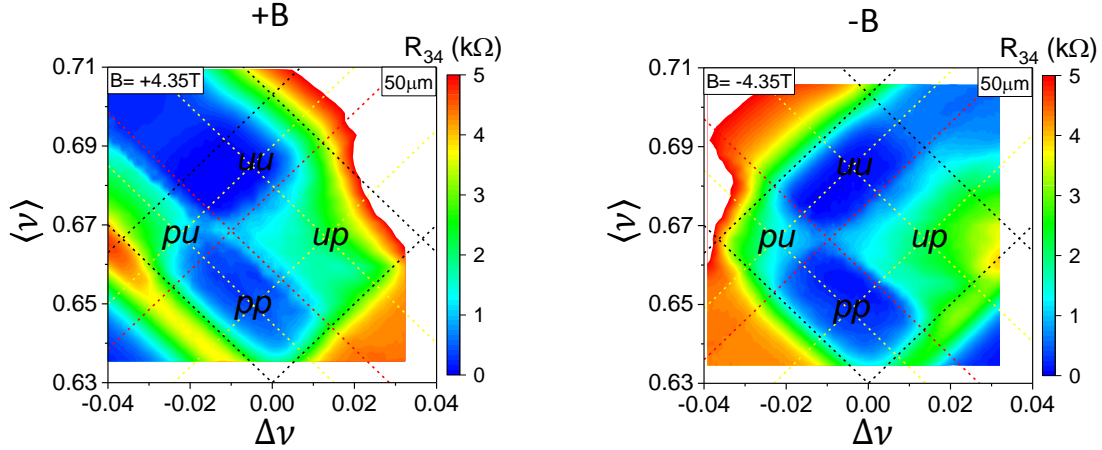


Figure 2.6. Stability of hDW resistance R_{34} under magnetic field inversion for the sample with $50 \mu\text{m}$ gates boundary.

2.5.2 Temperature dependence of helical domain wall

One of the important perspectives to understand the transport property of hDW is to study the temperature dependence of resistance across the gates boundary. R_{34} is measured as a function of filling factors under two gates at fixed $B = 4.3 \text{ T}$ for temperatures from 18 mK to 272 mK as Figure 2.8a shown. Figure 2.8b displays the Arrhenius plots ($\ln R_{34}$ vs $1/T$) at different filling factors. In our study of a single domain wall, R_{34} saturates at low temperatures to a nonzero value at a filling factor range of $0.651 < \nu_1, \nu_2 < 0.671$ (see Figure 2.8b). This nonzero value originates from the formation of a conducting domain wall channel, which can be formed below $T \sim 40 \text{ mK}$, along the gates boundary. Activation gaps of the spin transition have been previously studied [56] in a tilted magnetic field. In [24] authors observe a vanishing resistance peak at the lowest temperature ($T \approx 22 \text{ mK}$), they explained that by reducing the temperature, the size of the domains is reduced, at a low-temperature regime, the large networks of domains are localized, and backscattering is suppressed. In our experiments, the length of the domain wall is fixed and is temperature independent.

The value of activation gap (Δ), extracted from a linear fit to an Arrhenius plot ($\ln R(\propto \frac{\Delta}{2k_B T})$), as a function of filling factor is shown in Figure 2.8c. There is no electron transfer

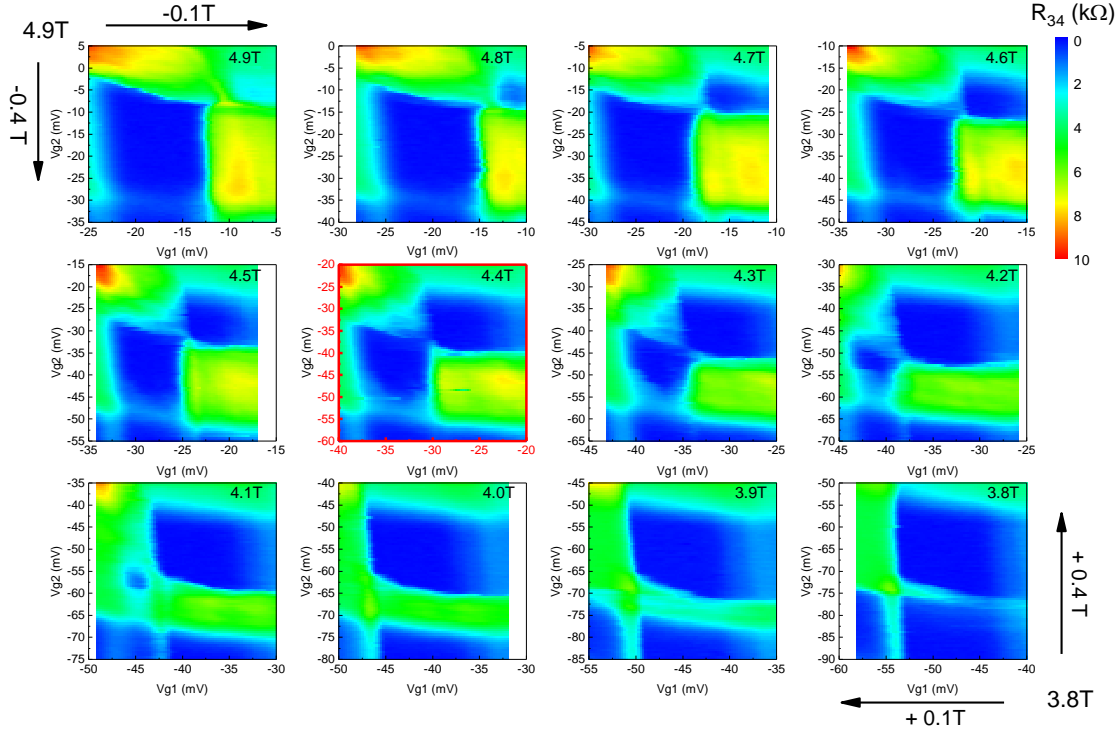


Figure 2.7. Evolution of spin transition boundaries with magnetic field for a $L = 7 \mu\text{m}$ hDW device: Red rectangle marks the field where spin transitions under both gates are centered within the $\nu = 2/3$ state, the optimal field may differ by ± 0.2 T between different cooldowns.

across the constriction in the middle of the u and p phases when density is tuned to be uniform across the sample, the excitation gaps are > 200 mK. Also, the activation gap reduces when the helical domain wall (pu state) is formed. Similar studies have been performed in the IQHE regime in double quantum wells [109]. In those experiments, measurements were performed between $\nu = 3$ and $\nu = 4$, where two pseudospin levels crossed. A reduction of activation energy was also observed. The authors attributed the reduction of the activation gap to the formation of the skyrmion, which may be trapped inside the domain wall. These skyrmions, which would have low-energy excitation, will result in the reduction of the activation gap.

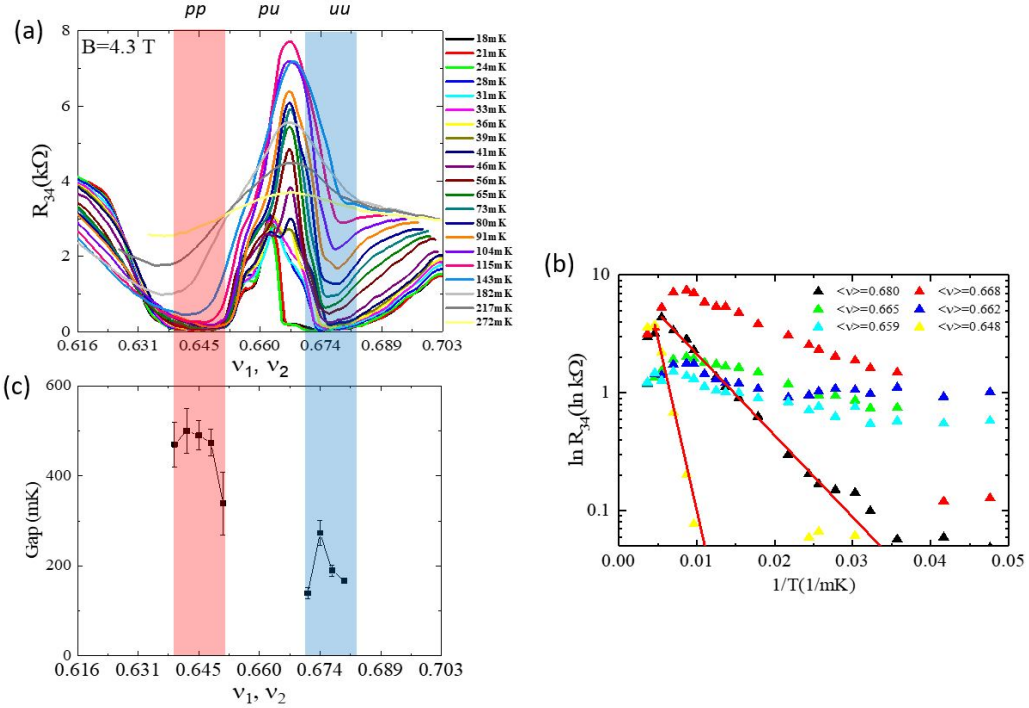


Figure 2.8. Activation gap. (a) Temperature dependence of resistance is measured across a $L = 7 \mu m$ hDW for various temperatures at $B = 4.3 T$. (b) Arrhenius plots at different filling factors. (c) Evolution of an activation gap.

2.5.3 Length dependence of helical domain wall

The hDW data for different DW lengths (Figure 2.9) were measured close to thermal equilibrium, where a small AC current does not affect the position of the spin transition boundary. The length dependence of current through DW for the average between up and pu are displayed in Figure 2.10c. In general, the experimental DW current shows exponential decay with the increase of DW length.

2.6 Transport study of the Domain wall in $\nu = 2/3$ plateau

Protection of helical states from backscattering and localization is weaker than for spatially separated chiral edge states, and conduction of hDWs is length-dependent. In Figure 2.10a fraction of the external current I that flows through the hDW, $i_{DW} = I_{DW}/I$, is plotted as a function of hDW length L . i_{DW} is found to decrease exponentially with L ,

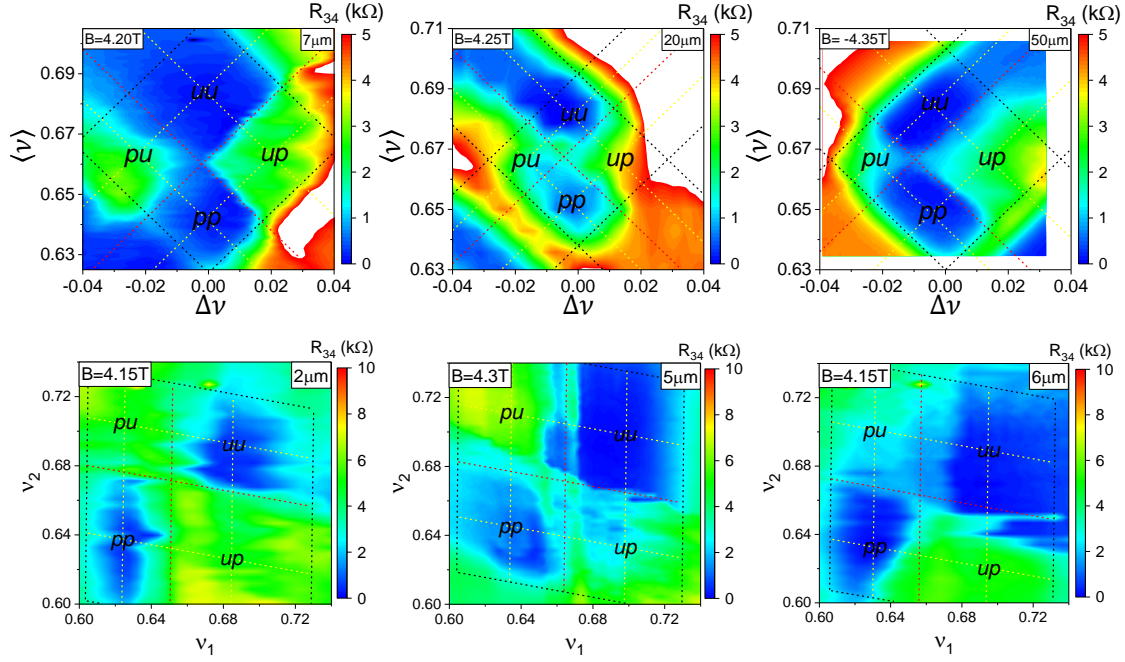


Figure 2.9. Resistance R_{34} as a function of $\langle \nu \rangle$ (or ν_1) and $\Delta \nu$ (or ν_2) for other gates boundary lengths: R_{34} is plotted as a function of $\langle \nu \rangle$ and $\Delta \nu$ for samples with $7 \mu\text{m}$, $20 \mu\text{m}$ and $50 \mu\text{m}$ gates boundary and as a function of ν_1 and ν_2 for samples with $2 \mu\text{m}$, $5 \mu\text{m}$ and $6 \mu\text{m}$ gates boundary. Black lines outline the $\nu = 2/3$ region, red lines mark $u-p$ transitions and yellow lines mark centers of u and p regions.

$i_{DW} = i_{DW}^0 \exp[-L/L_0]$, with a characteristic length $L_0 = 47 \mu\text{m}$. The value of i_{DW}^0 corresponds to the transport through a ballistic hDW in the absence of localization. Within a simplified model of $\nu = 2/3$ edge states consisting of equally populated $1/3 + 1/3$ chiral modes and no interaction between chiral channels with opposite spin polarization (Figure 2.10a), one expects $i_{DW}^0 = 1$ (marked by a blue arrow in Figure 2.10c), an order of magnitude larger than the experimentally observed value (marked by a green arrow). Note that transport through helical modes formed in double quantum well structures is well described by this simple model of weakly interacting chiral states [10].

An isolated hDW at a boundary of p and u phases was studied in Refs. [102], [108], where disk and torus geometry were employed to avoid physical edges of the sample and coupling of domain wall modes to these edges. Analytical model and numerical results indicate an existence of modes with opposite velocities and spins within the hDW region, a prerequisite

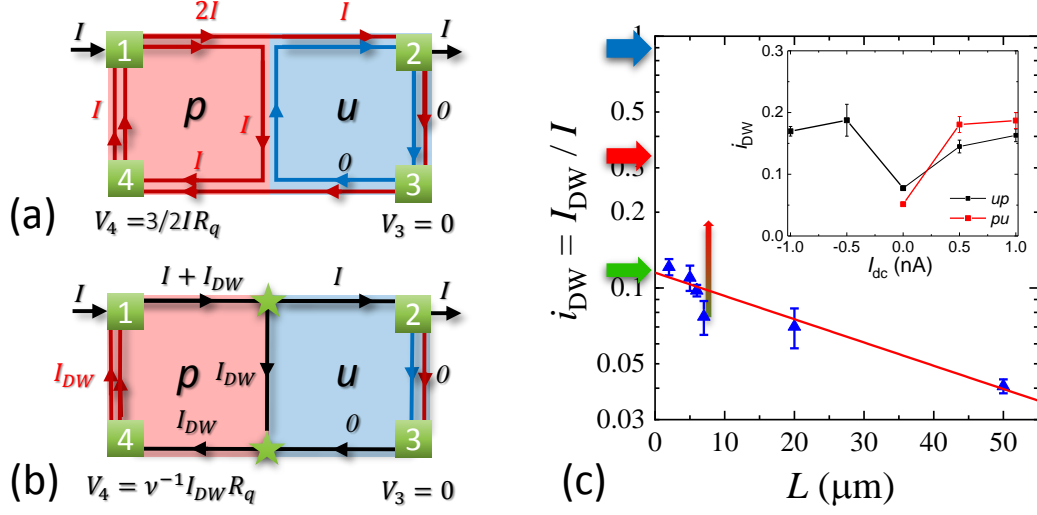


Figure 2.10. Conduction of hDWs: (a) A simplified picture of non-interacting chiral edge modes at $\nu = 2/3$. An inner spin-up edge (red) in p state carries current I while a spin-down edge (blue) in u state carries no current. (b) Charge conservation and chirality of edge states set the potential $V_4 = \nu^{-1} I_{DW} R_q$ to be proportional to the current I_{DW} diverted via the helical domain wall. (c) Scaling of the domain wall current $i_{DW} = I_{DW}/I$ with hDWs length L . The values are averaged between up and pu states (red circles in Fig. 2.5d). Red line is a fit to an exponential decay with the $L = 0$ value $i_{DW}^0 = 0.115$ and the decay length $L_0 = 47 \mu\text{m}$. Arrows indicate i_{DW}^0 values expected for naive non-interacting edge model (blue) and Luttinger liquid model in the absence of spin flip (red) and at spin-flip probability $r = 3/4$ (green), see text for details. Vertical arrow marks i_{DW} shift when $I_{dc} = 1 \text{ nA}$ is applied. In the inset i_{DW} dependence on large external dc current is plotted for $7 \mu\text{m}$ hDW for up and pu gates configuration right after the dc current is applied and before a measurable build-up of nuclear polarization.

for generating topological superconductivity. No neutral or spin modes appear within the K-matrix Luttinger liquid approach [103] in these isolated hDW models. In our case, moving beyond an isolated hDW model is needed to calculate the scattering of edge modes at a sample boundary by a hDW.

As calculated by our colleagues Prof. Yuli Lyanda-Geller and Prof. Vadim Ponomarenko, a map of an edge-hDW-edge structure onto one-dimensional bosonic modes $\varphi(x)$ is shown schematically in Figure 2.11a, considering two outgoing charge modes $\varphi_{pc}^{\rightarrow}(x_2)$ and $\varphi_{uc}^{\leftarrow}(x_1)$ and two outgoing spin/neutral modes $\varphi_{pn}^{\leftarrow}(x_1)$ and $\varphi_{us}^{\rightarrow}(x_2)$. In the strong coupling limit, charge, neutral and spin currents can be found by imposing the following boundary conditions

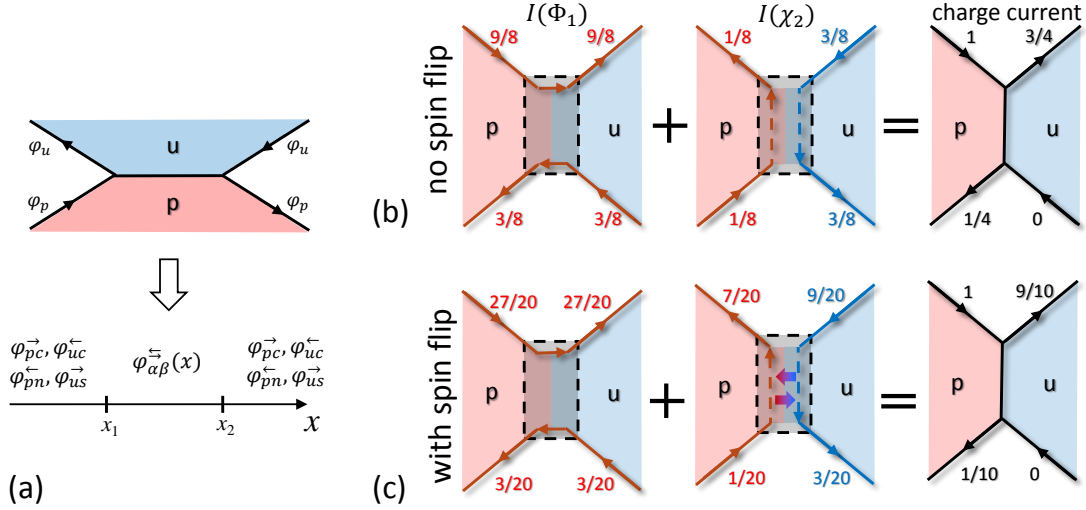


Figure 2.11. Schematic representation of currents: (a) Mapping of bosonic modes φ_α along sample edges onto a 1D Luttinger model modes $\varphi_{\alpha\beta}^{\rightarrow or \leftarrow}(x)$ for a domain wall with length $L = x_2 - x_1$. Subscripts $\alpha = \{p, u\}$ labels polarized and unpolarized phases, $\beta = \{c, n, s\}$ is for charge, neutral and spin modes and an arrow in the superscript specifies projection of the mode's group velocity. Arrows on the edges define chirality of edge channels. (b,c) Visualization of currents due propagation of Φ_1 and χ_2 modes without spin flips (b) and in the presence spin flips with the probability $r = 3/4$ (c) Red (blue) mode color indicates a spin-up (spin-down) polarization. Numbers indicate the fraction of the incoming current carried by the mode. Arrows correspond to directions of currents carried by corresponding modes.

on bosonic fields right outside of the hDW $[x_1, x_2]$. Our principal result is that imposing strong coupling boundary conditions in a general case of a domain wall of finite length results in the same currents flowing outside the domain wall as for the models of single-junction connecting edges on opposite sample boundaries, two junctions on opposite edges, and two junctions with scattering between same spin modes in between. Inside the domain wall, the chiral evolution of modes is controlled by the average voltage shifts at their corresponding boundaries. In the presence of voltage V , the only incoming mode changing due to charge injection in the p phase is $\varphi_{pc}(x_1)$, characterized by an average induced current $\bar{j} = \frac{e^2V}{3\pi\hbar}$. The detailed theoretic calculation can be found in ref.[110].

When spin-flip processes are absent, it is convenient to discuss the results in terms of currents carried by Φ_{1p} (Φ_{1u}) and quasiparticle $\chi_{2p} = (\varphi_{pc} - \varphi_{pn})/\sqrt{2}$ and $\chi_{2u} = (\varphi_{pc} -$

$\varphi_{ps})/\sqrt{2}$ modes. It is showed that Φ_{1p} (Φ_{1u}) modes propagate along the edges of the 2D gas and do not enter the domain wall, while χ_{2p} and χ_{2u} modes flow along the boundaries of p or u phases, including inside the domain wall, as shown schematically in Figure 2.11(b). Notable features of our solution are unequal distribution of carried currents between the modes caused by strong coupling to the domain wall and the presence of spin current along the edge of the u phase for $x > x_2$. The total current flowing along the hDW $I_{DW} = 1/4(I + I_{DW})$ or $i_{DW} = 1/3$. This value is three times larger than the experimentally measured i_{DW} and is indicated by a red arrow in Figure 2.10c.

In 2D gases formed in GaAs heterostructures spin transition at $\nu = 2/3$ is accompanied by a dynamic nuclear spin polarization [74]. Its main mechanism is the hyperfine coupling of electron and nuclear spins, which for QHE plateaus is usually suppressed due to a large difference between electron and nuclear Zeeman splitting. Near the u - p phase transition, however, electronic states with spin-up and spin-down are almost degenerate, enabling hyperfine coupling. This spin-flip mechanism can lead to the scattering between χ_{2p} and χ_{2u} modes propagating inside the domain wall, see Supplementary Materials of ref.[110]. Notably, Φ_1 modes still propagate along the 2D gas boundary and do not enter the domain wall. However, conservation of total current carried by Φ_1 and χ_2 modes results in the current redistribution between the modes. Domain wall current $i_{DW}(r)$ becomes a function of the spin-flip probability r and changes continuously between $1/3$ for $r = 0$ to zero for $r = 1$. Experimentally measured values correspond to $r \approx 3/4$, corresponding current are shown schematically in Figure 2.11c.

To test the role of spin flips it is possible to pass a large dc current and polarize nuclei in the vicinity of the tri-junction. Saturation of nuclear spin polarization is expected to create a bottleneck for electron spin flips and disable charge transfer between two χ_2 bosonic modes with opposite polarization. Indeed, application of $I_{dc} > 0.5$ nA results in approximately 3-fold increase of i_{DW} , as shown in the inset in Figure 2.10. A corresponding shift of i_{DW} for the $7 \mu\text{m}$ hDW is shown with a vertical arrow on the main plot. This shift is consistent with the 3 times current increase expected for the crossover from spin-flip-dominated to no-spin-flip transport.

2.7 Spin pumping with a dc current

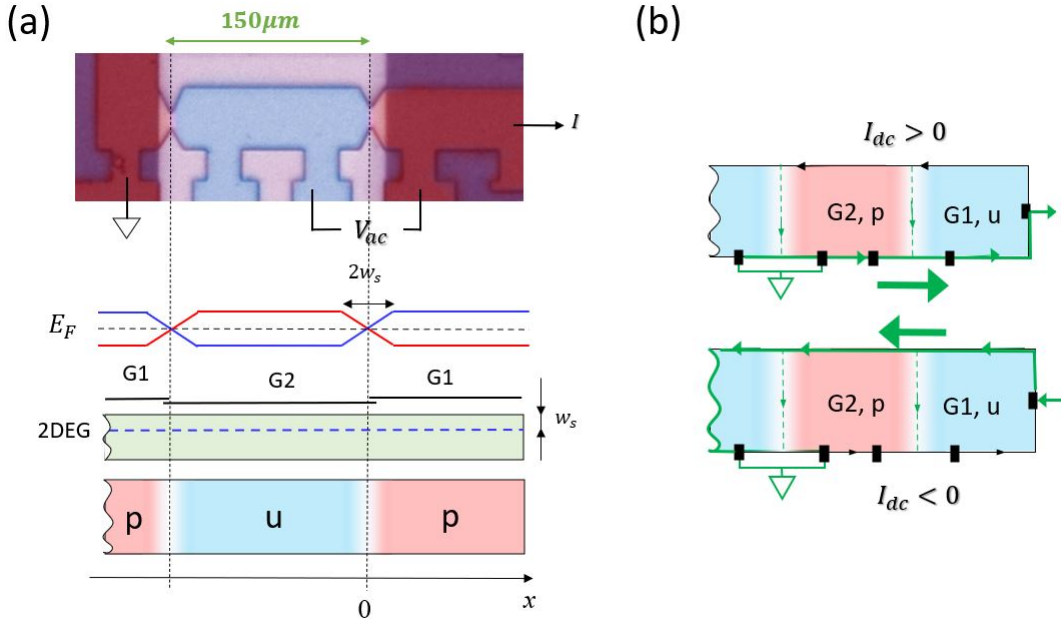


Figure 2.12. Schematic diagrams of spin pumping: (a) The top picture is a false color image of a typical device. 2D gas in red and blue regions is controlled by gates G1 and G2, in the purple area 2D gas is removed. The bottom schematic diagram displays the CF energy diagram, side view of device indicating positions of gates (G1 and G2) and 2D gas, and the controllable polarization state under each gate. Energy diagram represents the case when $\nu = 2/3$ state is polarized p under G1 and unpolarized u under G2. The 2D gas is 100nm below the surface (w_s). Density is controlled by two overlapping gates. Potential is expected to change within w_s from the gate boundary (white region). The vertical dashed line marks a physical boundary between G1 and G2. (b) Schematic diagrams of experiment configuration displaying electron flow (green arrows) with opposite dc current: the state is polarized under G1 and is unpolarized under G2.

Nuclear polarization can be used as a detector of electronic polarization. For example, by using optical pumped NMR, the decrease of Knight shift around $\nu = 1$ is strong evidence of the formation of skyrmions [83]. At filling factor $2/3$, a spin transition can happen and separate $2/3$ state into polarized state (spin $\uparrow\uparrow$) and unpolarized state (spin $\uparrow\downarrow$) [57]. Resistively detected NMR was used to confirm and study the electronic properties of this spin transition [52]. For $2/3$ state, previous studies focused on a multi-domain system, where

polarization was attributed to nuclear-electron hyperfine interaction. Here an experiment in a very controllable way is constructed with a single domain wall (see Figure 2.12). An application of large dc current leads to a build-up of nuclear polarization which results in a measurable shift of spin transition boundaries. Our experimental observation of nuclear polarization cannot be attributed to hyperfine interaction only and there should be some low-energy spin waves involved in the propagation of angular momentum.

Before starting the spin pumping experiment, a careful check of the stability of spin transition (magenta lines) without spin pumping is performed. Figure 2.13a shows a very small drift of spin transition after some time even without applying dc current. This small drift is attributed to density relaxation after applying non-zero gate voltage from zero gate voltage. Density relaxation drift for both gates is around -1.5mV and density should be stable after 2 hours (see Figure 2.13b). All the data for spin transition boundary shift due to none zero dc current or spin pumping are taken at least 2 hours later to provide enough time for density relaxation.

In our experiment, the system was first reset with zero net nuclear magnetization by applying zero gate voltages and by waiting for more than 2 hours for non-equilibrium nuclear polarization to decay. Then a map of spin transition boundaries (magenta lines) under G1 and G2 was measured with a small ac current of 0.13nA at a fixed applied magnetic field of 4.3T as shown in Figure 2.14a. After that, our system was gated in the way that the 2D gas is deep in u and p state under different gates and passed high dc current ($+1\text{nA}$ or -1nA) for several minutes, as shown schematically in the middle of Figure 2.14b. The time dependence of ac voltage (V_{ac}) crossing the gate boundary is recorded during the spin pumping process as shown in the top and bottom inserts of Figure 2.14b. Initially, V_{ac} is large due to the formation of a hDW, but after some time Δt , V_{ac} drops to zero. This V_{ac} change is due to the shift of the spin transition boundary under G2, as shown in Figure 2.14c, which shows a new corresponding map of spin transition boundaries under two gates after dc current is switched off. There are two important observations: (i) direction of the boundary shift depends on current direction, and (ii) sometimes only one boundary shifts (see Figure 2.14c).

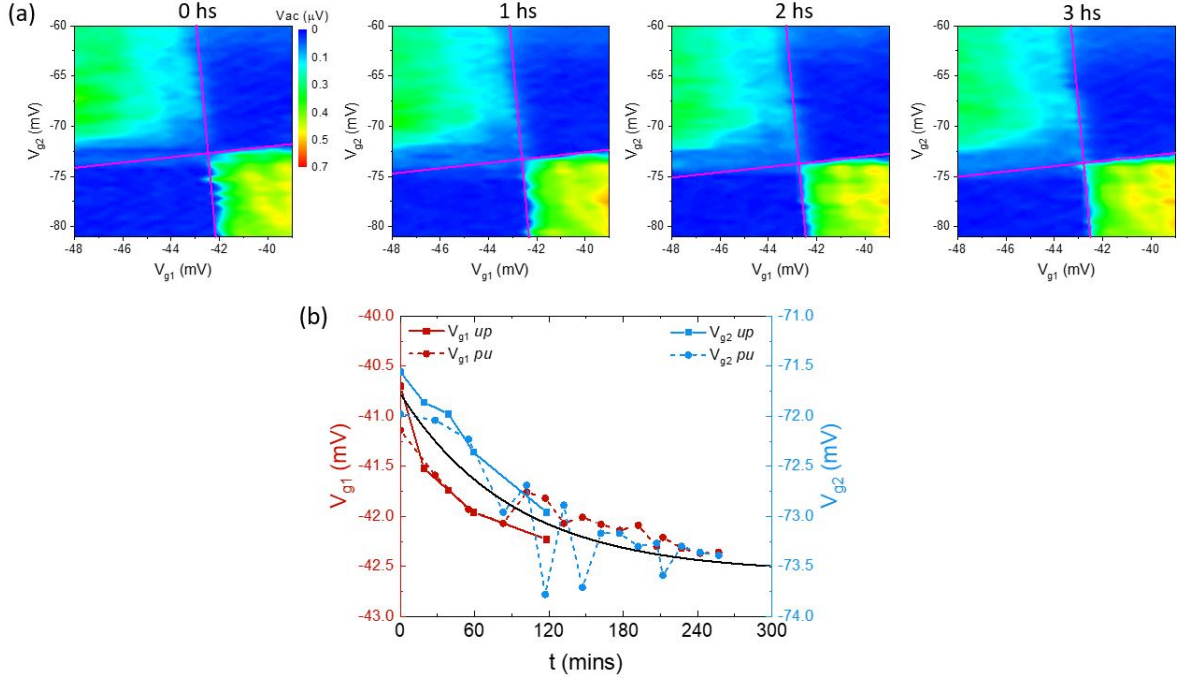


Figure 2.13. Density relaxation: (a) Time dependence of small drift of spin transition boundary (magenta lines) with zero dc current: these plots of ac voltage cross gates boundary as a function of gate voltages are taken every one hour. (b) Drifts of spin transition boundary under G1 (red curves) and G2 (blue curves) as a function of time with zero dc current.

The spin transition is determined by the ratio of Coulomb energy and Zeeman energy $\eta^* = E_C/E_Z$. In our work, the whole regime of $\nu = 2/3$ state does not shift, indicating no change of the orbital term or Coulomb energy. Therefore, the observation of shifts of spin transition is due to the change of Zeeman energy. The total field felt by electron spin is $B_Z = B_{ext} + B_n$, where B_{ext} is applied magnetic field and B_n is the Overhauser field created by nuclear polarization. In our work, we call the shift of the spin transition in this case the Overhauser shift which can be inversely used to detect the nuclear bath polarization and distinguish different mechanisms of nuclei-electron interaction.

This paragraph will discuss what is expected if only nuclear-electron hyperfine interaction is considered. For a simplified picture (see Figure 2.15a) when an electron is injected from u

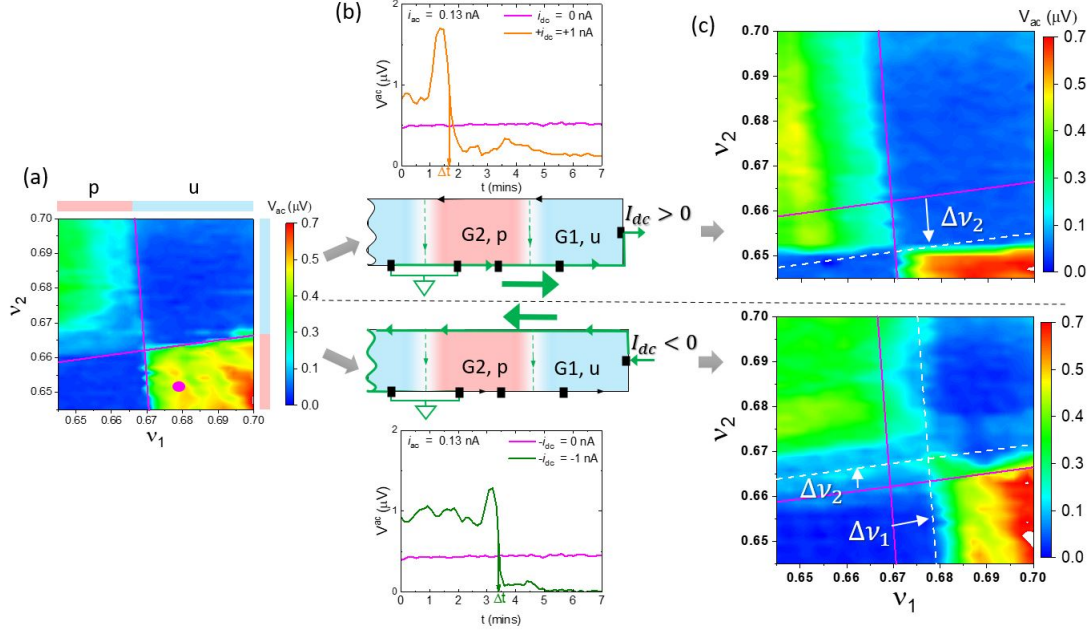


Figure 2.14. Shift of spin transition boundary: (a) Ac voltage as function of ν_1 and ν_2 before spin pumping. The magenta solid line and magenta point marks the spin transition boundary and pumping point which indicates the pu state in hDW in this case. (b) Middle: Schematic diagrams of experiment configuration with opposite dc current when the state is polarized under G1 and is unpolarized under G2. Top and bottom: Corresponding time dependence of ac voltage crosses the gates boundary. Δt indicates the total pumping time. (c) Corresponding ac voltage as function of ν_1 and ν_2 after spin pumping. The white dashed lines indicate new spin transition boundaries after spin pumping.

to p state, electron spin-flip from down to up will occur at the hot spot (the red star). The hamiltonian of nuclear-electron hyperfine interaction can be written as:

$$H_{HF} \propto A_H I \cdot S = \frac{A_H}{2} (I^+ S^- + I^- S^+) + A_H I_Z S_Z \quad (2.1)$$

where $A_H = 40 - 50 \mu\text{eV}$, I and S are interaction term between electron and nuclear for relevant ions (^{69}Ga , ^{71}Ga , ^{75}As), nuclear and electron spins respectively. Hyperfine interaction will happen when both spin conservation ($\Delta S + \Delta I = 0$) and energy conservation ($E_{\Lambda_{1\uparrow}} - E_{\Lambda_{0\downarrow}} = \hbar\gamma_n B_e \approx 0.03 \mu\text{eV}$) are satisfied, which should be the case, along the heli-

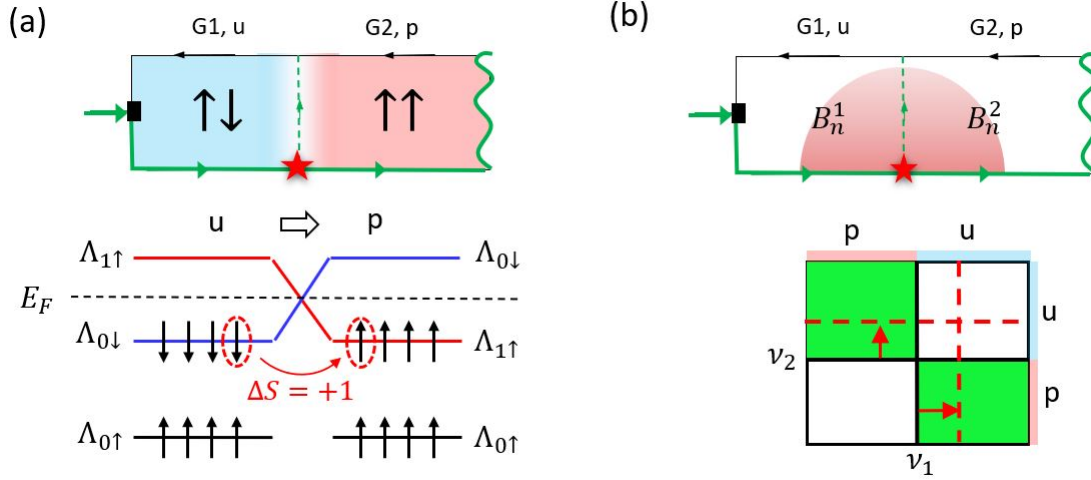


Figure 2.15. Electron spin flip and nuclear-electron hyperfine interaction: (a) Schematic diagram showing electron spin flip at hot spot when electron is injected from unpolarized state to polarized state: the change of electron spin is $\Delta S = +1$. (b) Expected shift of spin transition with hyperfine interaction only.

cal domain wall. Zeeman energy is proportional to the sum of external magnetic field and Overhauser field: $E_Z = g^* \mu_B (B_{ext} + B_n)$. Here the Overhauser field can be written as:

$$B_n = \frac{A_H \langle I_Z \rangle}{g^* \mu_B} = \frac{A_H \langle I_Z \rangle}{-|g^*| \mu_B} \quad (2.2)$$

Since g-factors of electron and nuclei have different signs, positive electron spin-flip $\Delta S = +1$ is compensated by nuclear spin-flip $\Delta I_Z = +1$ and results in a positive Overhauser field ($B_n > 0$) and positive shift of spin transition line under both gates as shown in the bottom insert of Figure 2.15b. Nuclear spins are expected to diffuse uniformly via dipole-dipole interaction from the hot spot, as schematically shown in the top insert of Figure 2.15b, and what is expected to be observed is almost identical Overhauser fields $B_n^1 \approx B_n^2$ under the two gates. Similarly, when the electron spin-flip is negative, a negative Overhauser field and a negative shift of spin transition line will be detected when only hyperfine interaction occurs. The comparison between the expected and measured shifts of spin transition for different configurations are shown in Figure 2.16. For $I_{dc} < 0$, there are two different types of hot spots as labeled by blue and red stars, depending on the sign of the spin-flip. A positive shift

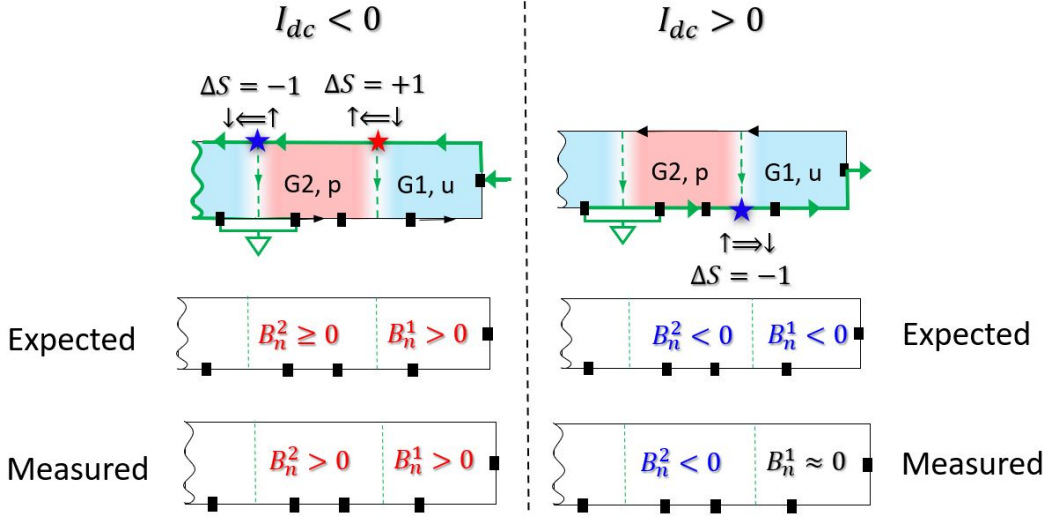


Figure 2.16. Overhauser field change with nuclear-electron hyperfine interaction only: Schematic diagrams showing comparison between the expected and measured change of Overhauser field according to shifts of spin transition for a certain experimental configurations with $\pm I_{dc}$ if only nuclear-electron hyperfine interaction is considered.

under G1 and a smaller positive shift under G2 are expected to be seen. The experimental result is almost consistent with expectation. The observed omnidirectional propagation of nuclear polarization is consistent with nuclear electron hyperfine interaction. For $I_{dc} > 0$, there is only one hot spot which indicates the negative electron spin-flip $\Delta S = -1$. Both negative shifts under two gates due to hyperfine interaction are expected to be observed. But experimental results only show shift under G2, indicating a unidirectional propagation of nuclear polarization.

Now we include a spin wave picture (see Figure 2.17) to understand this asymmetry shift of the spin transition line. Hyperfine interaction only will give us identical negative Overhauser fields under two gates which is inconsistent with real experimental results. In order to achieve the unidirectional nuclear polarization, one requires an efficient generation of low-energy spin waves in the polarized state. Combining with the positive spin-flip, of which the experimental result is consistent with hyperfine interaction, the spin wave picture needs to satisfy the following ingredients: (1) spin wave can only be generated and propagated in a polarized (ferromagnetic) state but not in an unpolarized (paramagnetic) state, (2)

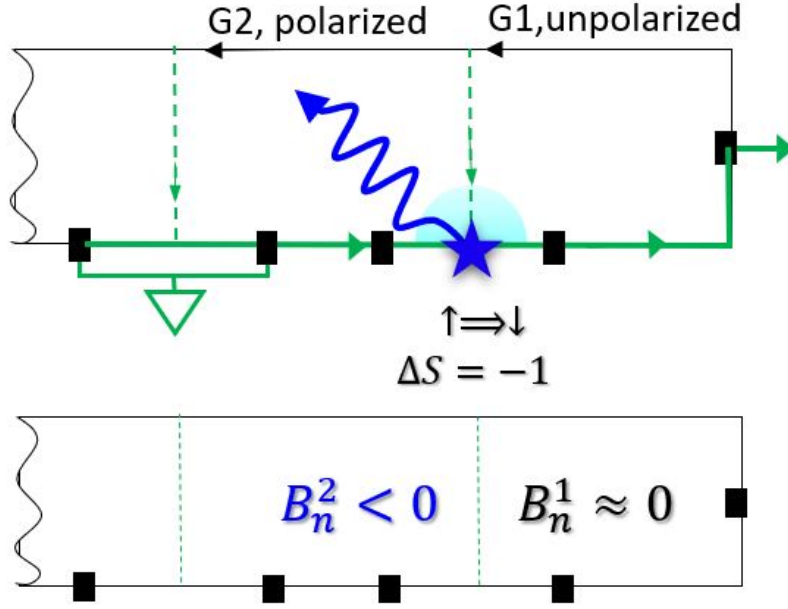


Figure 2.17. Schematic diagram of spin wave picture: The blue wave illustrates the propagation of spin wave from the hot spot, and the light blue semi-disk indicates nuclear spin diffusion (nuclear dipole-dipole interaction).

probability of the emission of this spin wave is much higher than that of the nuclear-electron hyperfine interaction, (3) spin wave is momentum selective ($\Delta S = -1$), (4) spin wave can interact with nuclear, indicating the energy of the spin-wave is very low ≈ 0 . Spin wave interacting with nuclear indicates the presence of spin textures in the polarized state.

Magnon (or a spin wave magneto-roton [111]) is momentum selective and is allowed in the ferromagnetic (FM) polarized state and cannot propagate in the paramagnetic unpolarized state. However, magnon is a high-energy excitation and cannot interact with nuclei directly. Thus, in the p state there should be low energy spin modes and there should be a mechanism for magnons to relax into low energy modes without losing angular momentum. The following model may be able to explain the measurements: (i) fractional skyrmion crystal is formed in the p state and (ii) only trivial quasiparticle excitations are supported in the gradient p state near the gate boundary. In this model, magnons propagate freely into the bulk of the FM p state and need to lose energy to interact with nuclei. The middle of the p state is at $\nu \approx 0.648$ or $\nu^* = 2.2$ for CF. For a similar density deviation from a middle of the

QHE plateau skyrmion crystals were observed near $\nu = 1$ and $\nu = 1/3$. Whether skyrmion or trivial quasielectron is the lowest excitation is controlled by the ratio $\kappa = E_Z/E_C$ and it was calculated [112] that at $\nu = 1/3$ skyrmions are stable for $\kappa < 0.0009$. At $B=4.2\text{T}$ $\kappa = 0.012$ and, compared to $\nu = 1/3$, E_C is further reduced due to the screening from $\Lambda_{0\uparrow}$ level, but E_Z is replaced by the smaller $\Lambda_{0\downarrow} - \Lambda_{1\uparrow}$ gap. Let's assume that skyrmions can be formed. Isolated skyrmionic excitations have a gap $> E_Z$. Skyrmion crystal has low energy spin excitations, these Goldstone modes are known to be responsible for strong interactions with nuclei [113].

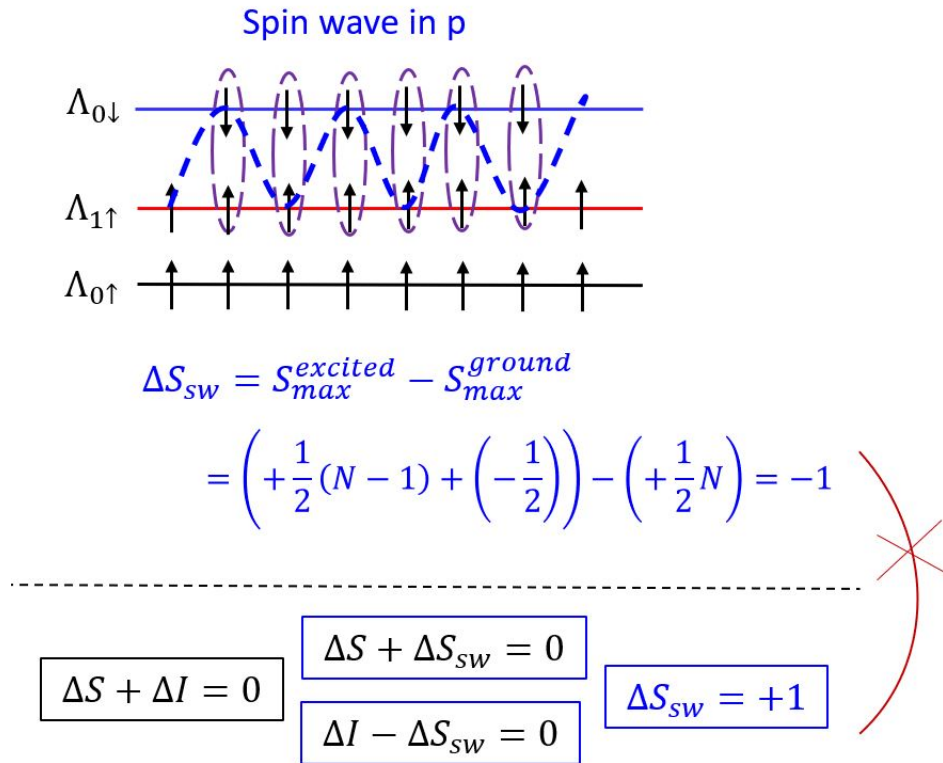


Figure 2.18. Sign of angular momentum change of spin wave: Negative sign of angular momentum change of spin wave $\Delta S_{sw} = -1$ deduced from collective mode in FM p state is inconsistent with $\Delta S_{sw} = +1$ result from spin conservation among electron spin, nuclear spin and spin wave.

However, there are still a number of open questions remained for this model. Is it possible that skyrmions are unstable in the presence of a potential gradient? This is a necessary ingredient to create a buffer between the degeneracy point ($x=0$ in Figure 2.12a) and the

skyrmion crystal with low energy modes. Can the gradient of quasiparticle density in this region play a role and destabilize skyrmion formation? Or, somehow, the presence of both electric and magnetic fields results in a force on a spin texture (as is the case for vortices) and an extra elastic energy due to the pinning of the skyrmion-associated charges, which makes texture formation energetically unfavorable? The major problem with magnon or spin-wave generation picture, though, is that the sign of ΔS is opposite to the angular momentum of magnon as shown schematically in Figure 2.18. The physical origin of the unidirectional propagation of the nuclear polarization is yet to be understood.

2.8 Transport discussion of Quasi-Corbino (qC) device

Devices with quasi-Corbino geometry (qC) are fabricated from two GaAs/AlGaAs heterostructures with electron gas density and mobility $0.9 \cdot 10^{11} \text{cm}^{-2}$ and $4.95 \cdot 10^6 \text{cm}^2/\text{Vs}$ (wafer A:LE40), and $1.3 \cdot 10^{11} \text{cm}^{-2}$ and $3.8 \cdot 10^6 \text{cm}^2/\text{Vs}$ (wafer B:LE25). A photograph of a typical qC device, of which contacts are fabricated within the interior of the device, fabricated from wafer A is shown in Figure 2.19. Devices are divided into two regions by semi-transparent gates (10 nm of Ti), the gates are separated from the surface of the wafer and between each other by 50nm of Al_2O_3 grown by the atomic layer deposition. Ohmic contacts are formed by annealing Ni/AuGe/Nb/NbN 30nm/154nm/5nm/7nm, in a H_2/N_2 atmosphere (forming gas). A 2DEG is created by shining red LED at ~ 4 K. In qC devices, actual Ohmic contacts ($\sim 10 \times 15 \mu\text{m}^2$) are formed along the boundary between two gates. In this design of qC device there is a single boundary with multiple contacts, while in another design of qC device (fabricated from wafer B), there is a central contact and four more contacts in a star formation. The actual length of hDW L in qC devices is smaller by the out-diffusion of AuGe contacts during thermal annealing. In different devices L varies between $2 - 100 \mu\text{m}$. In qC devices, one section of the gate boundary is patterned as a $1550 \mu\text{m}$ meander, reaching the edge of the mesa. Measurements were performed in a dilution refrigerator at a base temperature of 20 mK using standard lock-in technique at 17.7 Hz in 2-terminal ($V_{ac} = 5$ or $10 \mu\text{V}$) configuration. Gate voltages (V_{g1} and V_{g2}) were applied through a homemade digital-to-analog converter (DAC) to control the electron gas density. Here

$V_g = (V_{g1} + \alpha V_{g2})/2$ controls overall densities under gates G1 and G2 (coefficient $\alpha = 0.75$ accounts for the difference in oxide thickness under the gates), and $dV_g = V_{g1} - \alpha V_{g2}$ controls density difference. Density is uniform across the whole device for $dV_g = 0$. FQHE states are better developed under G2 with thicker oxide.

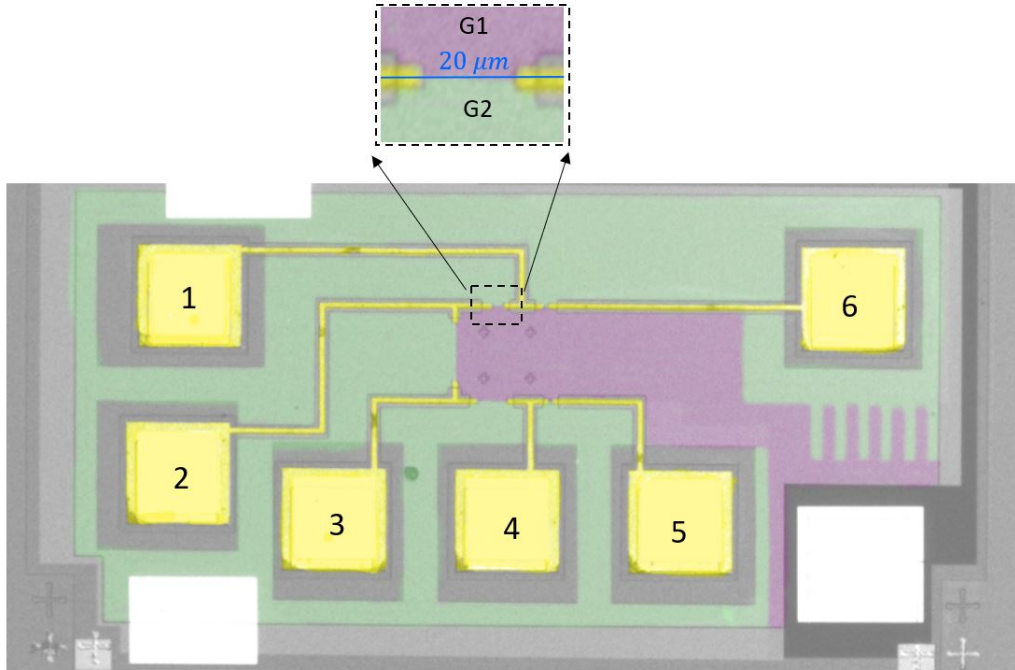


Figure 2.19. Photography of a qC device fabricated from wafer A: A false color image of a typical qC device: yellow regions are Ohmic contacts, 2D gas in green and magenta regions is controlled by gates G1 and G2, in the grey area 2D gas is removed. The thin horizontal blue line marks a physical boundary between G1 and G2. A two-terminal measurement is applied with small ac voltage ($5 - 10\mu V$) from contact 1 to contact 2 and ac current is measured at the same time.

The chiral channel measurements were firstly checked both in IQHE and FQHE regions. A 2-terminal measurement was used for qC geometry. According to Landauer-Büttiker approach, when a chiral channel is formed between two neighboring filling factors, a 2-terminal conductance along the gate boundary should be $G_{chiral}^{qC} = G_q$ for IQHE regime ($G_{chiral}^{qC} = (\nu_1 - \nu_2) \cdot G_q$ for FQHE regime). Here ν_1 and ν_2 represent the filling factors under the two gates and $R_q = 1/G_q = \frac{h}{e^2}$.

For our qC device, an asymmetry of the chiral channel ($1/3$ - $2/5$ or $2/3$ - $3/5$) depending on the sign of dV_g (density gradient) was observed, as Figure 2.20ab. This asymmetry indicates that the quality of electron gas under G1 is not as good as that under G2. However, a quantized plateau was measured for the chiral channel between $\nu = 1/3$ and $\nu = 2/5$ states. For 2-terminal measurement, contact resistances also contributed to experimentally measured values. Contact resistance can be extracted by measuring the known resistance of chiral channels. It was found that the contact resistance increases with the magnetic field, as Figure 2.20d shown. For $B \approx 4.3T$, the contact resistance is estimated to be less than $5k\Omega$, which is a small correction to our experimental resistance ($> 100k\Omega$) along the gates boundary with different polarizations of the $\nu = 2/3$ state.

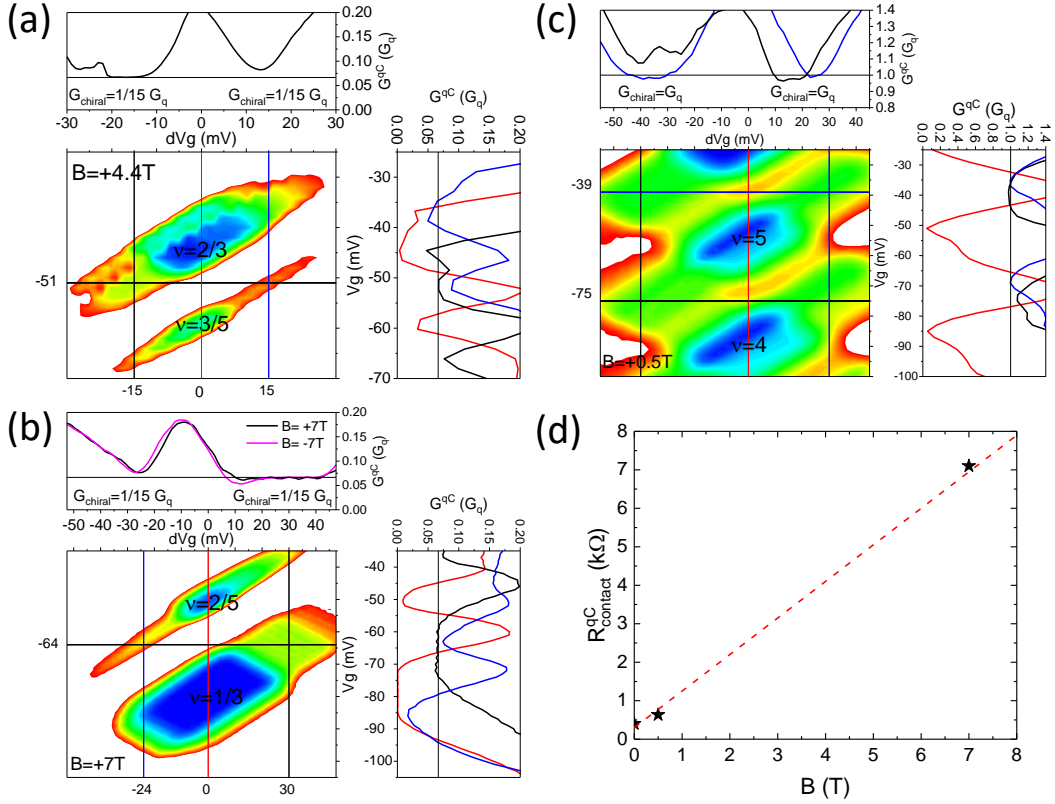


Figure 2.20. Formation of chiral edge channel in gated quasi-Corbino device fabricated from wafer A: (a)(b)(c) Two-terminal chiral measurement in the IQHE regime and the FQHE regime ($2/3$ and $3/5$ or $1/3$ and $2/5$), (d) Contact resistance vs. magnetic field extracted from chiral measurement.

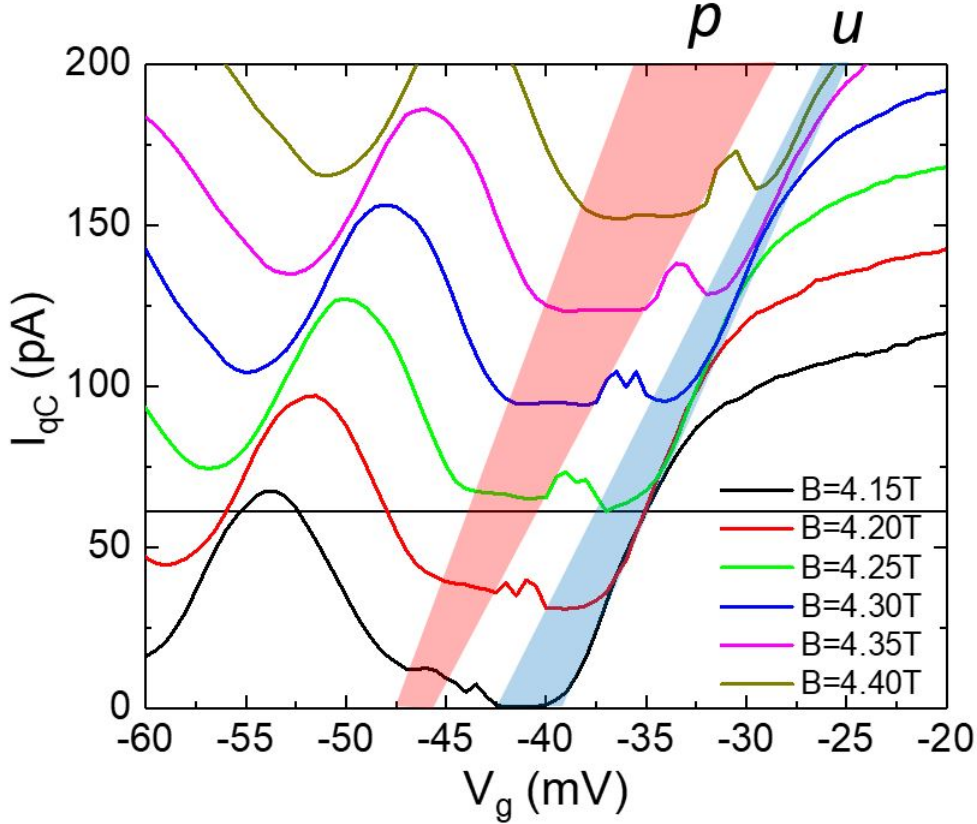


Figure 2.21. Gate and field dependence of spin transition around $\nu = 2/3$ with $dV_g = 0$ for qC devices fabricated from wafer A: Curves are off-set by 25 pA for clarity. Unpolarized (u) state (blue area) becomes polarized (p) state (red area) after spin transition peak. Black horizontal line indicates the position of a zero current expected for a well-developed FQHE state.

Field evolution of current in the vicinity of $2/3$ as a function of V_g for the qC device is shown in Figure 2.21. The $\nu = 2/3$ plateaus is interrupted by a small peak. The height of this peak has strong current dependence, as well as hysteresis with respect to the field sweep and gate sweep direction at high excitation currents. These characteristics are consistent with previous studies of spin phase transitions [24], and we identified these peaks as a signature of spin transition in our samples. Magnetic field was tuned to maximize the gaps between the p and u states. For HB geometry, the width of the spin transition peak is ~ 3 mV, which is only $\sim 25\%$ of the total plateau width of ~ 11 mV. The width of the $\nu = 2/3$ plateau for our qC geometry is ~ 6 mV, which is larger than that in the HB geometry. Besides, a small

leakage (nonzero value indicated was observed by a small offset marked by a black horizontal line in Figure 2.21) through bulk for p or u state in the qC geometry. Moreover, the QHE states in the qC geometry are harder to observe than in the HB geometry [114]. However, the qC geometry is important if we want to introduce superconductivity from superconducting contacts to create a fractional topological superconductor.

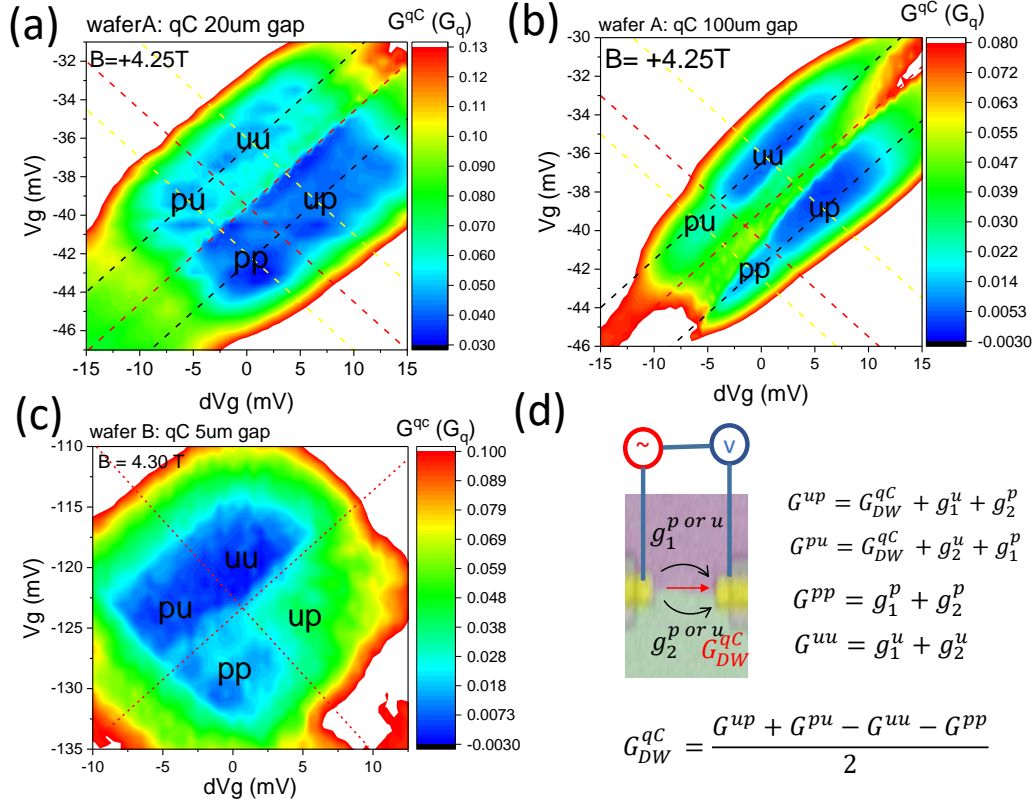


Figure 2.22. Helical channel measurement at $\nu = 2/3$ for quasi-Corbino (qC) geometry: (a)(b)(c) Conductance as a function of V_g and dV_g for different qC gaps (or lengths of gates boundary). (d) Schematic diagram for the case that current leaks through bulk: helical channel measurement in qC geometry is sensitive to bulk leakage.

For a qC geometry, the leakage from bulk affects the 2-terminal conductance. For chiral measurement in qC geometry, the bulk leakage can be accounted for by using a simple parallel resistor model, see Figure 2.22. The conductivity of chiral channel is corrected by $G_{chiral}^{qC} = (g_1^{chiral} + g_2^{chiral} - g_n - g_{n+1})/2$, where g_n and g_{n+1} are bulk leakage conductance for neighboring filling factors. This adjustment can restore the proper quantized chiral channel

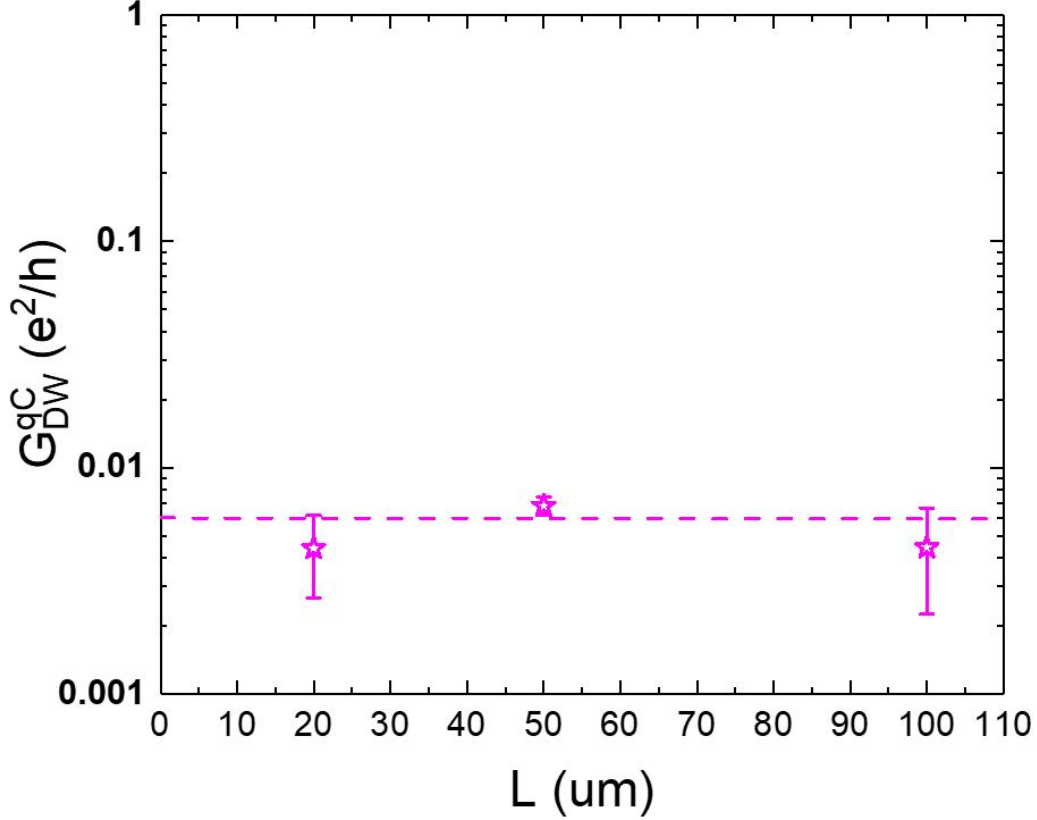


Figure 2.23. Conductance of the helical channel as a function of propagating length for the qC geometry.

within 4% precision while it will deviate 20% if the bulk contribution is ignored. Like the helical measurement of the HB geometry, what is expected are four quadrants separated by spin transition lines in our qC geometry. Instead of zero resistance for uu and pp states in the HB geometry, zero conductance using a two-terminal probe in our qC geometry should be measured. In this geometry, the conductance of a fractional helical channel (up and pu states) is expected to be measured directly. Figure 2.22ab shows the conductance at $\nu = 2/3$ as a function of V_g and dV_g for 20 and 100 μm lengths of gates boundary. A nonzero conductance for uu and pp states is observed, indicating certain bulk leakage. The conductance of the helical channel in our qC geometry can be extracted as $G_{DW}^{qC} = \frac{G^{up} + G^{pu} - G^{uu} - G^{pp}}{2}$, Figure 2.22d. The conductance of the helical channel for the 20 μm qC gap is 10 times smaller than that estimated from the HB geometry. For 100 μm gap, up state shows some conductance while pu state is very insulating. And a higher leakage is observed in uu state than in pp

state. Moreover, the quality of electron gas under G1 is worse than that under G2. Thus, only pu state shows the best quality of the formation of a helical edge channel. However, the conductance of pu state is even smaller (more insulating) than pp and uu states. It indicates that no conducting domain wall is formed for pu state for a $100 \mu m$ gap. A different qC geometry was fabricated from wafer B. The corresponding helical channel measurement is shown in Figure 2.22c for a $5 \mu m$ gap. The behavior of this helical channel is similar to what is observed for $100 \mu m$ gap from wafer A: up state shows certain conductance while pu state is insulating and pu state is even more insulating than pp and uu states. However, the conductance of up state for the $5 \mu m$ gap from wafer B is higher than the conductance for the $100 \mu m$ gap from wafer A. This may still indicate certain length dependence behavior. Figure 2.23 shows conductance of the DW ($G_{DW}^{qC} = \frac{G^{up} + G^{pu} - G^{uu} - G^{pp}}{2}$) for the qC geometry as a function of DW length. There is almost no length dependence for the helical channel in qC geometry and $G_{DW}^{qC} \approx 0.006 \frac{e^2}{h}$.

This observation indicates that conduction of helical channels in qC differs from HB measurements. This difference may be related to the Fermi level adjustment in the vicinity of Ohmic contacts and formation of an insulating barrier for carriers injection. This effect is expected to be less prominent for chiral channels.

2.9 Conclusions

In summary, we proposed that domain walls formed during ferromagnetic spin transitions in the fractional quantum Hall effect regime can be used as building blocks to form topological superconductors that support parafermion excitations. We demonstrated that in triangular quantum wells, spin transitions can be controlled locally by electrostatic gating, and conducting helical domain walls can be formed in multi-gate devices. Such local control allows the formation of reconfigurable networks of domain walls. In the presence of proximity-induced superconducting coupling, the system becomes a reconfigurable network of one-dimensional topological superconductors with parafermion excitations.

We investigated transport properties of hDWs in the $\nu = 2/3$ fractional QH regime in HB geometry. Experimentally, we found that current carried by hDWs is substantially

smaller than the prediction of the naïve model. Luttinger liquid theory of the system reveals redistribution of currents between quasiparticle charge, spin and neutral modes, and predicts the reduction of the hDW current. Inclusion of spin-non-conserving tunneling processes reconciles theory with experiment. The theory confirms emergence of spin modes required for the formation of fractional topological superconductivity.

We also studied DW channels in a quasi-Corbino (qC) geometry by directly contacting the hDW with Ohmic contacts. We are able to measure proper quantized chiral channels in the IQHE and FQHE regimes. However, we found hDWs in qC device to be almost insulating with no length dependence. The difference between HB measurement and qC measurement may indicate that it is easier to inject carriers into helical channels from chiral edges than from Ohmic contacts.

3. CONTROL OF HELICAL STATES IN TOPOLOGICAL INSULATOR

Parts of this work are submitted to Phys. Rev. Mater., arXiv:2106.09771, and are still in preparation.

3.1 Introduction

Eu chalcogenides are magnetic insulators that host one of the highest magnetic saturation moments per atom, owing to a partially filled Eu 4f-shell. A renewed interest in these materials is motivated by a possibility to induce strong Zeeman spin-splitting when interfaced with topological insulators and superconductors. Topological insulators (TIs) are characterized by the presence of topologically protected gapless surface states (TSSs) with spin-momentum locking [87] that are both a blessing and a curse for TI-based devices: on one hand, they are protected by time-reversal symmetry; on the other, the geometry of TSS cannot be constrained by simple lithographic techniques. There are many applications where selective gapping of TSS would be desired, for example quantum anomalous Hall effect requires gapping of top and bottom surfaces [115]–[117], spintronic devices may benefit from an ability to gap the side TSS and, thus, electrically disconnect top and bottom TSSs [118], while in TI-based topological superconductors selective gapping of TSS is required in order to localize non-Abelian excitations [119].

Globally, time-reversal protection of TSS can be lifted by strong external magnetic fields [120] or via bulk doping of a TI with magnetic impurities [121]–[124]. It has been suggested that local control of TSS can be achieved by coupling a TI to a magnetic material [125], [126]. Opening of an exchange gap in the Dirac spectrum of TSS has been reported in Bi_2Se_3/EuS heterostructures, where ferromagnetic insulator *EuS* proximity-induce ferromagnetism in the TI surface [127]. Polarized neutron reflectometry detected interfacial magnetization in these heterostructures up to room temperature, 20 times higher than the Curie temperature $T_c = 17$ K of the bulk *EuS* [96]. Such large T_c enhancement has not been seen in subsequent studies [128]. Gapping of TSS by exchange-coupling to an anti-ferromagnetic insulator has an advantage of reduced stray magnetic fields from the bulk of the magnetic material and

has been demonstrated in magnetically doped TI interfacing Cr_2O_3 [129] and $CrSb$ [130]. There are currently no reports of both top and bottom TSS modulations in non-magnetic TIs, which motivates further investigation of TI/material interface formation and the nature of interfacial magnetic exchange.

$EuSe$ is an insulating metamagnetic material with almost perfect cancellation of the nearest and next-nearest neighbor interactions between localized magnetic moments on the half-filled 4f levels of Eu^{2+} ions [131]. This cancellation leads to a phase diagram which includes several anti-ferromagnetic (AF-I $\uparrow\downarrow\uparrow\downarrow$, AF-II $\uparrow\uparrow\downarrow\downarrow$), ferrimagnetic (FiM $\uparrow\downarrow\uparrow$) and ferromagnetic (FM) phases in the bulk, where magnetization vectors are confined to the (111) plane of the NaCl-type crystal structure (as shown in Figure 3.1). There are two types of magnetic domain along (111) plane [132]: T (twin) domain, which has a triclinic symmetry and can be eliminated by a large ($> 0.2T$) external magnetic field, and S (spin rotation) domain as illustrated by the red arrows in Figure 3.1ab. It would be of great interest to control orientation of $EuSe$ during MBE growth, to enable proximity with both the ferromagnetic (111) and the antiferromagnetic (100) surfaces. The relative strength of magnetic phases and positions of phase boundaries are also highly sensitive to strain and can be tuned during epitaxial growth [133], [134]. The magnetic properties of bulk $EuSe$ and thin layers grown on IV-VI materials have been studied in the past [133], [135], [136], however, the growth and characterization of $EuSe$ thin films has yet to be performed on a variety of other substrates of interest to study TIs.

Here I first discuss the molecular beam epitaxy (MBE) growths, which has been performed by our collaborators Dr. Xinyu Liu and Prof. Badih A. Assaf at University of Notre Dame, and magnetic characterization of thin $EuSe$ films on different substrates followed by discussion of magnetic characterization and signatures of induced magnetic exchange between Bi_2Se_3 , TSSs and $EuSe$. We synthesize $EuSe$ on $GaAs(111)B$, Bi_2Se_3 , and the lattice matched $BaF_2(111)$ and $Pb_{1-x}Eu_xSe(111)$. It is found that a (001) oriented $EuSe$ can be obtained on $GaAs(111)B$ and Bi_2Se_3 enabling an antiferromagnetic proximity effect, while growth on $BaF_2(111)$ and $Pb_{1-x}Eu_xSe(111)$ yield a (111) oriented layer. The magnetic properties of both types of samples are studied and the Néel temperature are extracted. Un-

expectedly, we observe that the FiM-to-AFM transition in $EuSe$ is significantly broadened in these films and show a large hysteresis as a function of magnetic field scan direction.

Polarized Neutron Reflectivity (PNR) showed a reduction of in-plane magnetization at the interface between $EuSe$ and Bi_2Se_3 when bulk $EuSe$ is ferromagnetic. Combined with transport data, where no magnetic hysteresis was observed in magneto-conductance below 0.5T, it suggests AFM coupling instead of FM coupling as has been reported at the EuS/Bi_2Se_3 interface. Modulation of magneto-conductance above 0.5T in microscopic samples indicates reconfiguration of AFM domains at the interface.

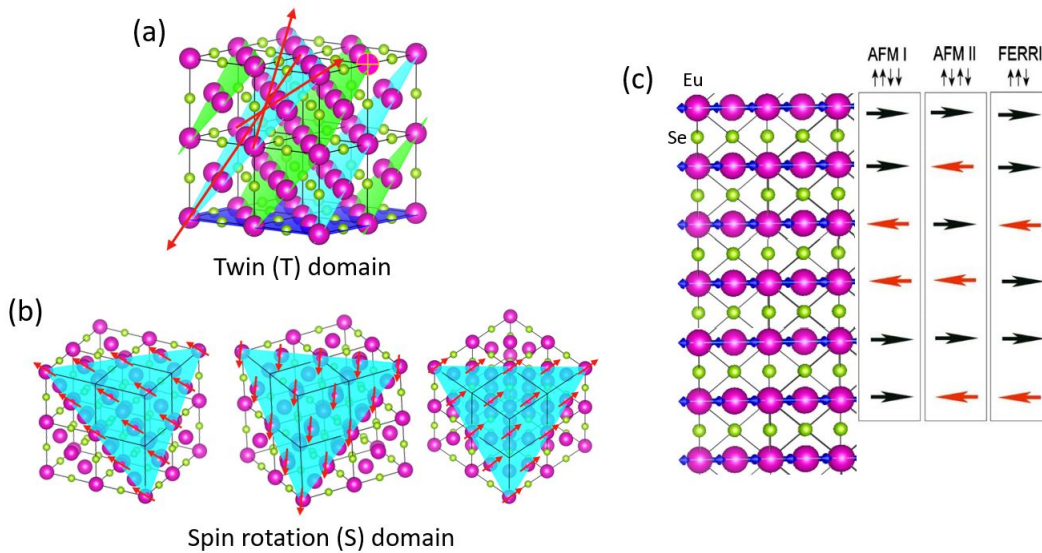


Figure 3.1. Structural and magnetic orderings of $EuSe$: (a)(b) Fcc crystal structure of $EuSe$ with T domain or S domain. The small and green balls represent atom Se, while the large and purple balls represent atom Eu, which form (111) planes (green and cyan planes). The red arrows indicate a T domain (or S domain). (c) Left: the fcc lattice of $EuSe$ is schematically represented along (111) direction. Right: the three observed magnetic orderings (AFM-I, AFM-II and FERRI) with different spin alignments in successive Eu atomic layers when viewed from a (111) equivalent direction.

3.2 Material growth and structural characterization.

The $EuSe$ thin epilayers were grown by MBE on three types of substrates and buffer layers: (SA) lattice mismatched $GaAs$, (SB) nearly-lattice matched BaF_2 (111), (SC) $Pb_{1-x}Eu_xSe/BaF_2$

Table 3.1. List of *EuSe* thin films on different substrates.

Sample label	substrate	growth sequence	thickness (nm)	R_a (nm)	<i>EuSe</i> growth direction	T_N (K)	<i>EuSe</i> OFP strain (%)
SA1	<i>GaAs</i> (111)B	<i>EuSe</i>	120	2.96	(001)	5.1	-0.001
SA2	<i>GaAs</i> (111)B	<i>EuSe</i>	120		(001)&(111)	5.4	+0.09
SB	<i>BaF₂</i> (111)	<i>EuSe</i>	90	2.58	(111)	4.9	-0.09
SC	<i>BaF₂</i> (111)	<i>Pb</i> _{0.575} <i>Eu</i> _{0.425} <i>Se</i> / <i>EuSe</i> / <i>Bi₂Se₃</i>	/43 /20 /28	0.979	(111)	5.5	+0.65
SD1	Sapphire	<i>Bi₂Se₃</i> / <i>EuSe</i>	16.6 /20	0.886	(001)	4.4	-0.08
SD2	<i>GaAs</i> (111)B	<i>Bi₂Se₃</i> / <i>EuSe</i>	18.8 /8.2	1.74	(001)&(111)	4.4	+0.11
SD3	Sapphire	<i>Bi₂Se₃</i> / <i>EuSe</i>	16.6 /9.8	1.06	(001)	3.7	-0.19
SE	<i>BaF₂</i> (111)	<i>EuSe</i> / <i>Bi₂Se₃</i>	50 /14	2.04	(111)	5.2	-0.09
SF	<i>GaAs</i> (111)B	<i>EuSe</i> / <i>Bi₂Se₃</i> / <i>EuSe</i>	9.9 /16.5 /6.7	1.96	(001)&(111) (001)	4.4	+0.05

Properties of *EuSe* films studied in this work: Films thickness is determined from MBE growth calibration and confirmed for several films by tunneling electron microscopy (TEM) imaging. RMS surface roughness R_a is extracted from atomic force microscopy (AFM) images (see Figure 3.2). The dominant crystal orientation is determined by XRD. Occasional (111) inclusions are detected by TEM but not by XRD. The Néel temperature is extracted from temperature dependence of magnetic susceptibility. The out-of-plane (OFP) strain is estimated based on the out-of-plane lattice constant measured by XRD.

(111) pseudo-substrates, (SD) 2-dimensional van-der-Waals *Bi₂Se₃* epilayers grown on sapphire. Table 3.1 summarizes parameters of the samples. High-purity *PbSe* compound flux, and *Eu*, *Bi*, and *Se* elemental fluxes are obtained from standard effusion cells. The growth is monitored by in situ reflection high energy electron diffraction (RHEED). During the growth process, the substrate temperature is kept at 300°C and the growth is carried out under Se-rich condition. The *Se* flux is kept constant at the beam equivalent pressure (BEP) ratio of

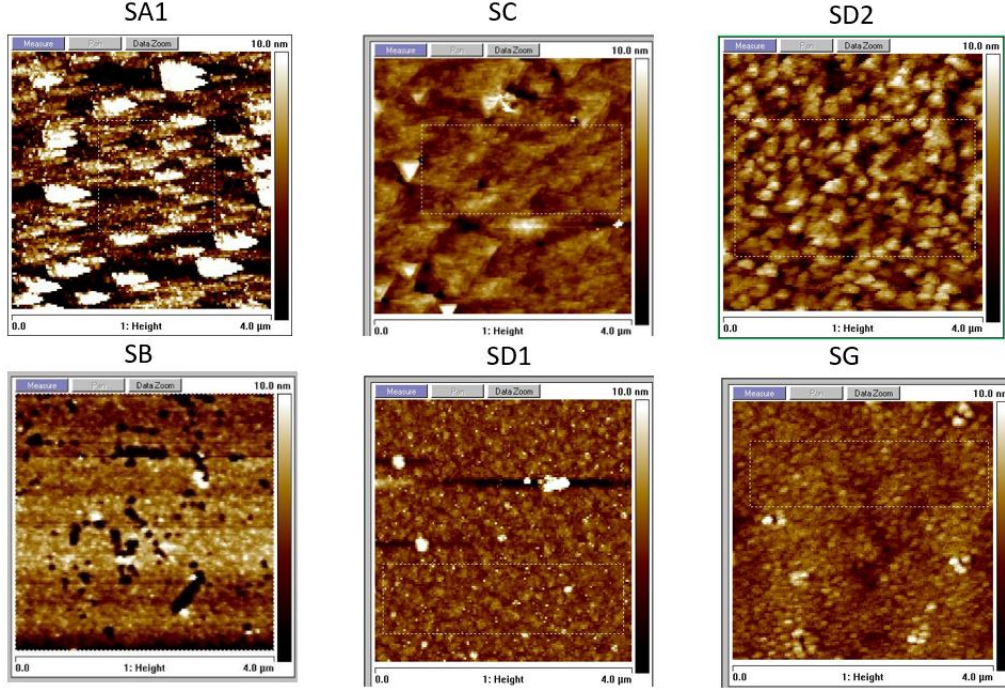


Figure 3.2. Surface roughness of $EuSe$ on different substrates: Atomic force microscopy (AFM) images of different samples.

$Se : Eu \approx 4 - 20$. Under these conditions the growth rate of $EuSe$ ($\approx 1 - 2nm/mins$) is controlled by the Eu flux. Various substrate treatments are carried out prior to the deposition of $EuSe$. The BaF_2 and sapphire substrate are annealed in-situ at $650 - 700^\circ C$ for at least 1 hour for thermal cleaning.

We found that direct growth of $EuSe$ on BaF_2 (SB) is quasi-two dimensional and yields a blurred and spotty RHEED pattern (as seen in Figure 3.3a) and rough surface. The introduction of a $Pb_{1-x}Eu_xSe$ ($x > 0.42$) buffer layer restores epitaxial 2D growth (SC), as indicated by the streaky RHEED pattern in 3.3b. Two types of $Pb_{1-x}Eu_xSe$ buffers are used in this work, a multi-layer $PbEuSe$ graded buffers and $PbSe/EuSe$ short-period superlattice (SL). It is found that the SL results in improved surface roughness compared to a graded buffer (0.77 nm vs. 0.98 nm). $EuSe$ film grown on $PbEuSe$ graded buffers is compressively strained.

For $GaAs$ (111)B substrates (SA) a specific Se treatment was carried out prior to the growth. First, a $GaAs$ (111)B substrate is heated to $\approx 570^\circ C$ to remove native oxide. Next,

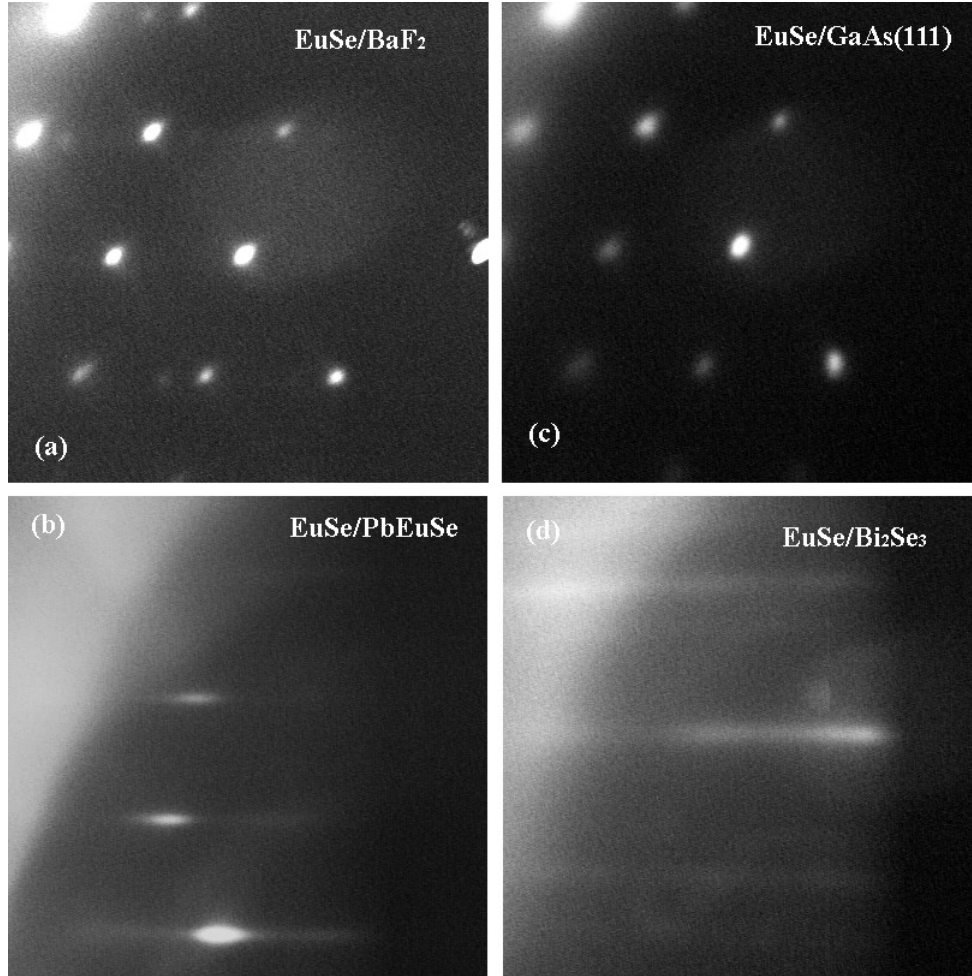


Figure 3.3. RHEED patterns of *EuSe* films grown with various crystalline orientations: *EuSe* films grown on (a) *BaF₂* (111), (b) *Pb_{1-x}Eu_xSe/BaF₂* (111) substrate, (c) *GaAs*(111)B, and (d) *Bi₂Se₃*. These pictures of RHEED patterns are courtesy of Dr.Xinyu Liu.

the substrate is annealed under Se flux ($\approx 2 \cdot 10^{-6}$ torr) at 600°C for 20 minutes to obtain streaky (1 × 1) RHEED pattern. Se passivation smooths the surface and terminates it with Se bonds. *EuSe* grown on *GaAs*(111)B substrate has two initiation processes. The direct growth often yields a 3-dimentional growth mode with a rough surface, as seen in Figure 3.3c. Alternatively, a specific atomic-layer-epitaxy (ALE) initial growth process were carried out to achieve layer-by-layer growth mode: the growth is initiated by a depositions of 6 periods of a monolayer of Se and followed by a monolayer of Eu at lower temperature (200°C). The substrate is then gradually heated to 300°C , and a nice streaky RHEED pattern (not shown,

similar to Figure 3.3d) appears prior to MBE growth of *EuSe* film. The latter process with higher *Se* : *Eu* flux ratio yields a uniform *EuSe* in (001) growth direction with a 12-fold symmetry RHEED pattern, suggesting four *EuSe* {100} planes of *EuSe* (001) surface are parallel (aligned) to three {110} plane of *GaAs*(111) surface similar to what has been recently reported for the growth of *PbSe* on *GaAs* [137] as discussed below.

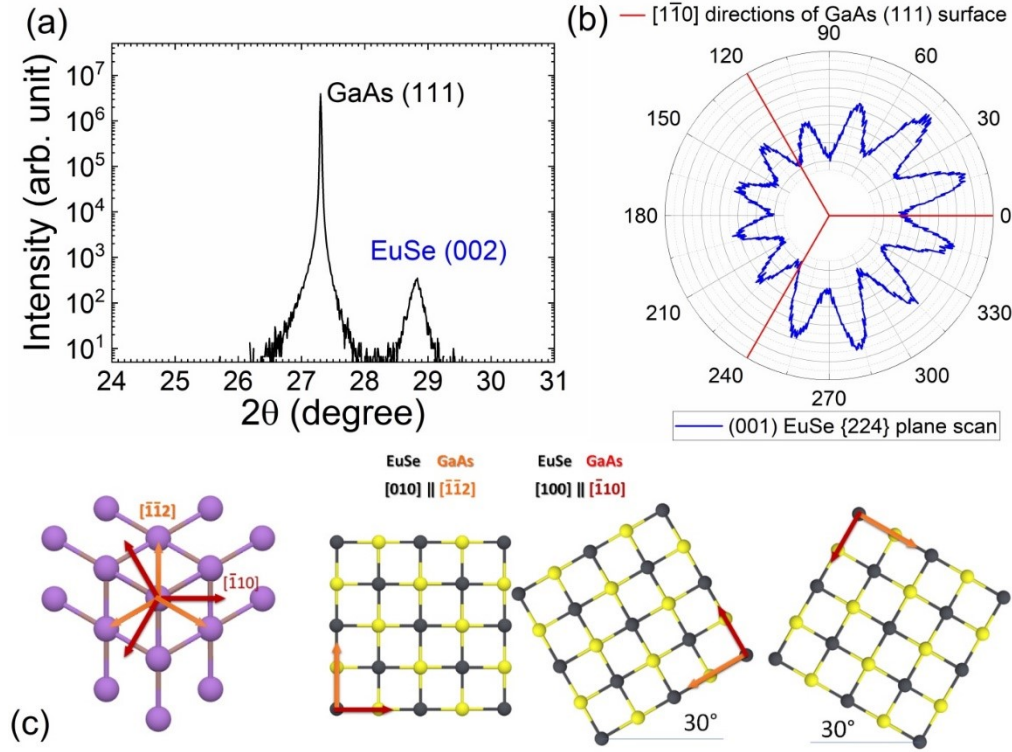


Figure 3.4. High-resolution XRD $\omega - 2\theta$ scan for (001) growth *EuSe*: (a) High-resolution XRD $\omega - 2\theta$ scan of the (111) Bragg peak of *GaAs* substrate and (002) Bragg peak of *EuSe*. (b) φ -scan of the (224) *EuSe* Bragg peak. (c) $[010] \parallel [\bar{1}\bar{1}2]$ ($[100] \parallel [\bar{1}10]$) rocksalt-zincblende in-plane alignment.

Figure 3.4a shows an XRD $\omega - 2\theta$ scan obtained for Sample SA1 grown on a *GaAs*(111)B substrate. All the $\omega - 2\theta$ scans displayed in this chapter has been performed by our collaborator Dr. Xinyu Liu at University of Notre Dame. A strong (002)*EuSe* peak is observed, indicating that a (001)-oriented *EuSe* layer is indeed obtained despite the (111) *GaAs* surface. A φ -scan is also performed about a (224) *EuSe* peak (Figure 3.4b), a 12-fold symmetric reflection pattern is visible about the *EuSe* peak. Figure 3.4c presents the alignment of *EuSe*(001) on the *GaAs*(111) surface as follows: If the $[010]$ direction of *EuSe* is aligned

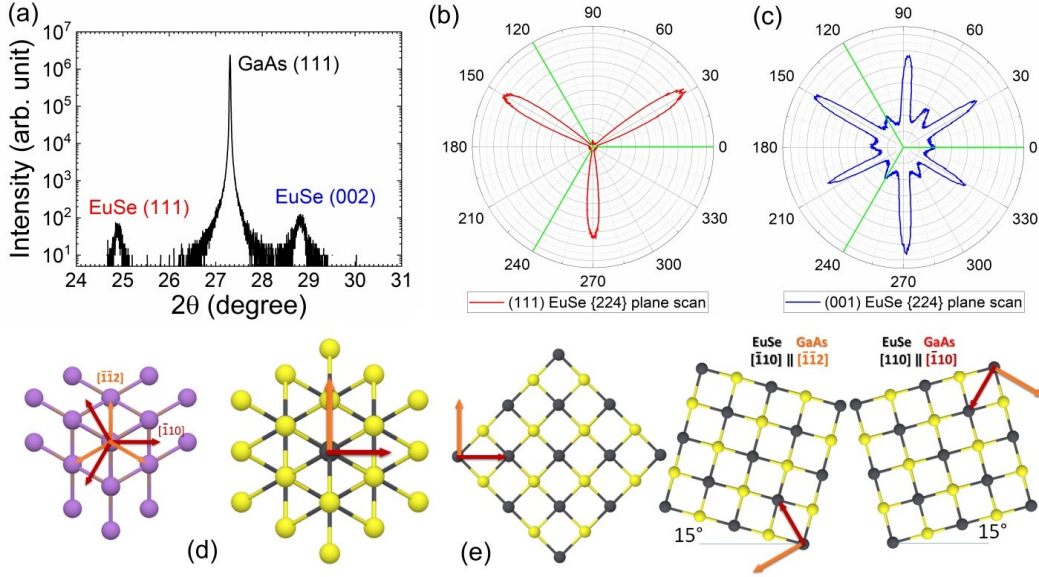


Figure 3.5. High-resolution XRD $\omega - 2\theta$ scan for (001) mixed with (111) growth *EuSe*: (a) High-resolution XRD $\omega - 2\theta$ scan of the (111) Bragg peak of GaAs substrate, and (111) and (002) Bragg peaks of *EuSe*. (b) φ -scan of the (224) *EuSe* Bragg peak with (111) growth direction. (c) φ -scan of the (224) *EuSe* Bragg peak with (001) growth direction. (d) $[\bar{1}10] \parallel [\bar{1}10]$ rocksalt-zincblende in-plane alignment for *EuSe* film with (111) growth direction. (e) $[\bar{1}10] \parallel [\bar{1}12]$ ($[100] \parallel [\bar{1}10]$) rocksalt-zincblende in-plane alignment for *EuSe* inclusion with (001) growth direction.

with the $[\bar{1}1\bar{2}]$ direction of GaAs, then a $[100]$ direction of *EuSe* is aligned with the $[\bar{1}10]$ direction of *GaAs*. There are, however, three $\langle 112 \rangle$ directions yielding 3 possible alignments shown in the Figure 3.4c. For each one of these cases there are 4 possible alignments of the rock-salt unit cell yielding 12 possible orientations. Figure 3.5a shows an XRD $\omega - 2\theta$ scan obtained for sample SA2 also grown on a *GaAs*(111)B substrate. Both (111) and (002) *EuSe* peaks are observed, indicating that a mixed (111)/(001)-oriented *EuSe* layer is obtained in this case. A φ -scan is performed about a (224) *EuSe* peak in respect to *EuSe* with (111) orientation (Figure 3.5b), a 3-fold symmetric reflection pattern is visible about such *EuSe* peak, suggesting $[\bar{1}10] \parallel [\bar{1}10]$ rocksalt-zincblende in-plane alignment for *EuSe* film with (111) growth direction (Figure 3.5d). A φ -scan is also performed about a (224) *EuSe* peak respect to *EuSe* with (001) orientation (Figure 3.5c), a 12-fold symmetric reflection pattern is observed, including 6-fold strong pattern and 6-fold weak pattern. In this case,

Figure 3.5e presents the alignment of $EuSe(001)$ inclusion on the $GaAs(111)$ surface as follows: If the $[\bar{1}10]$ direction of $EuSe$ is aligned with the $[\bar{1}\bar{1}2]$ direction of $GaAs$, then a $[110]$ direction of $EuSe$ is aligned with the $[\bar{1}10]$ direction of $GaAs$. Three $\langle 112 \rangle$ directions yield 3 possible alignments shown in the Figure 3.5e. For each one of these cases there are 4 possible alignments of the rock-salt unit cell yielding 12 possibilities. Due to the effect from $EuSe$ grown on (111) direction, which usually presents 6-fold $\langle 110 \rangle$ planes, the 12-fold symmetric reflection pattern evolves into a combination of 6-fold strong pattern and 6-fold weak pattern.

Moreover, $EuSe$ is grown on Bi_2Se_3 , itself grown on sapphire c-plane (sample SD1), and $GaAs(111)B$ (SD2) substrate. 15-20 nm thick Bi_2Se_3 were grown at $300^\circ C$ under Se rich condition as in ref[138], [139], followed by the $EuSe$ growth. Under Se rich condition ($Se : Eu > 10$), the RHEED pattern is blurry but streaky, suggesting a layer by layer growth mode (see Figure 3.3d). The process yields $EuSe$ in (001) growth direction with a pseudo 24-fold symmetry rotations, confirmed by the φ -scan of $\{224\}$ planes of (001) $EuSe$ (see Figure 3.4 and Figure 3.5). Lastly, a trilayer of $EuSe/Bi_2Se_3/EuSe$ is grown on $GaAs(111)B$ following the combined approach used for SA1 to grow $EuSe$ on $GaAs$ and SD2 to grow an additional Bi_2Se_3 with $EuSe$ on top.

Structurally, epi-layers are characterized by high resolution X-ray diffraction (HRXRD) using $1.5406\text{ Cu} - K_{\alpha 1}$ radiations and transmission electron microscopy (TEM), performed by our collaborators Dr. Xinyu Liu, Dr. Maksym Zhukovskiy, and Dr. Tatyana Orlova at the University of Notre Dame. Figure 3.6 and Figure 3.7 summarize the X-ray diffraction characterizations revealing growth direction and strain of $EuSe$ thin films grown on different materials. The growth of $EuSe$ on $GaAs(111)B$ (SA) has two modes: a mixed phase with both $EuSe(111)$ and $EuSe(001)$; and a single phase with $EuSe(001)$ as shown in Figure 3.6ab for two different samples. The growth direction depends on the $Se : Eu$ ratio: for $Se : Eu > 10$ a (001) growth is preferred (SA1), while for $Se : Eu \approx 4$, a (001) growth with (111) inclusions is observed (SA2), as can be seen from both XRD spectrum and TEM images.

The XRD pattern on SB grown on $BaF_2(111)$ is shown in Figure 3.6c. A (111) oriented $EuSe$ layer that is negligibly strained ($< 0.09\%$) is obtained in this case. The XRD pattern

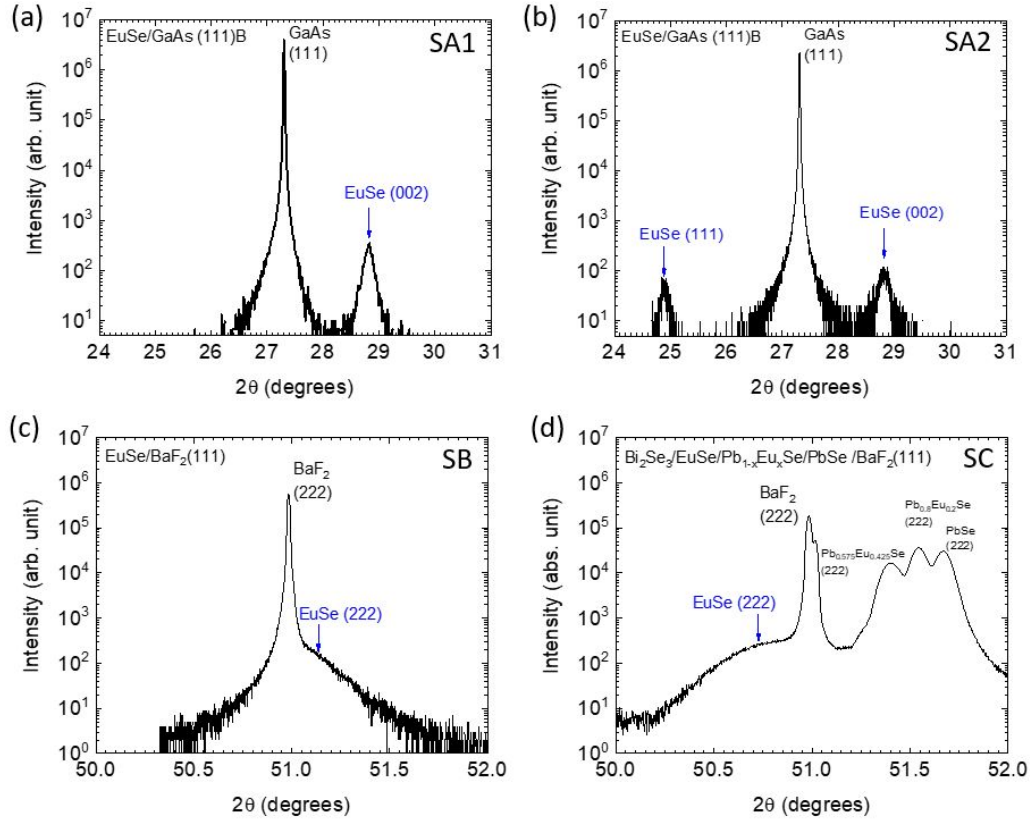


Figure 3.6. Structural characterization of *EuSe* growth on different substrates: HRXRD of *EuSe* films grown on (a)(b) *GaAs*(111)B, (c) *BaF₂*(111), (d) *Pb_{1-x}Eu_xSe*/*BaF₂*(111) substrates.

from SC grown on a *Pb_{1-x}Eu_xSe* buffer layer is shown in Figure 3.6d. This layer is also (111) oriented but slightly compressively strained in the plane and tensile strained in the (111) direction ($\approx -0.6\%$). Figure 3.7a shows the XRD patterns of *EuSe* grown on *Bi₂Se₃* (SD1 and SD2 and SF respectively). Both layers are found to be dominantly (001) oriented. However, one need to note that some (111) inclusions are observed in *EuSe* grown on *Bi₂Se₃* by TEM. A XRD $\omega-2\theta$ scan obtained for sample SD2, *EuSe* grown on a *Bi₂Se₃/GaAs*(111)B substrate is shown in Figure 3.7a. The (002) and (004) Bragg peaks of *EuSe*, and a series of {003} Bragg peaks of *Bi₂Se₃* peaks were observed in the data, suggesting *EuSe* grown along (001) direction and is fully relaxed on the c-plane of *Bi₂Se₃*(001). A φ -scan of {224} planes of (001) *EuSe* indicates a pseudo 24-fold symmetry as shown in Figure 3.7b: four *EuSe* {100} planes are dominantly parallel (aligned) to three {110} plane of *Bi₂Se₃*(001)

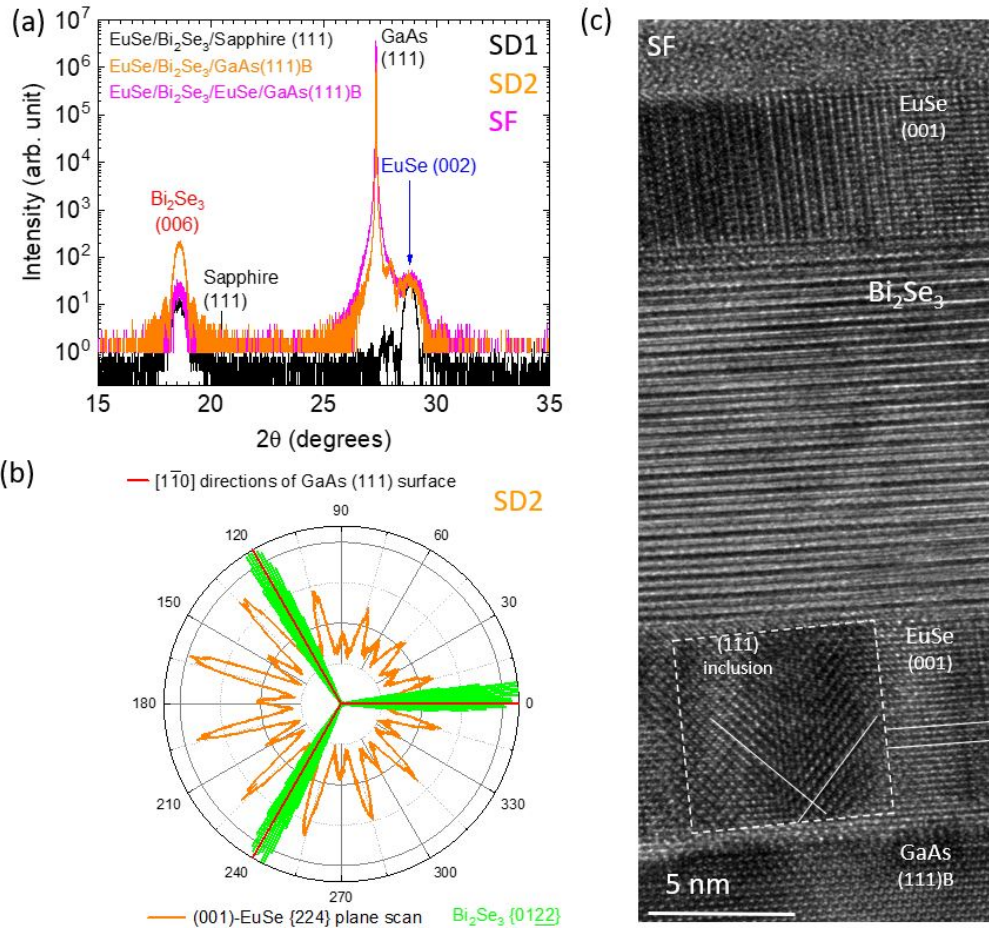


Figure 3.7. Structural characterization of *EuSe* growth on Bi_2Se_3 : (a) HRXRD of the *EuSe* film grown on $Bi_2Se_3/GaAs(111)B$ see (002) and (004) Bragg peaks of *EuSe*, and a series of Bi_2Se_3 peaks. (b) φ -scan of the (224) *EuSe* Bragg peak with (001) growth direction, and φ -scan of the {0122} Bi_2Se_3 Bragg peak. (c) High-resolution TEM image for the *EuSe*/ Bi_2Se_3 /*EuSe* epilayers grown on $GaAs(111)B$ substrate shows a predominantly [001] oriented growth of *EuSe* on $GaAs(111)B$ with some (111) inclusions.

surface, while some of four *EuSe* {110} planes are parallel (aligned) to three {110} plane of $Bi_2Se_3(001)$ surface. Sample SF is also characterized by XRD and yields a (001)-oriented *EuSe*, however a TEM image (Figure 3.7c) shown mixed (111) and (001) growths of *EuSe* on $GaAs(111)B$. Overall, XRD measurements clearly evidence a (111) oriented growth on nearly lattice-match $BaF_2(111)$ and $Pb_{1-x}Eu_xSe(111)$, but either a mixed phase or a (001) oriented growth on $GaAs(111)B$ and the Bi_2Se_3 surface with large lattice mismatch. This

will be of interest for subsequent magnetic measurements of the properties of $EuSe$, as this control of the growth orientation enables a concurrent control of the magnetic character of the interface. The trilayer grown here achieves a way to study possible proximity effect with (001) surface of $EuSe$ and two surfaces of Bi_2Se_3 .

3.3 Magnetic properties

The magnetic characterization of $EuSe$ films were performed in a Quantum Design MPMS-3 SQUID magnetometer. All the samples were carefully cleaned with isopropanol and standard plastic translucent drinking straws were used as wafer holders. Samples were mounted in the straws such that the magnetic field was applied either in-plane (H_{\parallel}) or out-of-plane (H_{\perp}). The magnetization loops (HLs) were obtained at various fixed temperatures below and above Néel temperature. All magnetization measurements were corrected to account for the demagnetizing field of thin film (demagnetization factors $N_{\parallel} = 0$ and $N_{\perp} = 1$). In addition, a correction to the reported applied magnetic field was made to HLs measurement data and arises due to remnant magnetic field in the superconducting magnet (See Application Note 1500-011 at www.qdusa.com). The field correction on this magnetometer was measured and verified using a clean paramagnetic sample (a single crystal of gadolinium gallium garnet) which is known to have a linear and reversible magnetization curve. As a result, the real applied fields in the system should be calibrated by shifting down (up) the reported field with a few Oersted (Oe) on decreasing (increasing) field. Careful attention to this correction is especially important here due to the implications of any remnant magnetization observed in the sample. In our measurement, 25 Oe offset is applied as the field correction. All the magnetization measurements presented below were properly corrected as described above.

3.3.1 Magnetization studies of SB: $EuSe(111)$ and SD: $EuSe(001)/Bi_2Se_3$

This section first focuses on the comparison between two types of samples: SB grown on BaF_2 and SD grown on Bi_2Se_3 .

Temperature dependence of magnetic susceptibility χ for SB and SD1 is plotted in Figure 3.8a and Figure 3.8b respectively. The Néel temperature $T_N = 4.4 - 4.9\text{K}$ of strain-free *EuSe* thin films SB and SD1 is found to be close to the T_N in bulk crystals (4.6K) and in thick epitaxial films ($4.75 \pm 0.25\text{K}$) [133]. For *EuSe* (111), we also find that the in-plane $\chi_{\parallel} \rightarrow 0$ for $T \rightarrow 0$ while out-of-plane χ_{\perp} remains finite (Figure 3.8a). This confirms that magnetization at low fields is laying within the (111) growth plane, perpendicular to growth axis. For (001) growth of *EuSe*, both χ_{\parallel} and χ_{\perp} are finite at small magnetic fields when $T \rightarrow 0$, as shown by the extended dashed lines (Figure 3.8b). This is consistent with magnetic field pointing at an angle to the magnetization axis for both field directions and indicates that magnetization does not lie along the growth axis, but remains within the (111) plane. In the following we will focus on the analysis of magnetization anisotropy in (111)-oriented films since they are of interest to topological magnetic device. In these films, we can clearly separate χ_{\parallel} and χ_{\perp} .

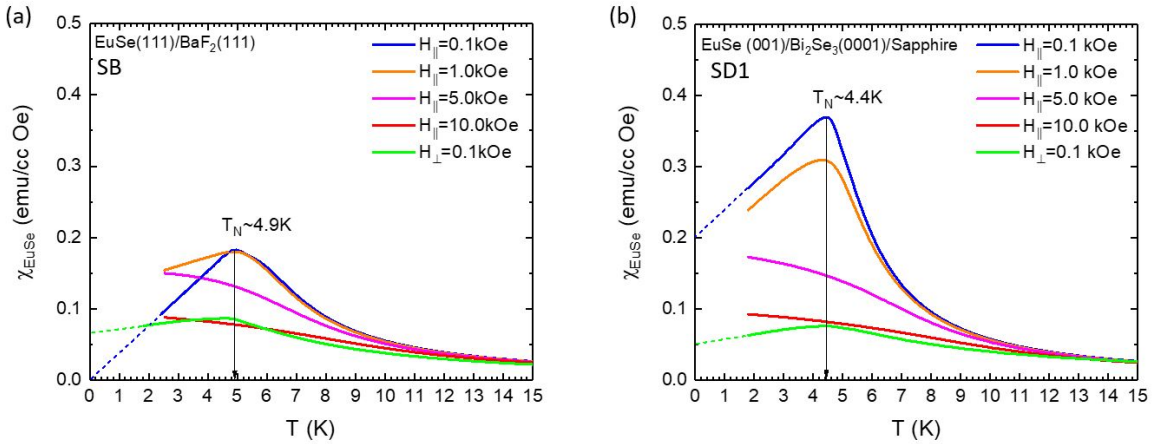


Figure 3.8. Temperature dependence of magnetic susceptibilities of *EuSe* with in-plane H_{\parallel} and out-of-plane H_{\perp} magnetic fields for (a) *EuSe*(111) and (b) *EuSe*(001) : Both samples show evolution of magnetic properties from AFM to FM when increasing applied magnetic field. The dashed lines indicate the comparison of zero temperature susceptibilities at small H_{\parallel} and H_{\perp} for both samples.

Magnetic field dependence of magnetization $M(H)$ for SB and SD1 are discussed below. Here magnetization loops normalized by fully magnetized Eu^{2+} ($6.94\mu_B$) are plotted. Magnetization loops are displayed for different temperatures and for both field applied in-plane

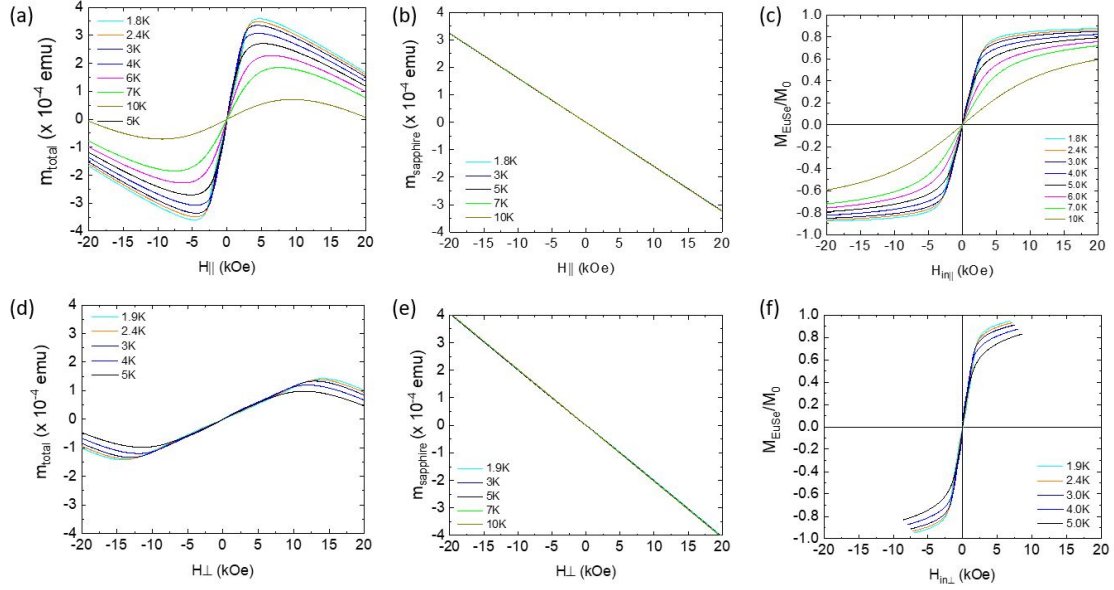


Figure 3.9. Magnetic moment per Eu^{2+} ion: Total magnetic moment of (a)(d) $EuSe$ on 2-dimensional van-der-Waals Bi_2Se_3 epilayers grown on sapphire (c-plane) substrate and (b)(e) pure sapphire substrate for (a)(b) H_{\parallel} and (d)(e) H_{\perp} ; Normalized magnetic moment per Eu^{2+} ion as a function of magnetic field at different temperatures for (c) H_{\parallel} and (f) H_{\perp} .

($H_{in\parallel}$) and out-of-plane ($H_{in\perp}$), where H_{in} is field inside the thin films and is corrected from H by considering demagnetization effect of thin film. An example of normalization of magnetic moment per Eu^{2+} ion from SD1 is explained as following. In the first place, a subtraction of substrate magnetization need to be considered for studying the magnetic contribution from a thin film only. The total magnetization (m_{total}) of sample SD1 were displayed in Figure 3.9ad. The magnetization loops of pure substrate should be subtracted to obtain magnetization of thin film $EuSe$. The magnetization loops of pure sapphire ($m_{sapphire}$) were measured after removing the top epilayers with a plastic blade, as shown in Figure 3.9be. The magnetization loops of thin film, of which magnetic moment is dominated by $EuSe$, were obtained by subtracting $m_{sapphire}$ from m_{total} . Secondly, magnetization of $EuSe$ is normalized to the magnetic moment of a Eu^{2+} ion. Magnetization of $EuSe$ in the unit of emu/cc can be converted to μ_B/Eu by using the following relationship: $emu/cc = \frac{1.0783 \cdot 10^{20} \mu_B}{4 (\lambda_{EuSe} \cdot 10^{-7})^3 Eu} = 6.41 \cdot 10^{-3} \mu_B/Eu$, where lattice constant $\lambda_{EuSe} = 0.6186$ nm is measured by XRD. For a fully polarized Eu^{2+}

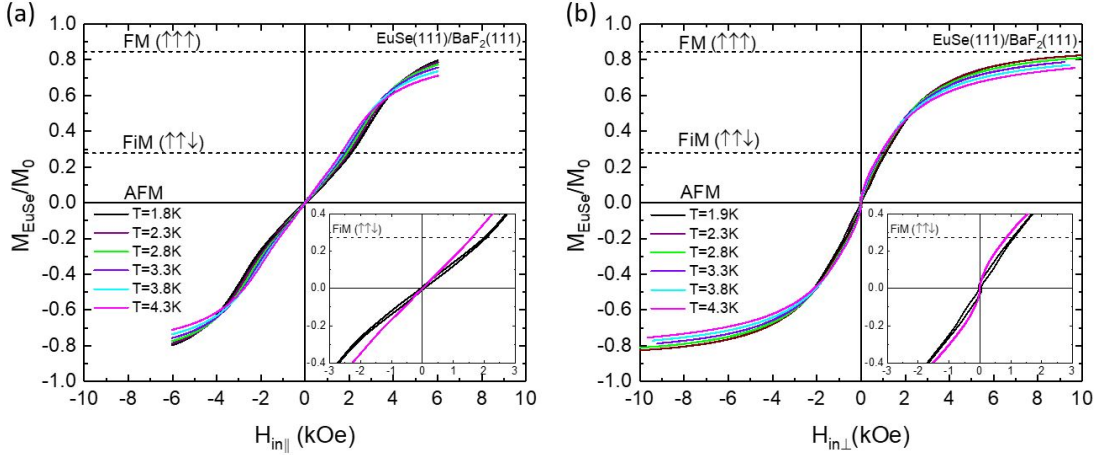


Figure 3.10. Normalized magnetization loops for SB: Normalized magnetic moment per Eu^{2+} ion as a function of magnetic field at different temperatures for (a) H_{\parallel} and (b) H_{\perp} for $EuSe$ (111) on nearly-lattice-match BaF_2 (111). The ferromagnetic (FM) and ferrimagnetic (FiM) saturation values are indicated by dashed lines. Insets: hysteresis loops are shown on an expanded scale.

ion in $EuSe$, $M_0 = 6.94\mu_B/Eu$ from DFT calculation [140]. Magnetization of $EuSe$ in the unit of emu/cc is normalized by M_0 as shown in Figure 3.9cf.

In Figure 3.10, the magnetization loops (HLs or $M(H)$) normalized by fully magnetized Eu^{2+} are plotted for sample SB. The magnetic transitions are more obviously resolved from the first derivatives of magnetization loops (differential magnetic susceptibilities (dM/dH)) as shown in Figure 3.11abde. Magnetic phase transitions that depend on field sweep direction are observed and are labeled by A^+ , A^- , B^+ and B^- . Expected FiM-FM transitions (A^+ , A^-) are observed, and an unexpected property of the AFM-FiM transitions, a hysteresis marked by B^+ and B^- . The temperature dependence of peak amplitude is similar for B^+ and B^- as shown in Figure 3.11c, indicating that the two transitions have the same origin, but arise at a different boundary. In Figure 3.11f, $EuSe$ crystal structure of (111) growth with in-plane spin rotation from the top and side views is displayed.

The corresponding in-plane phase diagram (solid symbols and color regions) of thin film $EuSe$ (111) is compared to the phase diagram (purple lines) of a bulk $EuSe$ (111) extracted from ref[133] in Figure 3.12. We first observed enhancement of field values for FM-FiM transition from our thin film $EuSe$ compared to reported bulk $EuSe$ [133], [135]. While

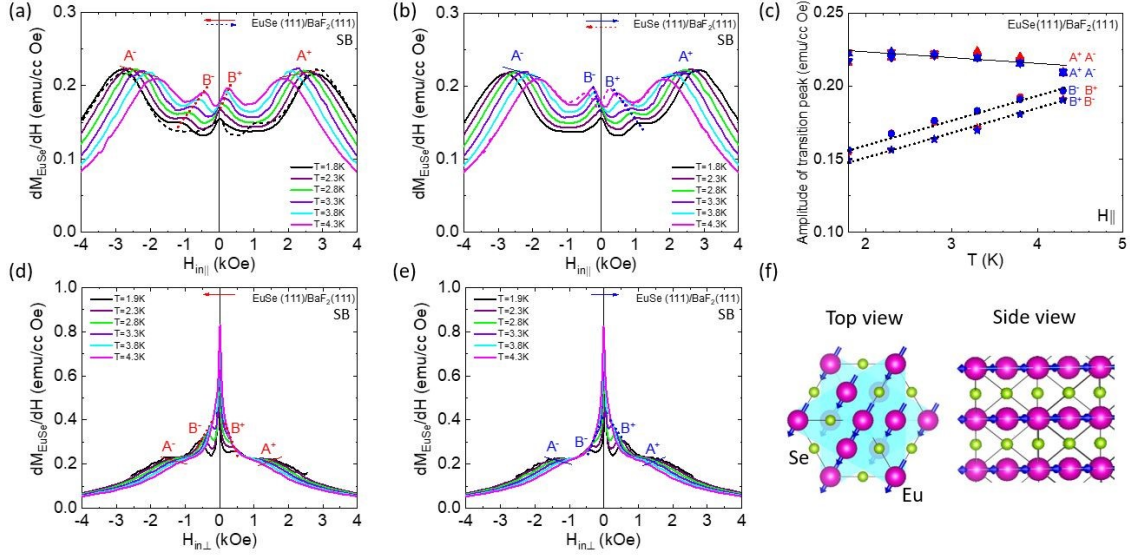


Figure 3.11. Magnetic properties of $EuSe(111)$: Differential magnetic susceptibilities (dM/dH) as a function of magnetic field with two opposite field sweep directions at different temperatures for (a)(b) in-plane $H_{||}$ and (d)(e) out-of-plane H_{\perp} : FM-FiM transitions are labeled by A^+ and A^- and guided by solid lines, AFM-FiM transitions are labeled by B^+ and B^- and guided by dotted lines, arrows indicate the field sweep direction corresponding to the dM/dH curves. (c) Amplitude of transitions as a function of temperatures for in-plane $H_{||}$. (f) $EuSe(111)$ crystal structure with magnetization plane (cyan color) and spin rotation (blue arrows).

AFM-FiM transitions are single lines in previous reports, we observed hysteresis of AFM-FiM transition boundary in our sample, which slightly depends on temperature. The observation of the hysteresis loop during AFM-FiM transition in film was reported in the early literature [141] studying the huge g-factor observed at the magnetic phase transitions in $EuSe$. We attribute the enhanced hysteresis loop observed in this work (≈ 1 kOe) to the reduced thickness of our films and presence of an interface with another material. In fact, such phase-transition dynamics are highly dependent on the film thickness and the presence of surfaces that can modify the exchange interaction, as has been shown for extensively for the AFM-FM transition that occurs near room temperature in FeRh alloys [142]–[144].

The phase diagram of $EuSe(001)$ film grown on Bi_2Se_3 is similar to those of $EuSe(111)$ films as shown in Figure 3.13. The magnetization data confirms that: (i) AFM magnetic orders occurs with a magnetic easy axis confined to the (111) planes of the NaCl-type crystal

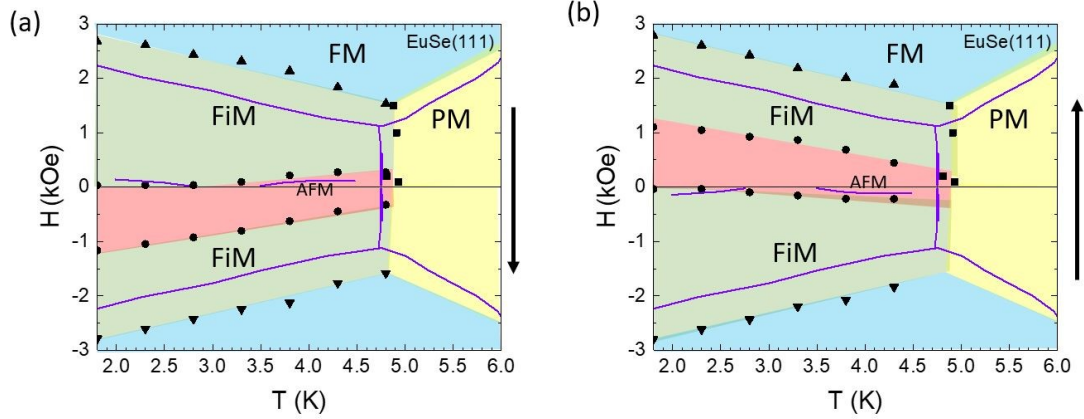


Figure 3.12. Phase diagram of SB: In-plane phase diagram of $EuSe(111)$ on nearly-lattice-match $BaF_2(111)$ for (a) field sweeping down and (b) field sweeping up. Dots and triangles are positions of A and B peaks in Figure 3.11. The red, green, blue and yellow areas indicate the AFM, FiM, FM and paramagnetic (PM) regions. Arrows indicate the field sweep directions. The purple lines display phase diagram of μm thick $EuSe(111)$ reprinted from ref [133].

structure of $EuSe$, and (ii) the hysteretic phase transition dynamics of $EuSe(001)$ and (111) films are highly dependent on the film thickness and orientation. Such strong modification of the AFM-FiM transition in thin $EuSe$ films might provide a convenient mean to control magnetic order and phase transition by tuning the film thickness, and can also be reflected in the strength of $EuSe/TI$ magnetic exchange. Also, (001) growth of $EuSe$ grown on Bi_2Se_3 or $GaAs(111)$ surfaces provides an opportunity to realize an AFM interface with TSS.

In-plane and out-of-plane magnetic phase transitions in SD1 were extracted from the differential magnetic susceptibility dM/dH as shown in Figure 3.13abde. The phase diagram of thin film $EuSe(001)$ is summarized and compared with bulk $EuSe(001)$ single crystal in Figure 3.13cf. Both in-plane and out-of-plane field direction have certain angles related to the magnetization plane (111) in $EuSe$. We observed almost identical FiM-FM transitions (A^+ , A^-) and AFM-FiM transition boundary (B^+ , B^-) in both field directions. Phase diagrams of (001) and (111) films are similar with that from bulk $EuSe$ apart from a small difference of hysteresis of the AFM-FiM transition boundary.

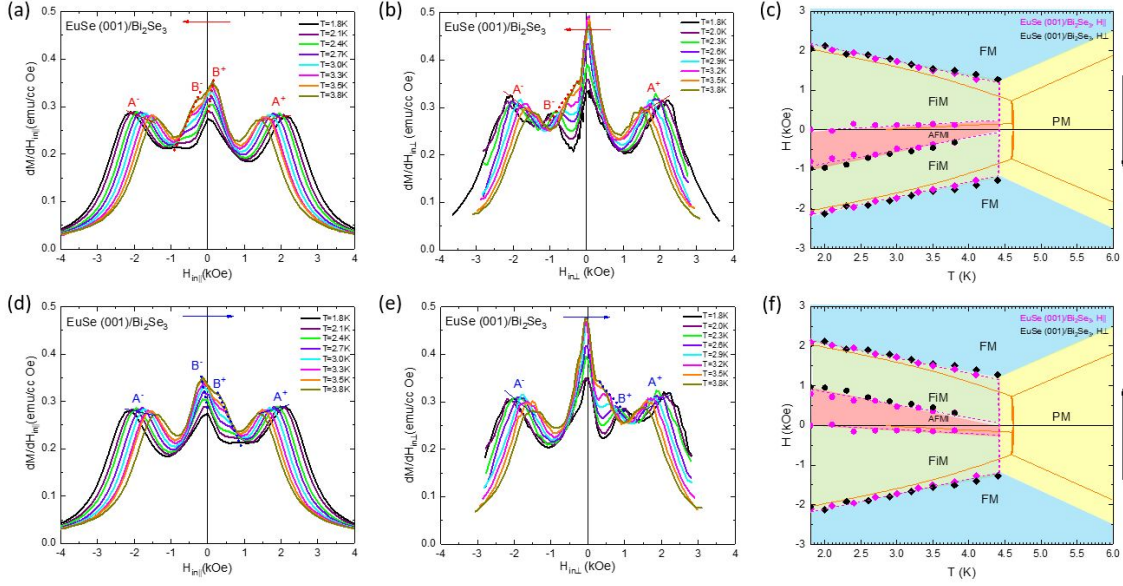


Figure 3.13. Phase diagram of SD1. In-plane (a)(d) and out-of-plane (b)(e) differential magnetic susceptibility dM/dH of $EuSe$ on 2-dimensional van-der-Waals Bi_2Se_3 epilayers grown on sapphire (c -plane) substrate as a function of magnetic field with two opposite field sweep directions at different temperatures: FM-FiM transitions are labeled by A^+ and A^- , AFM-FiM transitions are labeled by B^+ and B^- . (c)(f) Corresponding phase diagram for opposite field sweep direction: magenta and black symbols indicate H_{\parallel} and H_{\perp} . The red, green, blue and yellow areas indicate the AFM, FiM, FM and (PM) regions. Arrows indicate the field sweep directions. The orange curves display phase diagram of single crystal $EuSe$ reprinted from ref [135].

We also analyzed higher order terms in susceptibility $\chi_3 = \frac{C_3}{T-\theta_3}$, where Curie-Weiss temperature θ_3 is a measure for the biquadratic interaction strength, for sample SD1, following the analysis of ref. [145]. The biquadratic interaction is described by a molecular field which is proportional to m^3 , where $m = M/M_0$. An effective field is given by $H_{in} = \frac{1}{\chi_1} \cdot m + \frac{1}{\chi_3} \cdot m^3 + \dots$, where $\chi_1 = \frac{C_1}{T-\theta_1}$ and $\chi_3 = \frac{C_3}{T-\theta_3}$. The Arrott plot ($H_{in}/m = \frac{1}{\chi_1} + \frac{1}{\chi_3} \cdot m^2$) for paramagnetic phase is shown in Figure 3.14ab. χ_1 and χ_3 as a function of temperature are extracted from the linear fittings of Arrott plots in Figure 3.14c.

Curie-Weiss temperatures $\theta_1 = 4.15$ ($\theta_1 = 8$ in ref[145]) and $\theta_3 = 4.0$ ($\theta_3 = 3.3$ in ref[145]) are extracted from linear fitting of $1/\chi(T)$. Both $1/\chi_1$ and $1/\chi_3$ for H_{\parallel} behave linear with temperature changing and $1/\chi_3$ and does not diverge at 5.8K. This is unlike Fig.13 (Figure

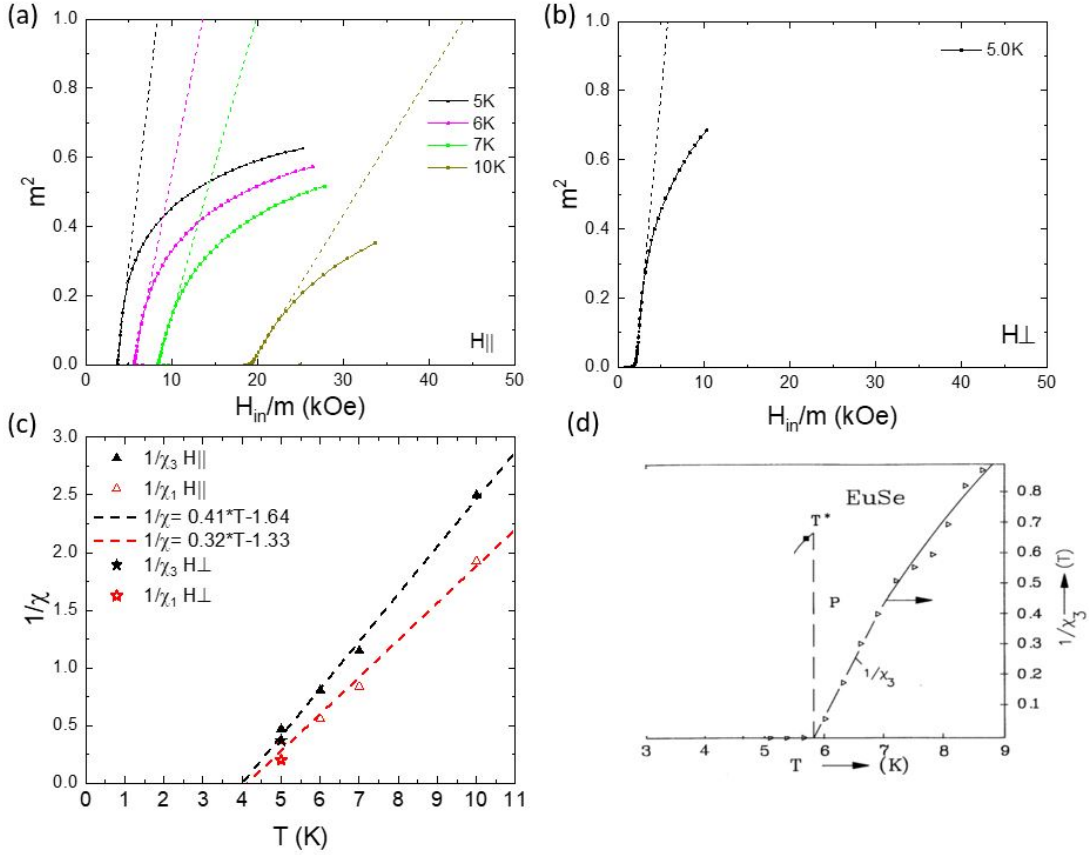


Figure 3.14. Analysis of higher order terms in susceptibility for SD1. In-plane H_{\parallel} (a) and out-of-plane H_{\perp} (b) Arrott plots of *EuSe* on 2-dimensional van-der-Waals Bi_2Se_3 epilayers grown on sapphire (c-plane) substrate at different high temperatures: dashed lines are linear fittings with slope= χ_3 and intercept= $-\chi_3/\chi_1$ at lower field ranges. (c) $1/\chi$ as a function of temperature for χ_1 and χ_3 . Dashed lines are linear fits indicating information of θ_1 and θ_3 . (d) Reciprocal cubic susceptibility $1/\chi_3$ vs. temperature for *EuSe* reprinted from ref [145]. χ_3 diverges at $T^*=5.8$ K which is 1.2K above the Néel temperature.

3.14d) showing diverging feature at 5.8K in the ref. [145]. In our thin film *EuSe*(001) we do not see 1st order phase transition (coincides with the second order in T transition when $\theta_3/\theta_1 = 0.97 \approx 1$, which is what we obtain from our experimental data).

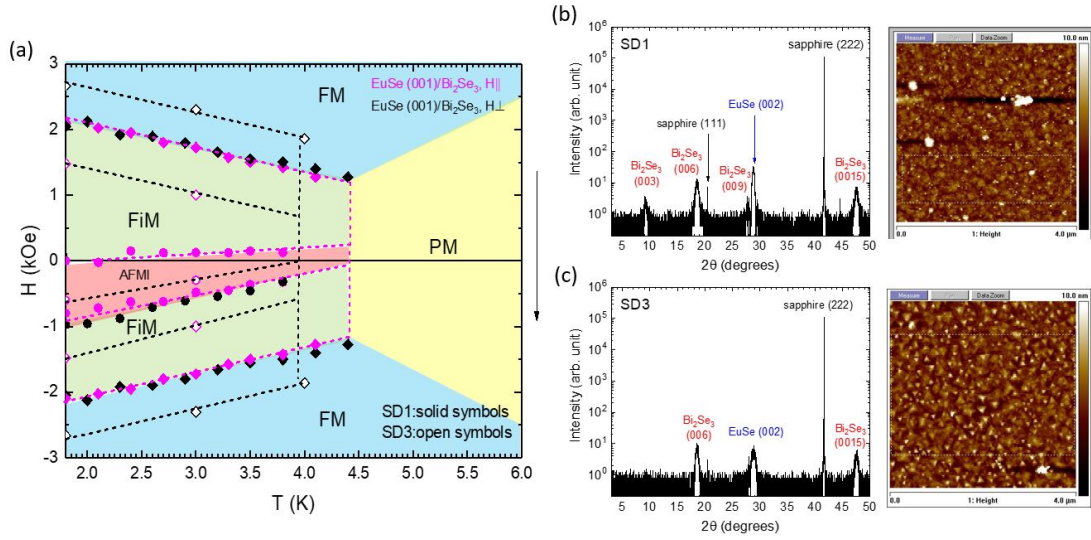


Figure 3.15. Phase diagrams and structural characterizations for SD1 and SD3: (a) Phase diagrams for SD1 (solid symbols) and SD3 (open symbols) when field in-plane (magenta symbols) and out-of-plane (black symbols). The black arrow indicates the field sweep direction. XRD scans (left panel) and AFM surface image (right panel) for (b) sample SD1 and (c) sample SD3.

3.3.2 Comparison of magnetic phase diagram and structural characterization between $\text{EuSe}(001)/\text{Bi}_2\text{Se}_3$ samples SD1 and SD3

Néel temperature reduces 15% for sample SD3 with thinner EuSe film as shown in the phase diagram (Figure 3.15a) comparing SD3 with SD1. The phase transition peaks observed from differential magnetic susceptibility for SD3 are broader and less clear than SD1 due to thinner thickness of EuSe . The saturation of total magnetization above $H > 10\text{kOe}$ for SD3 is 30% less than SD1. Furthermore, different from SD1 with almost identical field transition for both H_{\parallel} and H_{\perp} , SD3 showed anisotropic transition field, which may indicate a favor of out-of-plane canting from interfacial magnetization and this out-of-plane canting is more obvious and stronger with thinner EuSe film. The XRD data and AFM images (Figure 3.15bc) indicate that both samples have almost the same epilayer quality and surface roughness.

3.3.3 Magnetization studies of SC and SE: $Bi_2Se_3/EuSe(111)$

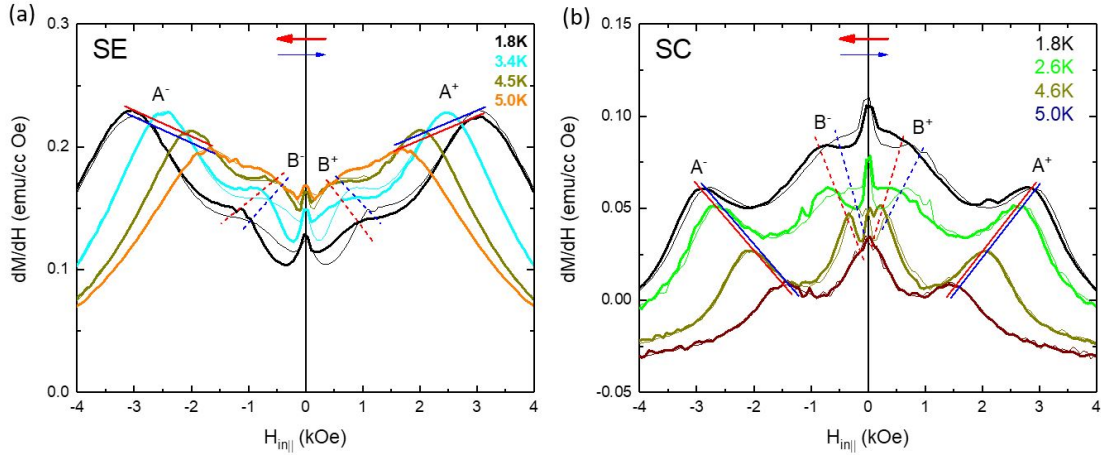


Figure 3.16. Magnetic properties of SC and SE: In-plane ($H_{||}$) differential magnetic susceptibilities (dM/dH) as a function of magnetic field with two opposite field sweep directions at different temperatures for (a) SE ($Bi_2Se_3/EuSe(111)/BaF_2(111)$) and (b) SC ($Bi_2Se_3/EuSe(111)/Pb_{1-x}Eu_xSe(111)/BaF_2(111)$): FM-FiM transitions are labeled by A^+ and A^- and guided by solid lines. AFM-FiM transitions are labeled by B^+ and B^- and guided by dotted lines. Arrows (thick and thin) indicate the corresponding field sweep direction (from $+H$ to $-H$ or from $-H$ to $+H$).

Out-of-plane proximity-induced magnetization is important in order to gap TSS. Magnetization, measured with MPMS, is dominated by the bulk of the $EuSe$ film and it is hard to disentangle interfacial response from the bulk response. However, there are some salient features in magnetization data which hint at the out-of-plane magnetization at the $EuSe/Bi_2Se_3$ interface.

In Figure 3.16 we plot in-plane differential magnetic susceptibilities (dM/dH) at different temperatures for both SE and SC with interfaces of $Bi_2Se_3/EuSe(111)$. The $EuSe$ layer of SE is almost relaxed while SC is certainly strained (+0.65%). We observed similar FM-FiM transitions labeled by A and hysteretic boundary of FiM-AFM transitions labeled by B . The corresponding phase diagrams of SC and SE are displayed and compared with SB in Figure 3.17. By adding interfaces of $Bi_2Se_3/EuSe(111)$ interface to pure bulk $EuSe$, the FM-FiM transitions are almost identical but the shape of one of the hysteretic boundaries of

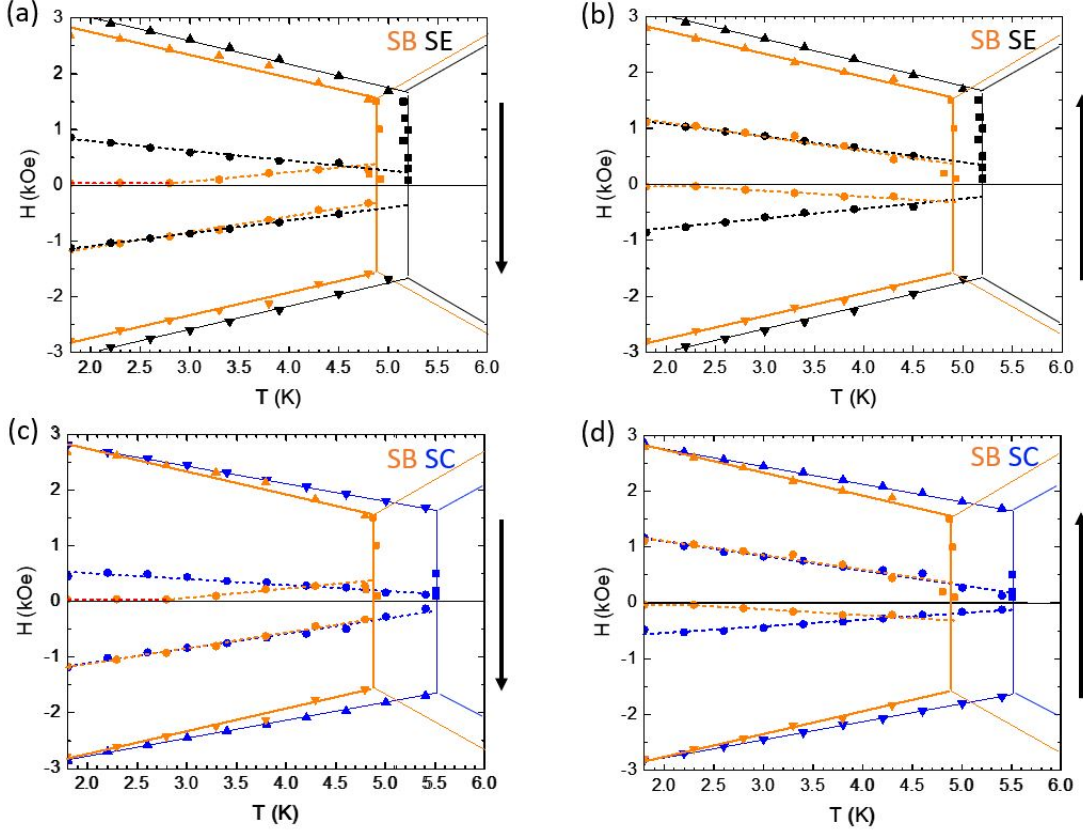


Figure 3.17. Phase diagrams of SC and SE: $Bi_2Se_3/EuSe(111)$: In-plane phase diagrams for (a)(b) SE ($Bi_2Se_3/EuSe(111)/BaF_2(111)$) and (c)(d) SC ($Bi_2Se_3/EuSe(111)/Pb_{1-x}Eu_xSe(111)/BaF_2(111)$): FM-FiM transitions are triangular symbols (positions of peak A in Figure 3.16) and guided by solid lines; AFM-FiM transitions are circular symbols (positions of peak B in Figure 3.16) and guided by dotted lines; arrows indicate the corresponding field sweep directions.

FiM-AFM changed, indicating effect from interfacial exchange interaction. Another feature of differential magnetic susceptibility to be noticed is a small bump around $H = 0$ existing from $T = 1.8K$ to $T = 5.0K$ for SC and SE but from from $T = 1.8K$ to $T = 2.8K$ for SB. We compared SB with SE (and SC) at $T = 1.8K$ and $T \approx 4.3K$ as shown in Figure 3.18. A small bump around $H = 0$ at $T \approx 4.3K$ is observed for SE (and SC) but not for SB, indicating AFM exchange coupling between Bi_2Se_3 and $EuSe$ independent of magnetic phase in bulk $EuSe$. To clarify this conclusion, we also conducted transport studies and cooperated with

Dr. Valeria Lauter for spin-polarized neutron reflectometry (PNR) experiments at Oak Ridge National Laboratory.

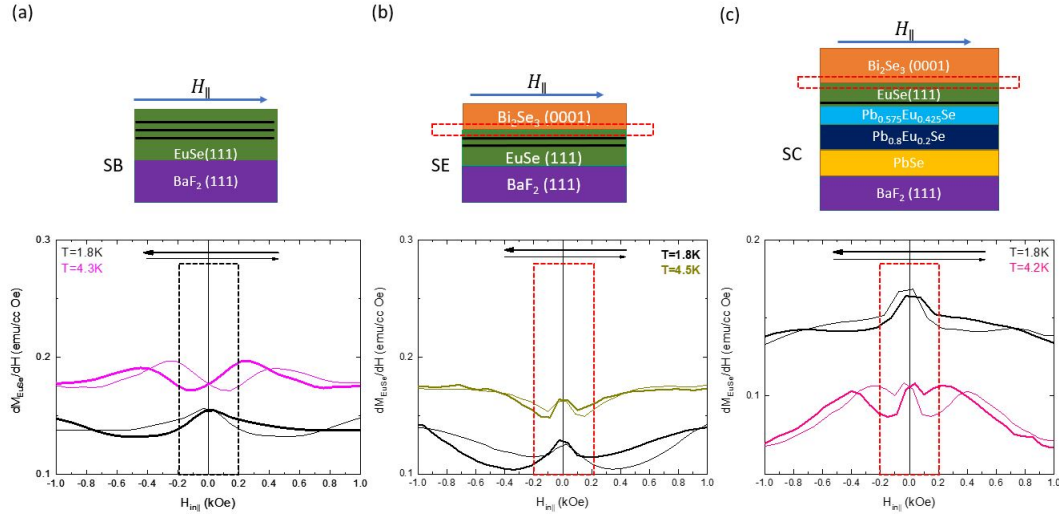


Figure 3.18. Comparison of in-plane differential magnetic susceptibilities among SB, SC and SE : In-plane differential magnetic susceptibilities as a function of small range magnetic field with two opposite field sweep directions at low temperature ($T = 1.8K$) and high temperature ($T \approx 4.3K$) for (a) SB ($EuSe(111)/BaF_2(111)$), (b) SE ($Bi_2Se_3/EuSe(111)/BaF_2(111)$), and (c) SC ($Bi_2Se_3/EuSe(111)/Pb_{1-x}Eu_xSe(111)/BaF_2(111)$) : a small peak around $H = 0$ at $T \approx 4.3K$ is observed in both SC and SE but not in SB (emphasized by dashed rectangular box). Insets: layer structures of each sample is shown. Black horizontal lines indicate (111) magnetization planes. Red dashed box outlines the interface between $EuSe(111)$ and Bi_2Se_3 . Arrow indicates in-plane field direction.

3.4 Spin-polarized neutron reflectivity (PNR) of $EuSe(001)/Bi_2Se_3/Sapphire$ samples

To explore the depth profile of magnetization in $EuSe$ films, we performed Polarized Neutron Reflectometry (PNR) [146]. PNR is particularly well suited for determining the nanostructures of magnetic thin films and multilayers. Different from other ordinary magnetometers which probe average magnetization only, PNR provides a unique way to see the vector magnetization with spatial detail under the surface of a sample. Neutrons possess a magnetic moment and can be obtained with a wavelength comparable to inter-atomic

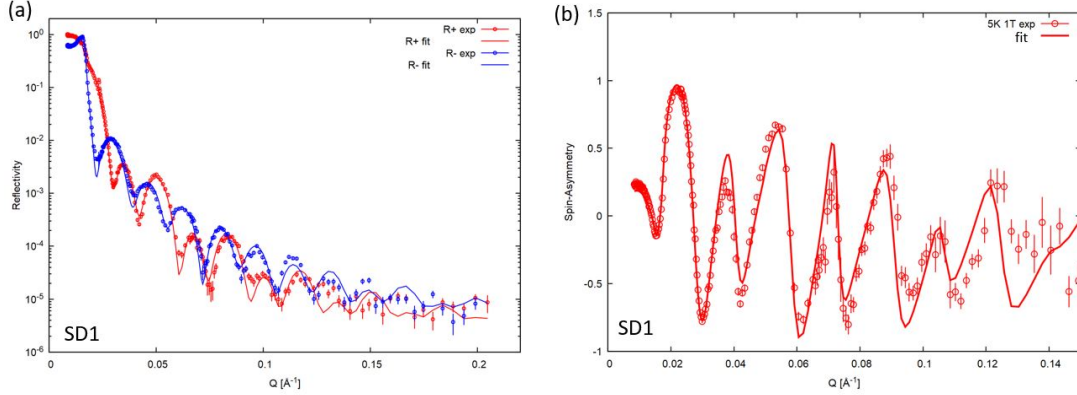


Figure 3.19. Polarized neutron reflectometry (PNR) results for SD1 : (a) Measured (symbols) and fitted (solid lines) reflectivity curves for spin-up (R^+) and spin-down (R^-) neutron spin-states (logarithmic-linear scale) as a function of momentum transfer $\vec{Q} = 4\pi\sin(\theta)/\lambda$, where θ is the incident angle and λ is the neutron wavelength. The error bars represent one standard deviation. (b) PNR spin-asymmetry (SA) ratio $SA = (R^+ - R^-)/(R^+ + R^-)$ obtained from the experimental and fitted reflectivities in (a). The error bars represent scattering one standard deviation. These PNR plots are courtesy of Dr. Valeria Lauter.

distances. Therefore, neutrons are sensitivity to atomic magnetic moments. Moreover, the specular reflection of polarized neutrons or coherent elastic scattering can be analyzed to yield the in-plane average of the vector magnetization depth profile along the surface normal. Sub-nanometer spatial resolution can be achieved by measuring the reflectivity (the ratio of reflected to incident intensities) over a sufficiently broad range of wave vector transfer \vec{Q} . The information about composition and vector magnetization depth profiles from \vec{Q} -scans can be extracted.

The depth profiles of the nuclear scattering length densities (NSLD) corresponds to the depth profile of the chemical distributions, and the magnetic scattering length densities (MSLD) represents the in-plane magnetization vector distributions. PNR measurements were carried out on $Bi_2Se_3/EuSe$ bilayers with Bi_2Se_3 thickness fixed at 20 QL and $EuSe$ (001) thickness 10 nm and 20 nm. The smoothness of sample surface is important to PNR experiments. The roughness of sample SD1 is only 0.88 nm, providing strong and clear signal of reflectivity. Combined with X-ray reflectometry (XRR) data and precise thickness

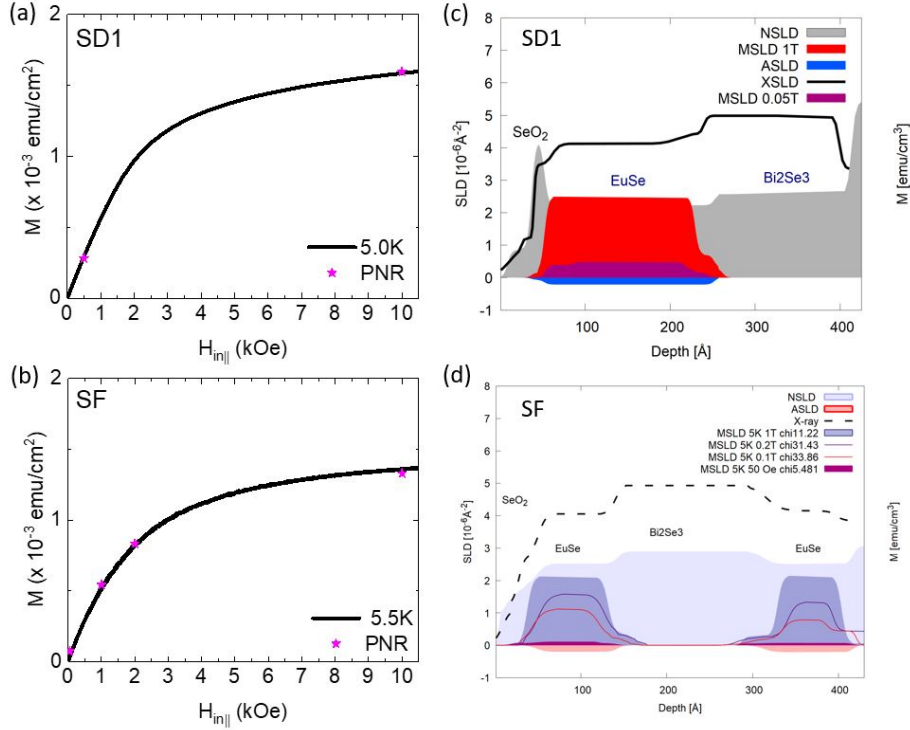


Figure 3.20. PNR and SQUID measurements. Comparison of magnetization (in the unit of emu/cm^2) between SQUID measurement (black curve) and PNR analysis (magenta stars) for (a) SD1 and (b) SF. (c) PNR nuclear (NSLD, in grey), magnetic (MSLD, in red) and absorption (ASLD, in blue) scattering length density (SLD) profiles, measured for SD1 at $T = 5 \text{ K}$ with an external in-plane magnetic field of 1 T or 0.05 T and presented as a function of the distance from the sample surface. The scale on the right-hand-side shows magnetization M . (d) PNR nuclear (NSLD, in light purple), magnetic (MSLD, in light navy) and absorption (ASLD, in light red) scattering length density (SLD) profiles, measured for SF at $T = 5 \text{ K}$ with an external in-plane magnetic fields of 1 T , 0.2 T , 0.1 T and 0.05 T and presented as a function of the distance from the sample surface. The scale on the right-hand-side shows magnetization M . The PNR analysis is performed by Dr. Valeria Lauter.

of layers obtained from TEM images, magnetization as a function of distance from the sample surface was extracted and is plotted in Figure 3.20b. The PNR data is confirmed by comparing integral PNR magnetization with SQUID measurements (see Figure 3.20a). We observed a reduction of in-plane component of $\text{EuSe}(001)$ at the interface and a magnetization penetration length of 2QL into Bi_2Se_3 at $T = 5 \text{ K}$ (PM phase) with an external in-plane magnetic field of 1 T . The ASLD profile in Figure 3.20a shows a sharp interface between the

EuSe and Bi_2Se_3 layers, and confirms that *Eu* atoms are not present in the Bi_2Se_3 layer. Given that the NSLD depth profile of the *EuSe* layer is uniform and no changes are detected in the structural and chemical composition in this interfacial *EuSe* layer, the reduction of magnetization in *EuSe*(001) at the interface indicates an out-of-plane component of the magnetization vector which is parallel to the momentum transfer \vec{Q} and is, thus, does not contribute to in PNR signal [147]. This out-of-plane component of the magnetization is not due to a proximity-induced FM coupling, as seen in $Bi_2Se_3/EuS(111)$ [96], since there is no FM response to the in-plane field H_{\parallel} in SQUID measurements.

3.5 Transport

3.5.1 Characterization of Bi_2Se_3 thin film from samples SD1 and SD3

We fabricated a Hall bar device with length of $\sim 500\mu m$ and width of $\sim 50\mu m$. The Hall bar shape was obtained by using PMMA as a protecting mask and ion milling for mesa etching. Normal Ohmic contacts Ti/Au were thermally evaporated and they are seen as the bright yellow squares in Figure 3.21a. Insulating *EuSe* was removed by ion milling before contact deposition. Conduction is dominated by the bulk of Bi_2Se_3 , and we expect effects due to gapping of TSS and possible formation of conducting domain walls in multi-domain device to be a minor contribution to the bulk conductivity. Resistivity and Hall measurements were performed on a 8T He3 system or cryogen-free (CF) dilution refrigerator system using standard lock-in technique at 17.7 Hz in 4-terminal probe.

Table 3.2. List of density and mobility of 20nm thick Bi_2Se_3 thin film.

Sample	Temperature (K)	Density $n_{2D}(\times 10^{12}cm^{-2})$	Mobility $\mu_{2D}(cm^2/Vs)$
SD1	5	8.6	446
SD1	0.05	7.4	525
SD3	~ 5	10.2	~ 680
SD3	0.25	10.1	645

Electron density and mobility of Bi_2Se_3 for samples SD1 and SD3 are summarized in Table 3.2.

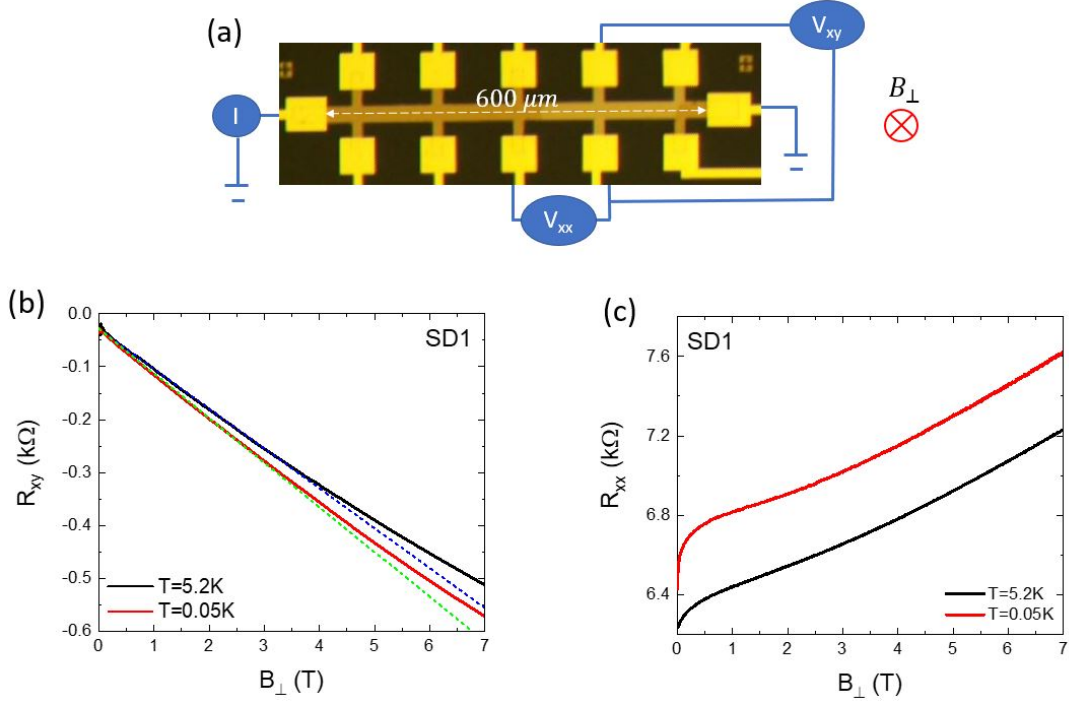


Figure 3.21. Transport characterization of Bi_2Se_3 for SD1: (a) A device picture with schematic diagram of transport measurement. The sample area is the Hall bar with length of $\sim 500\mu m$ and width of $\sim 50\mu m$. The bright yellow squares are Ti/Au normal contacts. A 10nA ac current is applied and ac voltage is measured between two contacts. (b) Hall resistance R_{xy} as a function of magnetic field at $T=0.05K$ and $T=5.0K$. Dashed line is linear fitting at low magnetic field for each temperature. (c) Longitude resistance R_{xx} as a function of magnetic field at $T=0.05K$ and $T=5.0K$.

The 2D weak anti-localization (WAL) correction to the magneto-conductivity at small magnetic field is described by the HLN formula[148].

$$\Delta\sigma(B) = \sigma(B) - \sigma(0) = -\frac{\alpha e^2}{\pi h} \cdot \left(\Phi\left(\frac{1}{2} + \frac{B_\phi}{B}\right) - \ln\left(\frac{B_\phi}{B}\right) \right) \quad (3.1)$$

where α is a constant or channel number of surface state [149], [150], Φ is the digamma function, and $B_\phi = \frac{\hbar}{4el_\phi^2}$ is a characteristic field defined by the dephasing length l_ϕ . $\alpha = 0.5$ is expected for one single surface state of a TI or a conventional 2-dimensional system with strong spin-orbit scattering [149], [150]. Typical experimental values of α can vary from 0.1 to 1, depending on the position of Fermi level and sample thickness in Bi_2Se_3

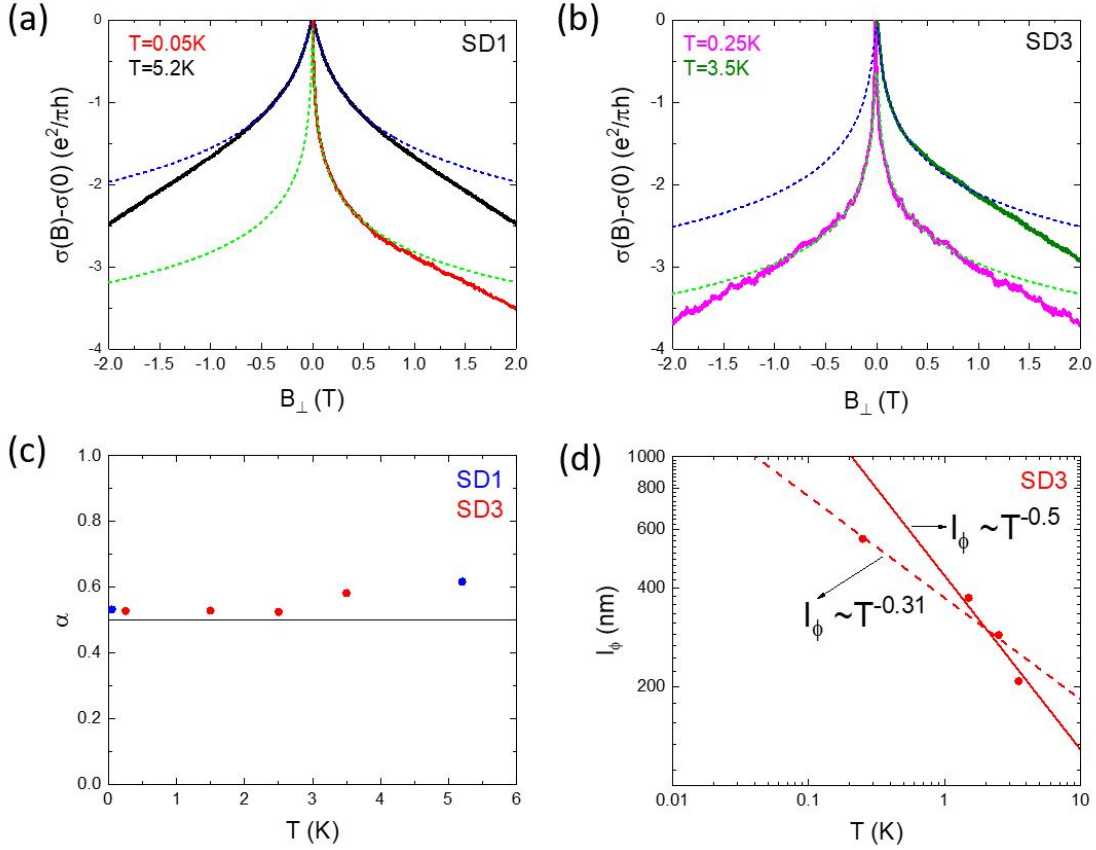


Figure 3.22. WAL of Bi_2Se_3 for SD1 and SD3: Magneto-conductivity in units of e^2/h versus perpendicular magnetic field at various temperatures for (a) SD1 and (b) SD3. Dashed curve is HLN fitting at low magnetic field for each temperature. Temperature dependence of (c) α and (d) dephasing length l_{ϕ} for SD3. The dashed and solid lines in (d) are power fittings.

[149]–[153]. $\alpha < 1$ is usually interpreted as an indication of surface-bulk coupling [150], [154]. HLN fitting can well describe the WAL behavior of Bi_2Se_3 up to $B = 0.5T$ in our samples. α in our samples is slightly larger than 0.5 and increases to 0.62 from $T = 0.05\text{K}$ to $T = 5.2\text{K}$. This may indicate more conducting channels at higher T . We extract temperature dependence of dephasing length $l_{\phi} \sim T^{-0.31}$ for the temperature range 0.25K–5K (see Figure 3.22d). Theoretically, l_{ϕ} is proportional to $T^{-1/2}$ for the two-dimensional and $T^{-1/3}$ for one dimensional systems when electron-electron interaction is the dominant dephasing source [155]. Our system is two-dimensional and at $T > 1\text{K}$, $T^{-1/2}$ well describes l_{ϕ} temperature dependence. The deviation of lower temperature ($T < 1\text{K}$) may due to a saturation of the

dephasing time at very low temperatures. In mesoscopic systems at very low temperatures, a "saturation" of the electron dephasing rate, which is independent of temperature, is often observed [156]–[158]. Many sources can result in the dephasing "saturation" such as the effect of electron-electron interaction in a disordered metal [159], [160], hot-electron effects [161], [162], electromagnetic noise [155], [163], non-equilibrium effects [164], and magnetic spin-spin scattering [165]–[167]. The microscopic origins for the widely observed "saturation" behavior remain undetermined [168]. For pure Bi_2Se_3 film, $l_\phi \sim T^{-0.47}$ was reported by our growth collaborators.

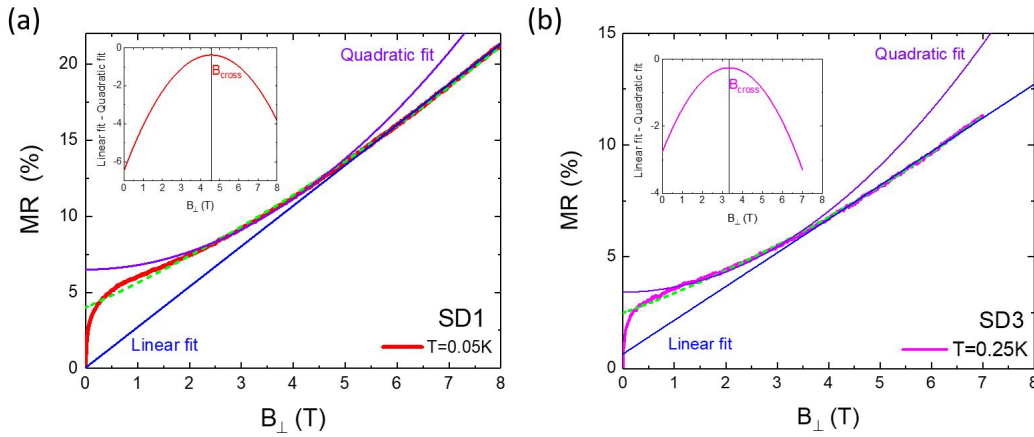


Figure 3.23. The field dependence (B_\perp) magneto-resistance (MR) at certain low temperature for (a) SD1 and (b) SD3: Dashed curve is the corresponding fitting function with a combination of quadratic function and linear function. The low field data is fitted with quadratic function while the high field data is fitted with the linear function to demonstrate their respective field dependence. The field variation of the difference of linear and quadratic function is plotted in the inset.

Figure 3.23 displays magneto-resistance $MR = (R_{xx}(B_\perp) - R_{xx}(0))/R_{xx}(0)$ as a function of B_\perp up to 8T at low temperature for SD1 and SD3. MR shows a quadratic field dependence at low fields which crosses over to a linear dependence at high magnetic fields. A parabolic function ($MR = a + b \cdot B_\perp + c \cdot B_\perp^2$ guided by the dashed curve in Figure 3.23) can well describe our MR data. A number of papers reported linear MR for pure Bi_2Se_3 with different growth methods [169]–[173]. This linear MR can arise from either quantum [174] or classical effects [175], [176]. For materials possessing a gapless linear energy dispersion in ultra quantum

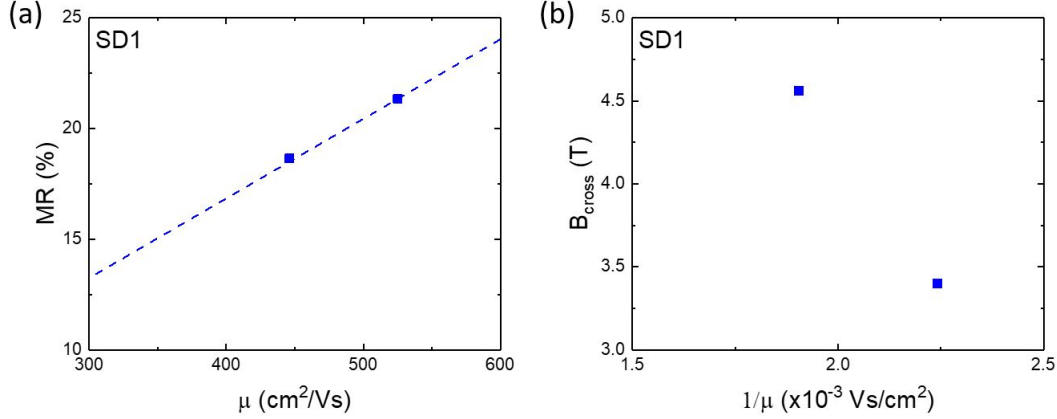


Figure 3.24. Cross field B_{cross} for SD1: (a) Magneto-resistance (MR at 8T) as a function of mobility μ . The straight dashed line represents the linear fit to data. (b) Cross field B_{cross} as a function of inverse of mobility μ^{-1} . B_{cross} is not proportional to μ^{-1} .

limit, only the first Landau level is filled and high-field linear MR can be explained by a quantum effects [177], [178]. In our system, the onset of linear MR is at $\sim 4T$. At this field the Fermi energy E_F lies far from the first Landau level and, hence, the high-field linear MR in our sample is not due to quantum limit. The other mechanisms for the existence of linear MR are classical and are associated with strong inhomogeneous distribution of carrier concentration and mobility in a strong disorder limit [175], [176]. At high fields, $\text{MR} \propto \mu$ for $\Delta\mu/\mu < 1$ and $\text{MR} \propto \Delta\mu$ for $\Delta\mu/\mu > 1$. The crossover field B_{cross} for quadratic to linear MR is $\propto \mu^{-1}$ for $\Delta\mu/\mu < 1$ and $\propto \Delta\mu^{-1}$ for $\Delta\mu/\mu > 1$. Here, μ is an average mobility and $\Delta\mu$ is the width of mobility disorder, and B_{cross} is determined as the field at which the absolute value of the difference between these linear and quadratic functions is minimum (See the insets in Figure 3.23). In Figure 3.24 for sample SD1, our MR at $B = 8T$ shows certain linear dependence ($\text{MR} \propto \mu$) but our B_{cross} is not proportional to μ^{-1} , which contradicts the inhomogeneity mechanism with $B_{\text{cross}} \sim \mu^{-1}$. B_{cross} extracted from SD3 is also not proportional to μ^{-1} . Therefore, the linear MR in our samples may not result from the distortion in current path due to inhomogeneity of electron density and mobility. Can linear MR be due to multi-channel conduction ($2 \times \text{TSS} + \text{bulk}$)? The physics of linear MR in our system is yet to be understood.

3.5.2 Magneto-resistance of $EuSe(001)/Bi_2Se_3$ without hysteresis in small field range below 300mT for both B_{\perp} and B_{\parallel}

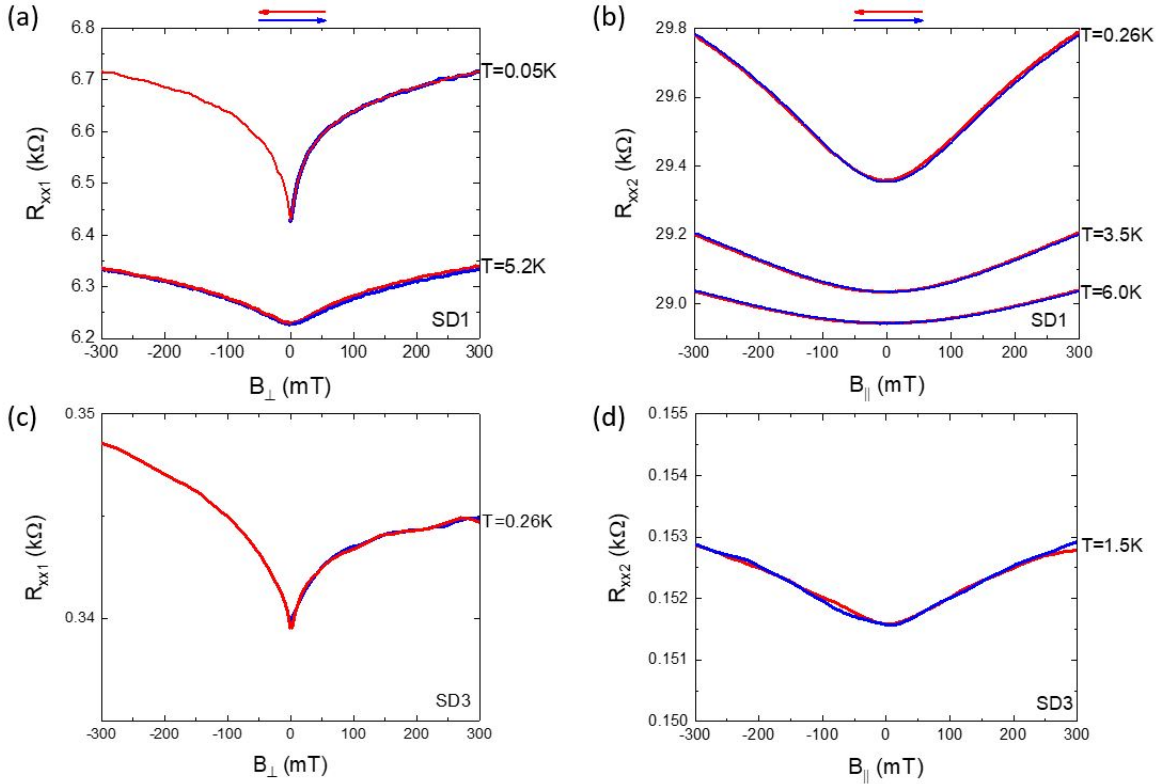


Figure 3.25. Longitude resistance below 300mT for SD1 and SD3: (a) Longitude resistance as a function of B_{\perp} or B_{\parallel} with opposite field sweep direction for (a)(b) SD1 and (c)(d) SD3 at different temperatures: resistance curves for SD1 (or SD3) displayed here are from Hall bar (or circular shaped) devices. The Ohmic contacts for all the devices here is Ti/Au. Arrows indicate field sweep directions.

According to the magnetic phase diagram, the bulk of $EuSe$ is fully polarized above 300mT and $T < 4.5K$. We focus on the magnetic range below 300mT since the bulk will be in various magnetic states (FM, FiM, AFM) depending on temperature and we are able to study any possible interfacial exchange which may relate to bulk magnetic phases. Figure 3.25 show in-plane and out-of-plane magneto-resistance changing with magnetic field below 300mT for a Hall bar and circular shaped devices from $T=0.05K$ to $T=6.0K$. Here we only show typical transport data for both samples. The noise level is below 1×10^{-4} of the signal. The magneto-resistance smoothly changes with magnetic field, indicating a typical behavior

of WAL from the bulk of Bi_2Se_3 film. We did not observe any hysteresis, which indicates an absence of FM coupling at a $EuSe/Bi_2Se_3$ interface in contrast to EuS/Bi_2Se_3 [127]. Our transport results, combined with the suppression of in-plane polarization near the interface detected by PNR, indicate that the interfacial coupling between $EuSe$ and Bi_2Se_3 is AFM independent of magnetic states of the bulk.

3.5.3 Modulation of magneto-conductance of $EuSe(001)/Bi_2Se_3$

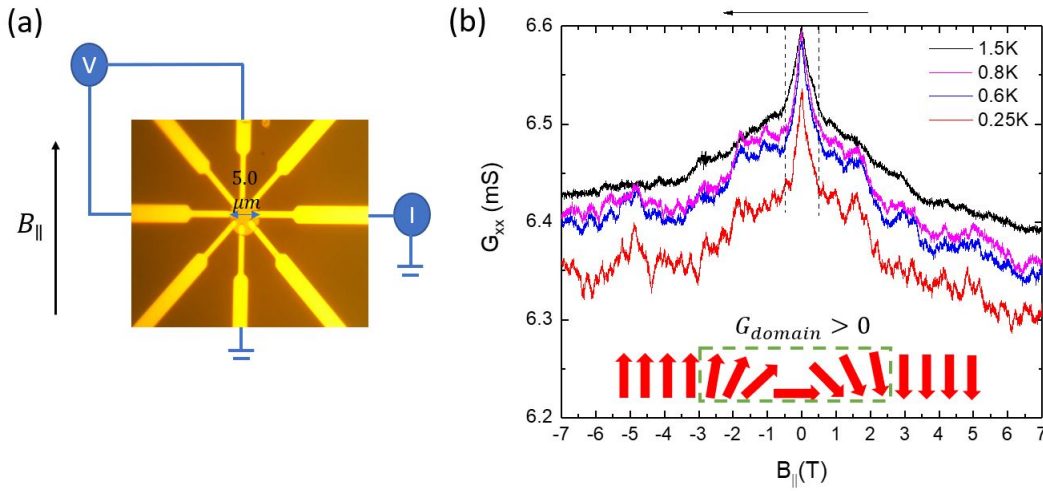


Figure 3.26. Multiple domains in a macroscopic sample SD1 : (a) A device picture with schematic diagram of transport measurement. The sample area is the circular shape in the center with a diameter of $5\mu m$. The yellow strips are Ti/Au normal contacts. A 10nA ac current is applied and ac voltage is measured between two contacts. (b) Longitude conductance G_{xx} as a function for in-plane magnetic field ($B_{||}$) at different temperatures from $T=0.26K$ to $T=1.5K$. The inset is a schematic diagram showing conduction change when conducting domains are formed.

At high magnetic fields larger than $0.5T$ we observed modulation of longitudinal conductance with no hysteresis as shown in Figure 3.26. The total conductance can be expressed as $G^{total} = G_{TSS}^{top}(M_{\perp}) + G_{Bulk}(B) + G_{TSS}^{bottom}(B)$, where G_{TSS}^{top} (or G_{TSS}^{bottom}) is conductance from top surface state (or bottom surface state), and G_{Bulk} is conductance of bulk Bi_2Se_3 . Both G_{Bulk} and G_{TSS}^{bottom} are expected to change smoothly with magnetic field. AFM exchange coupling may exist at the interface, as discussed above, and lead to a partial gapping of

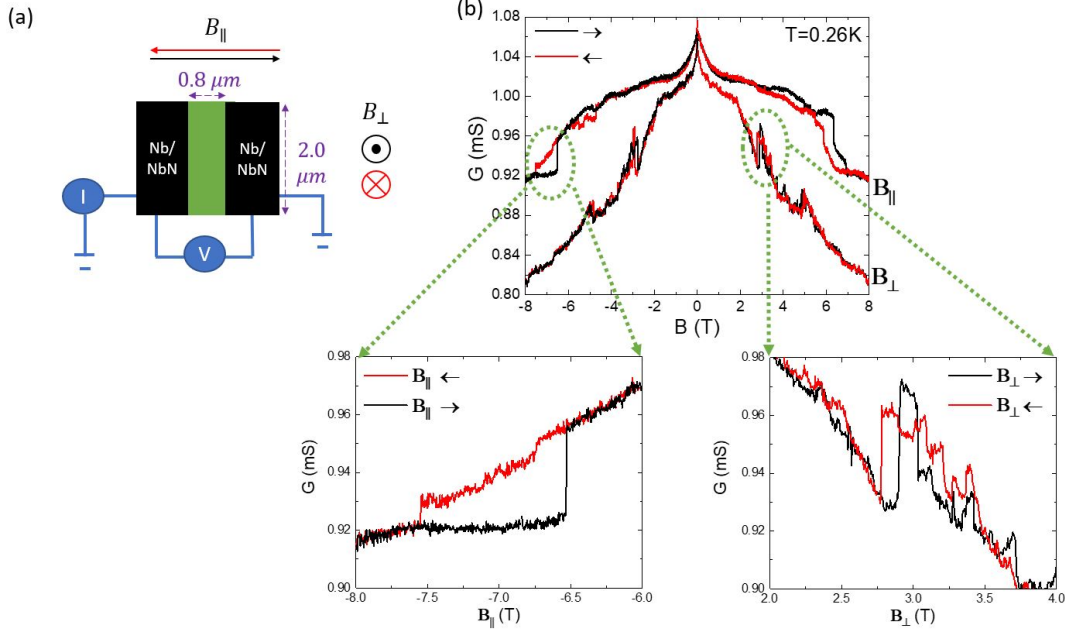


Figure 3.27. Single domain in a microscopic sample SD3 : (a) A schematic diagram of transport measurement. The green area is sample area and the black area is Nb/NbN (10nm/15nm) superconducting contacts. A 10nA ac current is applied and ac voltage is measured between two contacts. (b) Top: Conductance G as a function for in-plane ($B_{||}$) and out-of-plane (B_{\perp}) magnetic fields at $T=0.26\text{K}$. Bottom: Zoom in of the range when sharp change of conductance with hysteresis was observed for each field direction.

the top TSS. Formation of magnetic domains within the exchange layer with $T_N < T_N^{bulk}$ leads to the formation of domain walls which are expected to have conductance higher than the gapped TSS. Thus, field-induced rearrangement of out-of-plane AFM domains at the interface is expected to result in the change of the G_{TSS}^{top} and fluctuations in $G^{total} \ll G_{TSS}^{top}$, see schematic inset in Figure 3.26. For $T=0.26\text{K}$, fluctuations $\Delta G_{xx}/G_{xx}(B=0\text{T})$ can be as high as 2%.

We observed sharp change of conductance at certain magnetic fields in a microscopic sample (Figure 3.27a). We use superconducting contacts Nb/NbN with critical temperature of 8K, but differential resistance does not show any signatures of Andreev reflection, and we conclude that in this sample Nb/NbN can be regarded as an Ohmic contact. Also, any superconductivity-related change of resistance is expected to reduce conductance G at high temperature or magnetic field, while experimentally we observe both reduction and

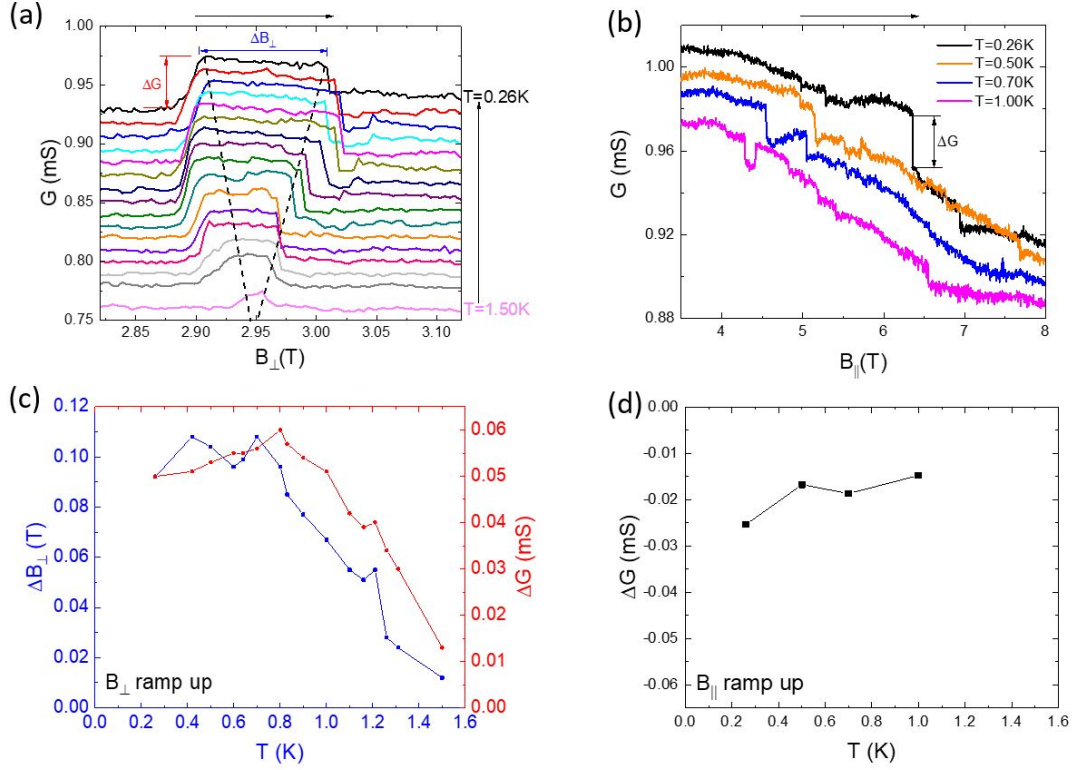


Figure 3.28. Temperature dependence of single domain in a microscopic sample SD3 : Conductance as a function of magnetic field at different temperatures for (a) B_{\perp} and (b) B_{\parallel} with field ramp up. Curves have an offset of 0.01 between each other. Sharp change of conductance (ΔG) was observed in both field directions. Conductance was increased for B_{\perp} while decreased for B_{\parallel} at the initial sharp changing point. Corresponding temperature dependence of sharp change of conductance ΔG for (c) B_{\perp} and (d) B_{\parallel} . Domain is more conducting for lower temperature.

enhancement of G (see Figure 3.27b and Figure 3.28ac). In that case, the sharp modulation of conductance for B_{\perp} is not assigned to superconductivity-related physics but reconfiguration of a single magnetic domain.

3.6 Conclusions

In summary, we have studied structural and magnetic properties of $EuSe$ thin epilayers grown on different substrates and buffer layers. On BaF_2 (111), $EuSe$ growth in (111) direction in a quasi-2D growth mode which results in rough surface. Introduction of $Pb_{1-x}Eu_xSe$

buffer layers improves surface morphology. However, $Pb_{1-x}Eu_xSe$ with $x < 0.1$ is conducting, which reduces its utility for TI exchange biasing. $EuSe$ grows in (001) direction on both $GaAs(111)B$ and Bi_2Se_3 substrates with good morphology. The magnetic phase diagram for thin films has AFM, FiM and FM phases similar to bulk crystals. Field value for the FiM-FM transitions is slightly enhanced compared to the bulk, while AFM-FiM transition is highly hysteretic and has T-dependence different from bulk crystals.

In-plane magnetization measured by PNR show a magnetization reduction at the interface between $EuSe$ and Bi_2Se_3 when bulk $EuSe$ is fully ferromagnetic. A combination of PNR and transport data rules out FM coupling at the $EuSe/Bi_2Se_3$ interface and suggests AFM coupling. The modulation of magneto-conductance above 0.5T in microscopic samples indicates formation of magnetic domains at the interface.

4. SUMMARY AND PERSPECTIVES

4.1 Transport in helical Luttinger liquids in the fractional quantum Hall regime

We investigate transport properties of hDWs in the $\nu = 2/3$ fractional QH regime. Here we study the electron transport in samples where hDWs of different length L are formed by electrostatic gating. Experimentally, in the limit $L \rightarrow 0$ approximately 12% of the edge current is diverted into the hDW, a number drastically different from the 50%, predicted by non-interacting counter-propagating chiral channels model. At high bias currents we observe an increase in the current carried by the hDW, indicating a crossover from spin-non-conserving to spin-conserving transport. Inclusion of spin non-conserving tunneling process reconciles theory with experiment.

The Ohmic contact may not be good enough in the qC geometry since we already observed the loss of contact when the magnetic field is higher than 10T. In this case, the improvement of Ohmic contact is needed in the future. In order to check contact quality in the future, it may be advantageous to redesign the device and add a few more contacts to check the current bypass problem. Mesa edges should be separated as far as possible to avoid edge cross-talk. The qC gaps can be designed similar to reference [179] focusing on the measurement of a single gap with no mixing of contributions from other gaps. The fabrication process also needs to be optimized to keep the best quality of electron gas. The residue of optical photoresist should be avoided for uniform LED illumination. Thicker oxide layer may be considered based on the observation that the quality of electron gas is better for the thicker oxide layer.

4.2 Experimental investigation of parafermion in FQHE regime

As an ongoing effort in our laboratory, superconducting proximity effect is a powerful tool to understand many-body physics. Recent theoretical proposals indicate that parafermion excitations can emerge in the fractional quantum Hall effect regime if two counter-propagating fractional chiral edge states with opposite spin polarization are brought in to close proximity in the presence of superconducting coupling [69]. So far, our group

have demonstrated the formation of helical domain wall between polarized and unpolarized $\nu = 2/3$ states. Also, in similar wafers, proximity-induced superconductivity has been reported [15]. By incorporating superconducting contacts into the helical channel, it maybe possible to form a high-order topological superconductor.

4.3 Experimental investigation of the superconducting contacts in the IQHE regime

The study of tunneling mechanism between IQHE and superconductor is also very interesting [15]. The realization of the highly transparent SC/SM interface in GaAs enables investigation of the interplay between superconductivity and states in the integer quantum Hall regime. However, it is not easy to obtain superconducting contacts with high transparency in GaAs due to a high Schottky barrier between a 2DEG and a superconductor where E_F is pinned in the middle of the gap. Ge quantum well is another promising system because of the good transparency for Al superconducting contacts [180]. Recently, quantum Hall ferromagnetic transition at $\nu = 2$ was demonstrated in Ge 2D gas [181]. But this transition only can be tuned by global control-magnetic field and cannot be locally controlled by gating. We are also working on SiGe wafers. We plan to deposit magnetic thin film to control the magnetic field in a different area of the sample. An hDW is possible to be formed in this case. We haven't successfully form good Ohmic contact using high Tc superconductors such as Nb by directly side contacting it to a SiGe quantum well while some other groups had good transparent Nb contacts. However, Al/Nb/NbN is very promising to form good transparent superconducting contacts on SiGe wafers.

4.4 Studies of possible formation of a fractional skyrmion crystal near filling factor $\nu = 2/3$

In the quantum Hall effect (QHE) regime, there is a competition between spontaneously broken symmetry states and uniform QH liquid phases. The phase transition from this exotic quantum liquids into an electron solid is anticipated at high magnetic fields. For example, the QH liquid wins for $\nu = 1/5$, while Wigner crystal (WC) wins at $\nu = 1/7$ and smaller filling factors [182], [183]. For the second Landau level (LL), there is a competition between

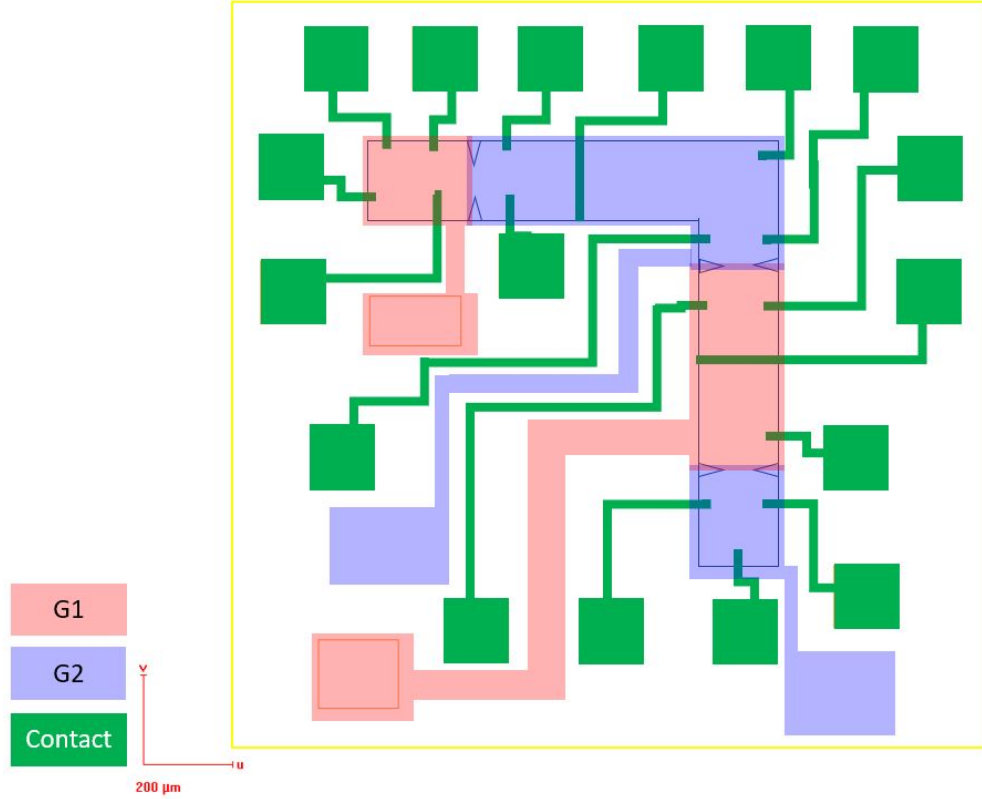


Figure 4.1. Design of future device for further studies of spin pumping: The mesa pattern is outline by black lines. Gate 1 and gate 2 are labeled by red and blue colors. Green color marks the position of Ohmic contact.

uniform quantum Hall liquid and charge density waves which break a translational symmetry [184]. For states near $\nu = 1$, a FM phase, a more exotic state of skyrmion crystal (or ordered spin texture) [185], [186] formed by skyrmions with repulsive interactions is predicted. This is an indication that skyrmion crystal can be formed near $\nu = 1/3$, which is a mirror of $\nu = 1$ for composite fermions (CFs). However, the crystalline state has not been seen in higher filling factors neither for CFs nor for electrons. Although a recent paper claimed formation of a solid at $\nu = 2/3$ in graphene [187] by using magnon as a detection method, one needs to note that high energy magnons are not a proper probe to study crystal formation because the observation of INCOHERENT magnon scattering is a characteristic of a DISORDERED media or indication of INELASTIC processes but NOT a signature of a crystal formation.

We constructed a single hDW system in $\nu = 2/3$ fractional Hall state and injected spin into the system in a controllable way. In GaAs, nuclear bath polarization can serve as a

low-energy spin detector. We observed unidirectional nuclear polarization which requires an efficient generation of low energy spin waves in the polarized state. Skyrmion crystal is expected to support low energy spin excitations. However, many questions are yet to be answered within the spin-wave picture.

In our previous device, hDWs with different lengths were not isolated from each other. Any possible spin excitation from two hDWs may interact with each other during the propagation. Also, we did not have enough contacts along the edge to study the propagation of spin waves. Our design of a new device (see Figure 4.1) will contain several isolated hDWs with different lengths. We will have contacts at both top and bottom edges to learn any possible change of potential due to the emission of spin waves. Since this type of spin excitations is at very low energy, the detailed studies of this system will help us to understand physics in FQHE, for example, to answer the question of whether there is any possible formation of a fractional skyrmion crystal near filling factor $\nu = 2/3$.

4.5 Magnetic and transport studies of a metamagnetic insulator/topological insulator system

We found that *EuSe* grows in (001) direction on *Bi₂Se₃*, which is different from (111) growth of *EuS*. An observed enhancement of AFM-FiM transition and strong hysteresis in *EuSe* thin film might provide an applicable way to control magnetic order and phase transition by tuning the film thickness. Furthermore, (001) growth of *EuSe* on *Bi₂Se₃* may provide an opportunity to realize an AFM interface with TSS.

A combination of PNR results(reduction of in-plane magnetization at the interface between *EuSe* and *Bi₂Se₃* when bulk *EuSe* is fully ferromagnetic) and transport data indicates AFM coupling at the *EuSe/Bi₂Se₃* interface, in contrast to the FM interfacial coupling observed at the *EuS/Bi₂Se₃* interface. Modulation of magneto-conductance at high magnetic field ($> 0.5T$) in microscopic samples suggests formation of magnetic domains at the interface.

Control of phase transition dynamics is a key for the successful realization of selective gapping of TSS in magnetic material/TI heterostructures. An AFM coupling between *EuSe*(001) and *Bi₂Se₃* is indicated from our transport and magnetization studies. It seems that this

AFM coupling is not strong enough to gap the TSS. To realize an FM interface with TSS in *EuSe*-based topological heterostructures it is necessary to develop suitable underlayer TI layers with similar lattice structures and matched lattice parameters.

REFERENCES

- [1] J. Alicea, “New directions in the pursuit of majorana fermions in solid state systems,” *Reports on Progress in Physics*, vol. 75, no. 7, p. 076 501, 2012, ISSN: 0034-4885. DOI: [10.1088/0034-4885/75/7/076501](https://doi.org/10.1088/0034-4885/75/7/076501).
- [2] C. Beenakker, “Search for majorana fermions in superconductors,” *Annual Review of Condensed Matter Physics*, vol. 4, no. 1, pp. 113–136, 2013, ISSN: 1947-5454. DOI: [10.1146/annurev-conmatphys-030212-184337](https://doi.org/10.1146/annurev-conmatphys-030212-184337).
- [3] R. M. Lutchyn, J. D. Sau, and S. D. Sarma, “Majorana fermions and a topological phase transition in semiconductor-superconductor heterostructures,” *Physical Review Letters*, vol. 105, no. 7, p. 077 001, 2015, ISSN: 0031-9007. DOI: [10.1103/physrevlett.105.077001](https://doi.org/10.1103/physrevlett.105.077001).
- [4] Y. Oreg, G. Refael, and F. von Oppen, “Helical liquids and majorana bound states in quantum wires,” *Physical Review Letters*, vol. 105, no. 17, p. 177 002, 2010, ISSN: 0031-9007. DOI: [10.1103/physrevlett.105.177002](https://doi.org/10.1103/physrevlett.105.177002).
- [5] M. Z. Hasan and J. E. Moore, “Three-dimensional topological insulators,” *Annual Review of Condensed Matter Physics*, vol. 2, no. 1, pp. 55–78, 2011, ISSN: 1947-5454. DOI: [10.1146/annurev-conmatphys-062910-140432](https://doi.org/10.1146/annurev-conmatphys-062910-140432).
- [6] J. Maciejko, T. L. Hughes, and S.-C. Zhang, “The quantum spin hall effect,” *Annual Review of Condensed Matter Physics*, vol. 2, no. 1, pp. 31–53, 2011, ISSN: 1947-5454. DOI: [10.1146/annurev-conmatphys-062910-140538](https://doi.org/10.1146/annurev-conmatphys-062910-140538).
- [7] V. Fal’ko and S. Iordanskii, “Spin-orbit coupling effect on quantum hall ferromagnets with vanishing zeeman energy,” *Physical Review Letters*, vol. 84, pp. 127–30, 2000.
- [8] A. Kazakov, G. Simion, Y. Lyanda-Geller, V. Kolkovsky, Z. Adamus, G. Karczewski, T. Wojtowicz, and L. P. Rokhinson, “Mesoscopic transport in electrostatically defined spin-full channels in quantum Hall ferromagnets,” *Physical Review Letters*, vol. 119, p. 046 803, 4 Jul. 2017. DOI: [10.1103/PhysRevLett.119.046803](https://doi.org/10.1103/PhysRevLett.119.046803).
- [9] G. Simion, A. Kazakov, L. P. Rokhinson, T. Wojtowicz, and Y. B. Lyanda-Geller, “Impurity-generated non-abelions,” *Physical Review B*, vol. 97, no. 24, p. 245 107, 2018, ISSN: 2469-9950. DOI: [10.1103/physrevb.97.245107](https://doi.org/10.1103/physrevb.97.245107).
- [10] Y. Ronen, Y. Cohen, D. Banitt, M. Heiblum, and V. Umansky, “Robust integer and fractional helical modes in the quantum hall effect,” *Nature Physics*, vol. 14, no. 4, pp. 411–416, 2018, ISSN: 1745-2473. DOI: [10.1038/s41567-017-0035-2](https://doi.org/10.1038/s41567-017-0035-2).

- [11] T. Ando, A. B. Fowler, and F. Stern, “Electronic properties of two-dimensional systems,” *Reviews of Modern Physics*, vol. 54, no. 2, pp. 437–672, 1982. DOI: [10.1103/revmodphys.54.437](https://doi.org/10.1103/revmodphys.54.437).
- [12] K. v. Klitzing, G. Dorda, and M. Pepper, “New method for high-accuracy determination of the fine-structure constant based on quantized hall resistance,” *Physical Review Letters*, vol. 45, no. 6, pp. 494–497, Aug. 1980. DOI: [10.1103/physrevlett.45.494](https://doi.org/10.1103/physrevlett.45.494).
- [13] D. C. Tsui, H. L. Stormer, and A. C. Gossard, “Two-dimensional magnetotransport in the extreme quantum limit,” in *Quantum Hall Effect: A Perspective*, Springer Netherlands, 1982, pp. 212–215. DOI: [10.1007/978-94-010-9709-3_22](https://doi.org/10.1007/978-94-010-9709-3_22).
- [14] V. Umansky, M. Heiblum, Y. Levinson, J. Smet, J. N?bler, and M. Dolev, “MBE growth of ultra-low disorder 2deg with mobility exceeding $35 \times 10^6 \text{cm}^2/\text{vs}$,” *Journal of Crystal Growth*, vol. 311, no. 7, pp. 1658–1661, 2009, ISSN: 0022-0248. DOI: [10.1016/j.jcrysgro.2008.09.151](https://doi.org/10.1016/j.jcrysgro.2008.09.151).
- [15] Z. Wan, A. Kazakov, M. J. Manfra, L. N. Pfeiffer, K. W. West, and L. P. Rokhinson, “Induced superconductivity in high-mobility two-dimensional electron gas in gallium arsenide heterostructures,” *Nature Communications*, vol. 6, no. 1, 2015, ISSN: 2041-1723. DOI: [10.1038/ncomms8426](https://doi.org/10.1038/ncomms8426).
- [16] P. T. Coleridge, R. Stoner, and R. Fletcher, “Low-field transport coefficients in GaAs/ga1-xAlxAs heterostructures,” *Physical Review B*, vol. 39, no. 2, pp. 1120–1124, Jan. 1989. DOI: [10.1103/physrevb.39.1120](https://doi.org/10.1103/physrevb.39.1120).
- [17] S. Baer and K. Ensslin, “The quantum hall effect,” in *Transport Spectroscopy of Confined Fractional Quantum Hall Systems*, Springer International Publishing, 2015, pp. 21–45. DOI: [10.1007/978-3-319-21051-3_3](https://doi.org/10.1007/978-3-319-21051-3_3).
- [18] M. Büttiker, “Absence of backscattering in the quantum hall effect in multiprobe conductors,” *Physical Review B*, vol. 38, no. 14, pp. 9375–9389, 1988, ISSN: 01631829. DOI: [10.1103/physrevb.38.9375](https://doi.org/10.1103/physrevb.38.9375).
- [19] D. Tong, *Lectures on the quantum hall effect*, ed. by D. Tong, <https://www.damtp.cam.ac.uk/user/tong/> 2016.
- [20] B. Kramer and A. MacKinnon, “Localization: Theory and experiment,” *Reports on Progress in Physics*, vol. 56, no. 12, pp. 1469–1564, 1993. DOI: [10.1088/0034-4885/56/12/001](https://doi.org/10.1088/0034-4885/56/12/001).
- [21] J. T. Chalker, P. Carra, and K. A. Benedict, “Weak localization and the integer quantum hall effect,” *Europhysics Letters (EPL)*, vol. 5, no. 2, pp. 163–168, Jan. 1988, ISSN: 0295-5075. DOI: [10.1209/0295-5075/5/2/013](https://doi.org/10.1209/0295-5075/5/2/013).

- [22] R. B. Laughlin, “Quantized hall conductivity in two dimensions,” *Physical Review B*, vol. 23, no. 10, pp. 5632–5633, 1981. DOI: [10.1103/physrevb.23.5632](https://doi.org/10.1103/physrevb.23.5632).
- [23] D. C. Tsui, H. L. Stormer, and A. C. Gossard, “Two-dimensional magnetotransport in the extreme quantum limit,” *Physical Review Letters*, vol. 48, no. 22, pp. 1559–1562, May 1982. DOI: [10.1103/physrevlett.48.1559](https://doi.org/10.1103/physrevlett.48.1559).
- [24] O. I. Stern, “Spin phenomena in the fractional quantum hall effect: Nmr and magnetotransport studies,” PhD thesis, Physik der Universität Stuttgart, 2005.
- [25] S. D. Sarma and A. Pinczuk, *Perspectives on Quantum Hall Effects*. Wiley, New York, 1996.
- [26] O. Heinonen, *Composite Fermions*. WORLD SCIENTIFIC, Oct. 1998. DOI: [10.1142/3894](https://doi.org/10.1142/3894).
- [27] R. B. Laughlin, “Anomalous quantum hall effect: An incompressible quantum fluid with fractionally charged excitations,” *Physical Review Letters*, vol. 50, no. 18, pp. 1395–1398, 1983, ISSN: 0031-9007. DOI: [10.1103/physrevlett.50.1395](https://doi.org/10.1103/physrevlett.50.1395).
- [28] R. B. Laughlin, “Nobel lecture: Fractional quantization,” *Reviews of Modern Physics*, vol. 71, no. 4, pp. 863–874, Jul. 1999, ISSN: 0034-6861. DOI: [10.1103/revmodphys.71.863](https://doi.org/10.1103/revmodphys.71.863).
- [29] J. K. Jain, “Composite-fermion approach for the fractional quantum hall effect,” *Physical Review Letters*, vol. 63, no. 2, pp. 199–202, Jul. 1989. DOI: [10.1103/physrevlett.63.199](https://doi.org/10.1103/physrevlett.63.199).
- [30] J. K. Jain, “Theory of the fractional quantum hall effect,” *Physical Review B*, vol. 41, no. 11, pp. 7653–7665, 1990. DOI: [10.1103/physrevb.41.7653](https://doi.org/10.1103/physrevb.41.7653).
- [31] B. I. Halperin, P. A. Lee, and N. Read, “Theory of the half-filled landau level,” *Physical Review B*, vol. 47, no. 12, pp. 7312–7343, Mar. 1993. DOI: [10.1103/physrevb.47.7312](https://doi.org/10.1103/physrevb.47.7312).
- [32] V. J. Goldman, B. Su, and J. K. Jain, “Detection of composite fermions by magnetic focusing,” *Physical Review Letters*, vol. 72, no. 13, pp. 2065–2068, Mar. 1994. DOI: [10.1103/physrevlett.72.2065](https://doi.org/10.1103/physrevlett.72.2065).
- [33] R. L. Willett, R. R. Ruel, K. W. West, and L. N. Pfeiffer, “Experimental demonstration of a fermi surface at one-half filling of the lowest landau level,” *Physical Review Letters*, vol. 71, no. 23, pp. 3846–3849, 1993, ISSN: 0031-9007. DOI: [10.1103/physrevlett.71.3846](https://doi.org/10.1103/physrevlett.71.3846).

- [34] A. H. MacDonald, “Edge states in the fractional-quantum-hall-effect regime,” *Physical Review Letters*, vol. 64, no. 2, pp. 220–223, 1990, ISSN: 0031-9007. DOI: [10.1103/physrevlett.64.220](https://doi.org/10.1103/physrevlett.64.220).
- [35] R. C. Ashoori, H. L. Stormer, L. N. Pfeiffer, K. W. Baldwin, and K. West, “Edge magnetoplasmons in the time domain,” *Physical Review B*, vol. 45, no. 7, pp. 3894–3897, 1992, ISSN: 0163-1829. DOI: [10.1103/physrevb.45.3894](https://doi.org/10.1103/physrevb.45.3894).
- [36] R. Sabo, I. Gurman, A. Rosenblatt, F. Lafont, D. Banitt, J. Park, M. Heiblum, Y. Gefen, V. Umansky, and D. Mahalu, “Edge reconstruction in fractional quantum hall states,” *Nature Physics*, vol. 13, no. 5, pp. 491–496, 2017, ISSN: 1745-2473. DOI: [10.1038/nphys4010](https://doi.org/10.1038/nphys4010).
- [37] C. L. Kane, M. P. A. Fisher, and J. Polchinski, “Randomness at the edge: Theory of quantum hall transport at filling $\nu=2/3$,” *Physical Review Letters*, vol. 72, no. 26, pp. 4129–4132, 1994, ISSN: 0031-9007. DOI: [10.1103/physrevlett.72.4129](https://doi.org/10.1103/physrevlett.72.4129).
- [38] Y. Meir, “Composite edge states in the $\nu=2/3$ fractional quantum hall regime,” *Physical Review Letters*, vol. 72, no. 16, pp. 2624–2627, 1994, ISSN: 0031-9007. DOI: [10.1103/physrevlett.72.2624](https://doi.org/10.1103/physrevlett.72.2624).
- [39] J. Wang, Y. Meir, and Y. Gefen, “Edge reconstruction in the $\nu=2/3$ fractional quantum hall state,” *Physical Review Letters*, vol. 111, no. 24, 2013, ISSN: 0031-9007. DOI: [10.1103/physrevlett.111.246803](https://doi.org/10.1103/physrevlett.111.246803).
- [40] A. Bid, N. Ofek, H. Inoue, M. Heiblum, C. L. Kane, V. Umansky, and D. Mahalu, “Observation of neutral modes in the fractional quantum hall regime,” *Nature*, vol. 466, no. 7306, pp. 585–590, 2010, ISSN: 0028-0836. DOI: [10.1038/nature09277](https://doi.org/10.1038/nature09277). [Online]. Available: <http://dx.doi.org/10.1038/nature09277>.
- [41] I. Gurman, R. Sabo, M. Heiblum, V. Umansky, and D. Mahalu, “Extracting net current from an upstream neutral mode in the fractional quantum hall regime,” *Nature Communications*, vol. 3, no. 1, 2012, ISSN: 2041-1723. DOI: [10.1038/ncomms2305](https://doi.org/10.1038/ncomms2305).
- [42] H. Inoue, A. Grivnin, Y. Ronen, M. Heiblum, V. Umansky, and D. Mahalu, “Proliferation of neutral modes in fractional quantum hall states,” *Nature Communications*, vol. 5, no. 1, 2014, ISSN: 2041-1723. DOI: [10.1038/ncomms5067](https://doi.org/10.1038/ncomms5067).
- [43] A. Rosenblatt, F. Lafont, I. Levkivskyi, R. Sabo, I. Gurman, D. Banitt, M. Heiblum, and V. Umansky, “Transmission of heat modes across a potential barrier,” *Nature Communications*, vol. 8, no. 1, 2017, ISSN: 2041-1723. DOI: [10.1038/s41467-017-02433-z](https://doi.org/10.1038/s41467-017-02433-z).

- [44] C. W. J. Beenakker, “Edge channels for the fractional quantum hall effect,” *Physical Review Letters*, vol. 64, no. 2, pp. 216–219, 1990, ISSN: 0031-9007. DOI: [10.1103/physrevlett.64.216](https://doi.org/10.1103/physrevlett.64.216).
- [45] A. M. Chang and J. E. Cunningham, “Transport evidence for phase separation into spatial regions of different fractional quantum hall fluids near the boundary of a two-dimensional electron gas,” *Physical Review Letters*, vol. 69, no. 14, pp. 2114–2117, 1992, ISSN: 0031-9007. DOI: [10.1103/physrevlett.69.2114](https://doi.org/10.1103/physrevlett.69.2114).
- [46] A. Bid, N. Ofek, M. Heiblum, V. Umansky, and D. Mahalu, “Shot noise and charge at the $2/3$ composite fractional quantum hall state,” *Physical Review Letters*, vol. 103, no. 23, p. 236 802, 2009, ISSN: 0031-9007. DOI: [10.1103/physrevlett.103.236802](https://doi.org/10.1103/physrevlett.103.236802).
- [47] F. Lafont, A. Rosenblatt, M. Heiblum, and V. Umansky, “Counter-propagating charge transport in the quantum hall effect regime,” *Science*, vol. 363, no. 6422, pp. 54–57, 2019, ISSN: 0036-8075. DOI: [10.1126/science.aar3766](https://doi.org/10.1126/science.aar3766).
- [48] J. P. Eisenstein, H. L. Stormer, L. Pfeiffer, and K. W. West, “Evidence for a phase transition in the fractional quantum hall effect,” *Physical Review Letters*, vol. 62, no. 13, pp. 1540–1543, 1989, ISSN: 0031-9007. DOI: [10.1103/physrevlett.62.1540](https://doi.org/10.1103/physrevlett.62.1540).
- [49] R. Clark and P. Maksym, “Fractional quantum hall effect in a spin,” *Physics World*, vol. 2, no. 9, pp. 39–46, 1989, ISSN: 0953-8585. DOI: [10.1088/2058-7058/2/9/23](https://doi.org/10.1088/2058-7058/2/9/23).
- [50] I. V. Kukushkin, K. v. Klitzing, and K. Eberl, “Spin polarization of composite fermions: Measurements of the fermi energy,” *Physical Review Letters*, vol. 82, no. 18, pp. 3665–3668, 1999, ISSN: 0031-9007. DOI: [10.1103/physrevlett.82.3665](https://doi.org/10.1103/physrevlett.82.3665).
- [51] J. Hayakawa, K. Muraki, and G. Yusa, “Real-space imaging of fractional quantum hall liquids,” *Nature Nanotechnology*, vol. 8, no. 1, pp. 31–35, Dec. 2013, ISSN: 1748-3387. DOI: [10.1038/nnano.2012.209](https://doi.org/10.1038/nnano.2012.209).
- [52] O. Stern, N. Freytag, A. Fay, W. Dietsche, J. Smet, K. von Klitzing, D. Schuh, and W. Wegscheider, “NMR study of the electron spin polarization in the fractional quantum hall effect of a single quantum well: spectroscopic evidence for domain formation,” *Physical Review B*, vol. 70, no. 7, p. 075 318, 2004, ISSN: 1098-0121. DOI: [10.1103/physrevb.70.075318](https://doi.org/10.1103/physrevb.70.075318).
- [53] H. M. Yoo, K. W. Baldwin, K. West, L. Pfeiffer, and R. C. Ashoori, “Spin phase diagram of the interacting quantum hall liquid,” *Nature Physics*, vol. 16, no. 10, pp. 1022–1027, Jun. 2020, ISSN: 1745-2473. DOI: [10.1038/s41567-020-0946-1](https://doi.org/10.1038/s41567-020-0946-1).

- [54] R. Dingle, H. L. Störmer, A. C. Gossard, and W. Wiegmann, “Electron mobilities in modulation-doped semiconductor heterojunction superlattices,” *Applied Physics Letters*, vol. 33, no. 7, pp. 665–667, 1978, ISSN: 0003-6951. DOI: [10.1063/1.90457](https://doi.org/10.1063/1.90457).
- [55] J. P. Eisenstein, H. L. Stormer, L. N. Pfeiffer, and K. W. West, “Evidence for a spin transition in the $\nu=2/3$ fractional quantum hall effect,” *Physical Review B*, vol. 41, no. 11, pp. 7910–7913, 1990, ISSN: 0163-1829. DOI: [10.1103/physrevb.41.7910](https://doi.org/10.1103/physrevb.41.7910).
- [56] L. W. Engel, S. W. Hwang, T. Sajoto, D. C. Tsui, and M. Shayegan, “Fractional quantum hall effect at $\nu=2/3$ and $3/5$ in tilted magnetic fields,” *Physical Review B*, vol. 45, pp. 3418–3425, 7 Feb. 1992. DOI: [10.1103/PhysRevB.45.3418](https://doi.org/10.1103/PhysRevB.45.3418).
- [57] J. H. Smet, R. A. Deutschmann, W. Wegscheider, G. Abstreiter, and K. von Klitzing, “Ising ferromagnetism and domain morphology in the fractional quantum hall regime,” *Physical Review Letters*, vol. 86, no. 11, pp. 2412–2415, 2001. DOI: [10.1103/physrevlett.86.2412](https://doi.org/10.1103/physrevlett.86.2412).
- [58] S. Melinte, N. Freytag, M. Horvatić, C. Berthier, L. P. Lévy, V. Bayot, and M. Shayegan, “Nmr determination of 2d electron spin polarization at $\nu=1/2$,” *Physical Review Letters*, vol. 84, no. 2, pp. 354–357, Jan. 2000. DOI: [10.1103/physrevlett.84.354](https://doi.org/10.1103/physrevlett.84.354). eprint: [cond-mat/9908098](https://arxiv.org/abs/cond-mat/9908098).
- [59] M. Stern, B. A. Piot, Y. Vardi, V. Umansky, P. Plochocka, D. K. Maude, and I. Bar-Joseph, “Nmr probing of the spin polarization of the $\nu = 5/2$ quantum hall state,” *Physical Review Letters*, vol. 108, p. 066 810, 6 Feb. 2012. DOI: [10.1103/PhysRevLett.108.066810](https://doi.org/10.1103/PhysRevLett.108.066810).
- [60] C. Nayak, S. H. Simon, A. Stern, M. Freedman, and S. D. Sarma, “Non-abelian anyons and topological quantum computation,” *Reviews of Modern Physics*, vol. 80, no. 3, pp. 1083–1159, 2008, ISSN: 0034-6861. DOI: [10.1103/revmodphys.80.1083](https://doi.org/10.1103/revmodphys.80.1083).
- [61] J. M. Leinaas and J. Myrheim, “On the theory of identical particles,” *Il Nuovo Cimento B Series 11*, vol. 37, no. 1, pp. 1–23, 1977, ISSN: 1826-9877. DOI: [10.1007/bf02727953](https://doi.org/10.1007/bf02727953).
- [62] F. Wilczek, “Quantum mechanics of fractional-spin particles,” *Physical Review Letters*, vol. 49, no. 14, pp. 957–959, 1982, ISSN: 0031-9007. DOI: [10.1103/physrevlett.49.957](https://doi.org/10.1103/physrevlett.49.957).
- [63] A. Y. Kitaev, “Unpaired majorana fermions in quantum wires,” *Physics-Uspekhi*, vol. 44, no. 10S, pp. 131–136, Oct. 2001, ISSN: 1468-4780. DOI: [10.1070/1063-7869/44/10s/s29](https://doi.org/10.1070/1063-7869/44/10s/s29).

- [64] G. Giuliani and G. Vignale, *Quantum theory of the electron liquid*. Cambridge University Press, 2005.
- [65] M. Baraban, N. E. Bonesteel, and S. H. Simon, “Resources required for topological quantum factoring,” *Physical Review A*, vol. 81, no. 6, p. 062317, 2010, ISSN: 1050-2947. DOI: [10.1103/physreva.81.062317](https://doi.org/10.1103/physreva.81.062317).
- [66] P. Fendley, “Parafermionic edge zero modes in Zn-invariant spin chains,” *Journal of Statistical Mechanics: Theory and Experiment*, vol. 2012, no. 11, P11020, 2012, ISSN: 1742-5468. DOI: [10.1088/1742-5468/2012/11/p11020](https://doi.org/10.1088/1742-5468/2012/11/p11020).
- [67] J. Alicea and P. Fendley, “Topological phases with parafermions: Theory and blueprints,” *Annual Review of Condensed Matter Physics*, vol. 7, no. 1, pp. 119–139, 2016, ISSN: 1947-5454. DOI: [10.1146/annurev-conmatphys-031115-011336](https://doi.org/10.1146/annurev-conmatphys-031115-011336).
- [68] R. S. K. Mong, D. J. Clarke, J. Alicea, N. H. Lindner, P. Fendley, C. Nayak, Y. Oreg, A. Stern, E. Berg, K. Shtengel, and M. P. A. Fisher, “Universal topological quantum computation from a superconductor-Abelian quantum hall heterostructure,” *Physical Review X*, vol. 4, p. 011036, 1 Mar. 2014. DOI: [10.1103/PhysRevX.4.011036](https://doi.org/10.1103/PhysRevX.4.011036).
- [69] D. J. Clarke, J. Alicea, and K. Shtengel, “Exotic non-abelian anyons from conventional fractional quantum hall states,” *Nature Communications*, vol. 4, no. 1, Jan. 2013, ISSN: 2041-1723. DOI: [10.1038/ncomms2340](https://doi.org/10.1038/ncomms2340).
- [70] N. H. Lindner, E. Berg, G. Refael, and A. Stern, “Fractionalizing majorana fermions: Non-abelian statistics on the edges of abelian quantum hall states,” *Physical Review X*, vol. 2, no. 4, p. 041002, 2012, ISSN: 2160-3308. DOI: [10.1103/physrevx.2.041002](https://doi.org/10.1103/physrevx.2.041002).
- [71] A. Vaezi, “Superconducting analogue of the parafermion fractional quantum hall states,” *Physical Review X*, vol. 4, no. 3, p. 031009, 2014, ISSN: 2160-3308. DOI: [10.1103/physrevx.4.031009](https://doi.org/10.1103/physrevx.4.031009).
- [72] B. Verdene, J. Martin, G. Gamez, J. Smet, K. von Klitzing, D. Mahalu, D. Schuh, G. Abstreiter, and A. Yacoby, “Microscopic manifestation of the spin phase transition at filling factor $2/3$,” *Nature Physics*, vol. 3, no. 6, pp. 392–396, Jun. 2007, ISSN: 1745-2473. DOI: [10.1038/nphys588](https://doi.org/10.1038/nphys588).
- [73] J. Hayakawa, K. Muraki, and G. Yusa, “Real-space imaging of fractional quantum Hall liquids,” *Nature Nanotechnology*, vol. 8, no. 1, pp. 31–35, Dec. 2012. DOI: [10.1038/nnano.2012.209](https://doi.org/10.1038/nnano.2012.209).
- [74] Y. Q. Li and J. H. Smet, *Spin Physics in Semiconductors*, M. I. Dyakonov, Ed. Springer Berlin Heidelberg, Berlin, Heidelberg, pp. 347-388, 2008.

- [75] S. Kronmüller, W. Dietsche, J. Weis, K. von Klitzing, W. Wegscheider, and M. Bichler, “New resistance maxima in the fractional quantum hall effect regime,” *Physical Review Letters*, vol. 81, no. 12, pp. 2526–2529, Sep. 1998. DOI: [10.1103/physrevlett.81.2526](https://doi.org/10.1103/physrevlett.81.2526).
- [76] K. Hashimoto, K. Muraki, T. Saku, and Y. Hirayama, “Electrically controlled nuclear spin polarization and relaxation by quantum-hall states,” *Physical Review Letters*, vol. 88, no. 17, Apr. 2002. DOI: [10.1103/physrevlett.88.176601](https://doi.org/10.1103/physrevlett.88.176601).
- [77] M. Dobers, K. v. Klitzing, J. Schneider, G. Weimann, and K. Ploog, “Electrical detection of nuclear magnetic resonance in GaAs-AlxGa1-xAs Heterostructures,” *Physical Review Letters*, vol. 61, no. 14, pp. 1650–1653, Oct. 1988. DOI: [10.1103/physrevlett.61.1650](https://doi.org/10.1103/physrevlett.61.1650).
- [78] D. C. Dixon, K. R. Wald, P. L. McEuen, and M. R. Melloch, “Dynamic nuclear polarization at the edge of a two-dimensional electron gas,” *Physical Review B*, vol. 56, no. 8, pp. 4743–4750, Aug. 1997. DOI: [10.1103/physrevb.56.4743](https://doi.org/10.1103/physrevb.56.4743).
- [79] T. Machida, S. Ishizuka, T. Yamazaki, S. Komiyama, K. Muraki, and Y. Hirayama, “Spin polarization of fractional quantum hall edge channels studied by dynamic nuclear polarization,” *Physical Review B*, vol. 65, no. 23, May 2002. DOI: [10.1103/physrevb.65.233304](https://doi.org/10.1103/physrevb.65.233304).
- [80] W. Desrat, D. K. Maude, M. Potemski, J. C. Portal, Z. R. Wasilewski, and G. Hill, “Resistively detected nuclear magnetic resonance in the quantum hall regime: Possible evidence for a skyrme crystal,” *Physical Review Letters*, vol. 88, no. 25, Jun. 2002. DOI: [10.1103/physrevlett.88.256807](https://doi.org/10.1103/physrevlett.88.256807).
- [81] S. E. Barrett, R. Tycko, L. N. Pfeiffer, and K. W. West, “Directly detected nuclear magnetic resonance of optically pumped GaAs quantum wells,” *Physical Review Letters*, vol. 72, no. 9, pp. 1368–1371, Feb. 1994. DOI: [10.1103/physrevlett.72.1368](https://doi.org/10.1103/physrevlett.72.1368).
- [82] S. M. Girvin, “The quantum hall effect: Novel excitations and broken symmetries,” in *Aspects topologiques de la physique en basse dimension. Topological aspects of low dimensional systems*, Springer Berlin Heidelberg, Jul. 1, 1999, pp. 53–175. DOI: [10.1007/3-540-46637-1_2](https://doi.org/10.1007/3-540-46637-1_2).
- [83] S. E. Barrett, G. Dabbagh, L. N. Pfeiffer, K. W. West, and R. Tycko, “Optically pumped NMR evidence for finite-size skyrmions in GaAs quantum wells near landau level filling $\nu=1$,” *Physical Review Letters*, vol. 74, no. 25, pp. 5112–5115, Jun. 1995, ISSN: 0031-9007. DOI: [10.1103/physrevlett.74.5112](https://doi.org/10.1103/physrevlett.74.5112).

- [84] S. L. Sondhi, A. Karlhede, S. A. Kivelson, and E. H. Rezayi, “Skyrmions and the crossover from the integer to fractional quantum hall effect at small zeeman energies,” *Physical Review B*, vol. 47, no. 24, pp. 16 419–16 426, Jun. 1993, ISSN: 0163-1829. DOI: [10.1103/physrevb.47.16419](https://doi.org/10.1103/physrevb.47.16419).
- [85] D. R. Leadley, R. J. Nicholas, D. K. Maude, A. N. Utjuzh, J. C. Portal, J. J. Harris, and C. T. Foxon, “Fractional quantum hall effect measurements at zero g factor,” *Physical Review Letters*, vol. 79, no. 21, pp. 4246–4249, Nov. 1997. DOI: [10.1103/physrevlett.79.4246](https://doi.org/10.1103/physrevlett.79.4246).
- [86] X.-G. Wen, “Colloquium : Zoo of quantum-topological phases of matter,” *Reviews of Modern Physics*, vol. 89, no. 4, Dec. 2017, ISSN: 0034-6861. DOI: [10.1103/revmodphys.89.041004](https://doi.org/10.1103/revmodphys.89.041004).
- [87] M. Z. Hasan and C. L. Kane, “Topological insulators,” *Reviews of Modern Physics*, vol. 82, pp. 3045–3067, 4 Nov. 2010. DOI: [10.1103/RevModPhys.82.3045](https://doi.org/10.1103/RevModPhys.82.3045).
- [88] C. L. Kane and E. J. Mele, “Quantum spin hall effect in graphene,” *Physical Review Letters*, vol. 95, no. 22, Nov. 2005. DOI: [10.1103/physrevlett.95.226801](https://doi.org/10.1103/physrevlett.95.226801).
- [89] B. A. Bernevig, T. L. Hughes, and S.-C. Zhang, “Quantum spin hall effect and topological phase transition in HgTe quantum wells,” *Science*, vol. 314, no. 5806, pp. 1757–1761, Dec. 2006, ISSN: 0036-8075. DOI: [10.1126/science.1133734](https://doi.org/10.1126/science.1133734).
- [90] M. König, S. Wiedmann, C. Brune, A. Roth, H. Buhmann, L. W. Molenkamp, X.-L. Qi, and S.-C. Zhang, “Quantum spin hall insulator state in HgTe quantum wells,” *Science*, vol. 318, no. 5851, pp. 766–770, Nov. 2007, ISSN: 0036-8075. DOI: [10.1126/science.1148047](https://doi.org/10.1126/science.1148047).
- [91] M. Mogi, M. Kawamura, A. Tsukazaki, R. Yoshimi, K. S. Takahashi, M. Kawasaki, and Y. Tokura, “Tailoring tricolor structure of magnetic topological insulator for robust axion insulator,” *Science Advances*, vol. 3, no. 10, eaao1669, Oct. 2017. DOI: [10.1126/sciadv.aao1669](https://doi.org/10.1126/sciadv.aao1669).
- [92] A. M. Essin, J. E. Moore, and D. Vanderbilt, “Erratum: Magnetoelectric polarizability and axion electrodynamics in crystalline insulators,” *Physical Review Letters*, vol. 103, no. 25, Dec. 2009, ISSN: 0031-9007. DOI: [10.1103/physrevlett.103.259902](https://doi.org/10.1103/physrevlett.103.259902).
- [93] M. Mogi, M. Kawamura, R. Yoshimi, A. Tsukazaki, Y. Kozuka, N. Shirakawa, K. S. Takahashi, M. Kawasaki, and Y. Tokura, “A magnetic heterostructure of topological insulators as a candidate for an axion insulator,” *Nature Materials*, vol. 16, no. 5, pp. 516–521, Feb. 2017. DOI: [10.1038/nmat4855](https://doi.org/10.1038/nmat4855).

- [94] V. P. Ningrum, B. Liu, W. Wang, Y. Yin, Y. Cao, C. Zha, H. Xie, X. Jiang, Y. Sun, S. Qin, X. Chen, T. Qin, C. Zhu, L. Wang, and W. Huang, “Recent advances in two-dimensional magnets: Physics and devices towards spintronic applications,” *Research*, vol. 2020, pp. 1–19, Jun. 2020. DOI: [10.34133/2020/1768918](https://doi.org/10.34133/2020/1768918).
- [95] C. Tang, C.-Z. Chang, G. Zhao, Y. Liu, Z. Jiang, C.-X. Liu, M. R. McCartney, D. J. Smith, T. Chen, J. S. Moodera, and J. Shi, “Above 400-k robust perpendicular ferromagnetic phase in a topological insulator,” *Science Advances*, vol. 3, no. 6, e1700307, Jun. 2017. DOI: [10.1126/sciadv.1700307](https://doi.org/10.1126/sciadv.1700307).
- [96] F. Katmis, V. Lauter, F. S. Nogueira, B. A. Assaf, M. E. Jamer, P. Wei, B. Satpati, J. W. Freeland, I. Eremin, D. Heiman, P. Jarillo-Herrero, and J. S. Moodera, “A high-temperature ferromagnetic topological insulating phase by proximity coupling,” *Nature*, vol. 533, no. 7604, pp. 513–516, 2016, ISSN: 0028-0836. DOI: [10.1038/nature17635](https://doi.org/10.1038/nature17635).
- [97] H. Wang, Y. Liu, P. Wu, W. Hou, Y. Jiang, X. Li, C. Pandey, D. Chen, Q. Yang, H. Wang, D. Wei, N. Lei, W. Kang, L. Wen, T. Nie, W. Zhao, and K. L. Wang, “Above room-temperature ferromagnetism in wafer-scale two-dimensional van der waals fe₃gete₂ tailored by a topological insulator,” *ACS Nano*, vol. 14, no. 8, pp. 10 045–10 053, Jul. 2020. DOI: [10.1021/acsnano.0c03152](https://doi.org/10.1021/acsnano.0c03152).
- [98] T. Liu, J. Kally, T. Pillsbury, C. Liu, H. Chang, J. Ding, Y. Cheng, M. Hilse, R. Engel-Herbert, A. Richardella, N. Samarth, and M. Wu, “Changes of magnetism in a magnetic insulator due to proximity to a topological insulator,” *Physical Review Letters*, vol. 125, no. 1, Jul. 2020. DOI: [10.1103/physrevlett.125.017204](https://doi.org/10.1103/physrevlett.125.017204).
- [99] T. Wojtowicz, M. Kutrowski, G. Karczewski, J. Kossut, B. K?nig, A. Keller, D. Yakovlev, A. Waag, J. Geurts, W. Ossau, G. Landwehr, I. Merkulov, F. Teran, and M. Potemski, “II–VI quantum structures with tunable electron -factor,” *Journal of Crystal Growth*, vol. 214-215, pp. 378–386, 2000, ISSN: 0022-0248. DOI: [10.1016/s0022-0248\(00\)00113-5](https://doi.org/10.1016/s0022-0248(00)00113-5).
- [100] R. Winkler, *Spin—Orbit Coupling Effects in Two-Dimensional Electron and Hole Systems*. Springer Berlin Heidelberg, 2003. DOI: [10.1007/b13586](https://doi.org/10.1007/b13586).
- [101] J. K. Jain, “Composite-fermion approach for the fractional quantum hall effect,” *Physical Review Letters*, vol. 63, no. 2, pp. 199–202, 1989, ISSN: 0031-9007. DOI: [10.1103/physrevlett.63.199](https://doi.org/10.1103/physrevlett.63.199).
- [102] J. Liang, G. Simion, and Y. Lyanda-Geller, “Parafermions, induced edge states, and domain walls in fractional quantum hall effect spin transitions,” *Physical Review B*, vol. 100, no. 7, p. 075 155, 2019, ISSN: 2469-9950. DOI: [10.1103/physrevb.100.075155](https://doi.org/10.1103/physrevb.100.075155).

- [103] X.-G. Wen, “Topological orders and edge excitations in fractional quantum hall states,” *Advances in Physics*, *44*, 405 (1995), vol. 44, no. 5, pp. 405–473, Jun. 15, 1995. DOI: [10.1080/00018739500101566](https://doi.org/10.1080/00018739500101566).
- [104] N. P. Sandler, C. d. C. Chamon, and E. Fradkin, “Noise measurements and fractional charge in fractional quantum hall liquids,” *Physical Review B*, vol. 59, pp. 12 521–12 536, 19 May 1999. DOI: [10.1103/PhysRevB.59.12521](https://doi.org/10.1103/PhysRevB.59.12521).
- [105] C. Nayak, M. P. A. Fisher, A. W. W. Ludwig, and H. H. Lin, “Resonant multilead point-contact tunneling,” *Physical Review B*, vol. 59, no. 24, pp. 15 694–15 704, 1999. DOI: [10.1103/physrevb.59.15694](https://doi.org/10.1103/physrevb.59.15694).
- [106] J. E. Moore and X.-G. Wen, “Critical points in edge tunneling between generic fractional quantum hall states,” *Physical Review B*, vol. 66, no. 11, p. 115 305, Jun. 19, 2001. DOI: [10.1103/physrevb.66.115305](https://doi.org/10.1103/physrevb.66.115305).
- [107] L. Brey, “Edge states of composite fermions,” *Physical Review B*, vol. 50, no. 16, pp. 11 861–11 871, 1994, ISSN: 0163-1829. DOI: [10.1103/physrevb.50.11861](https://doi.org/10.1103/physrevb.50.11861).
- [108] T. Wu, Z. Wan, A. Kazakov, Y. Wang, G. Simion, J. Liang, K. W. West, K. Baldwin, L. N. Pfeiffer, Y. Lyanda-Geller, and L. P. Rokhinson, “Formation of helical domain walls in the fractional quantum hall regime as a step toward realization of high-order non-abelian excitations,” *Physical Review B*, vol. 97, no. 24, p. 245 304, 2018, ISSN: 2469-9950. DOI: [10.1103/physrevb.97.245304](https://doi.org/10.1103/physrevb.97.245304).
- [109] K. Muraki, T. Saku, and Y. Hirayama, “Charge excitation and transport in pseudospin quantum hall ferromagnets,” *Physica E: Low-dimensional Systems and Nanostructures*, vol. 18, no. 1–3, pp. 107–108, 2003, 23rd International Conference on Low Temperature Physics (LT23), ISSN: 1386-9477. DOI: [http://dx.doi.org/10.1016/S1386-9477\(02\)01035-4](http://dx.doi.org/10.1016/S1386-9477(02)01035-4).
- [110] Y. Wang, V. Ponomarenko, K. W. West, K. Baldwin, L. N. Pfeiffer, Y. Lyanda-Geller, and L. P. Rokhinson, “Transport in helical luttinger liquids in the fractional quantum hall regime,” *arXiv:2101.00126*, Jan. 1, 2021.
- [111] S. S. Mandal and J. K. Jain, “Low-energy spin rotons in the fractional quantum hall effect,” *Physical Review B*, vol. 63, no. 20, p. 201 310, 2001. DOI: [10.1103/physrevb.63.201310](https://doi.org/10.1103/physrevb.63.201310).
- [112] A. C. Balram, U. Wurstbauer, A. Wójs, A. Pinczuk, and J. K. Jain, “Fractionally charged skyrmions in fractional quantum hall effect,” *Nature Communications*, vol. 6, no. 1, 2015. DOI: [10.1038/ncomms9981](https://doi.org/10.1038/ncomms9981).

- [113] R. Côté, A. H. MacDonald, L. Brey, H. A. Fertig, S. M. Girvin, and H. T. C. Stoof, “Collective excitations, NMR, and phase transitions in skyrme crystals,” *Physical Review Letters*, vol. 78, no. 25, pp. 4825–4828, 1997. DOI: [10.1103/physrevlett.78.4825](https://doi.org/10.1103/physrevlett.78.4825).
- [114] B. Schmidt, K. Bennaceur, S. Bilodeau, G. Gervais, L. Pfeiffer, and K. West, “Second landau level fractional quantum hall effects in the corbino geometry,” *Solid State Communications*, vol. 217, pp. 1–5, 2015, ISSN: 0038-1098. DOI: [10.1016/j.ssc.2015.05.005](https://doi.org/10.1016/j.ssc.2015.05.005).
- [115] R. Yu, W. Zhang, H.-J. Zhang, S.-C. Zhang, X. Dai, and Z. Fang, “Quantized anomalous hall effect in magnetic topological insulators,” *Science*, vol. 329, no. 5987, pp. 61–64, 2010. DOI: [10.1126/science.1187485](https://doi.org/10.1126/science.1187485).
- [116] C.-Z. Chang, J. Zhang, X. Feng, J. Shen, Z. Zhang, M. Guo, K. Li, Y. Ou, P. Wei, L.-L. Wang, Z.-Q. Ji, Y. Feng, S. Ji, X. Chen, J. Jia, X. Dai, Z. Fang, S.-C. Zhang, K. He, Y. Wang, L. Lu, X.-C. Ma, and Q.-K. Xue, “Experimental observation of the quantum anomalous hall effect in a magnetic topological insulator,” *Science*, vol. 340, no. 6129, pp. 167–170, May 28, 2016. DOI: [10.1126/science.1234414](https://doi.org/10.1126/science.1234414).
- [117] M. Mogi, R. Yoshimi, A. Tsukazaki, K. Yasuda, Y. Kozuka, K. S. Takahashi, M. Kawasaki, and Y. Tokura, “Magnetic modulation doping in topological insulators toward higher-temperature quantum anomalous hall effect,” *Applied Physics Letters*, vol. 107, no. 18, p. 182401, Nov. 5, 2015. DOI: [10.1063/1.4935075](https://doi.org/10.1063/1.4935075). arXiv: [1511.01724v1](https://arxiv.org/abs/1511.01724v1).
- [118] D. Xiao, J. Jiang, J.-H. Shin, W. Wang, F. Wang, Y.-F. Zhao, C. Liu, W. Wu, M. H. Chan, N. Samarth, and C.-Z. Chang, “Realization of the axion insulator state in quantum anomalous hall sandwich heterostructures,” *Physical Review Letters*, vol. 120, no. 5, p. 056801, Oct. 2, 2017. DOI: [10.1103/physrevlett.120.056801](https://doi.org/10.1103/physrevlett.120.056801).
- [119] L. Fu and C. L. Kane, “Superconducting proximity effect and majorana fermions at the surface of a topological insulator,” *Physical Review Letters*, vol. 100, no. 9, p. 096407, Jul. 11, 2007. DOI: [10.1103/physrevlett.100.096407](https://doi.org/10.1103/physrevlett.100.096407).
- [120] Y. Xu, I. Miotkowski, C. Liu, J. Tian, H. Nam, N. Alidoust, J. Hu, C.-K. Shih, M. Z. Hasan, and Y. P. Chen, “Observation of topological surface state quantum hall effect in an intrinsic three-dimensional topological insulator,” *Nature Physics*, vol. 10, no. 12, pp. 956–963, Sep. 12, 2014. DOI: [10.1038/nphys3140](https://doi.org/10.1038/nphys3140).

- [121] E. D. L. Rienks, S. Wimmer, J. Sánchez-Barriga, O. Caha, P. S. Mandal, J. Ružička, A. Ney, H. Steiner, V. V. Volobuev, H. Groiss, M. Albu, G. Kothleitner, J. Michalička, S. A. Khan, J. Minár, H. Ebert, G. Bauer, F. Freyse, A. Varykhalov, O. Rader, and G. Springholz, “Large magnetic gap at the dirac point in $\text{bi}_2\text{te}_3/\text{MnBi}_2\text{te}_4$ heterostructures,” *Nature*, vol. 576, no. 7787, pp. 423–428, 2019, ISSN: 0028-0836. DOI: [10.1038/s41586-019-1826-7](https://doi.org/10.1038/s41586-019-1826-7).
- [122] H. Sun, B. Xia, Z. Chen, Y. Zhang, P. Liu, Q. Yao, H. Tang, Y. Zhao, H. Xu, and Q. Liu, “Rational design principles of the quantum anomalous hall effect in superlatticelike magnetic topological insulators,” *Physical Review Letters*, vol. 123, no. 9, p. 096 401, May 29, 2019. DOI: [10.1103/physrevlett.123.096401](https://doi.org/10.1103/physrevlett.123.096401).
- [123] M. Nadeem, A. R. Hamilton, M. S. Fuhrer, and X. Wang, “Quantum anomalous hall effect in magnetic doped topological insulators and ferromagnetic spin-gapless semiconductors—a perspective review,” *Nano micro Small*, vol. 16, no. 42, p. 1 904 322, Dec. 22, 2020. DOI: [10.1002/sml.201904322](https://doi.org/10.1002/sml.201904322).
- [124] Y. Deng, Y. Yu, M. Z. Shi, Z. Guo, Z. Xu, J. Wang, X. H. Chen, and Y. Zhang, “Quantum anomalous hall effect in intrinsic magnetic topological insulator MnBi_2te_4 ,” *Science*, vol. 367, no. 6480, pp. 895–900, 2020. DOI: [10.1126/science.aax8156](https://doi.org/10.1126/science.aax8156).
- [125] P. Chen, Y. Zhang, Q. Yao, F. Tian, L. Li, Z. Qi, X. Liu, L. Liao, C. Song, J. Wang, J. Xia, G. Li, D. M. Burn, G. van der Laan, T. Hesjedal, S. Zhang, and X. Kou, “Tailoring the hybrid anomalous hall response in engineered magnetic topological insulator heterostructures,” *Nano Letters*, vol. 20, no. 3, pp. 1731–1737, Dec. 16, 2019. DOI: [10.1021/acs.nanolett.9b04932](https://doi.org/10.1021/acs.nanolett.9b04932).
- [126] S.-J. Chang, P.-Y. Chuang, C.-W. Chong, Y.-J. Chen, J.-C. A. Huang, P.-W. Chen, and Y.-C. Tseng, “Heterostructured ferromagnet–topological insulator with dual-phase magnetic properties,” *RSC Advances*, vol. 8, no. 14, pp. 7785–7791, 2018, ISSN: 2046-2069. DOI: [10.1039/c8ra00068a](https://doi.org/10.1039/c8ra00068a).
- [127] P. Wei, F. Katmis, B. A. Assaf, H. Steinberg, P. Jarillo-Herrero, D. Heiman, and J. S. Moodera, “Exchange-coupling-induced symmetry breaking in topological insulators,” *Physical Review Letters*, vol. 110, no. 18, p. 186 807, 2013, ISSN: 0031-9007. DOI: [10.1103/physrevlett.110.186807](https://doi.org/10.1103/physrevlett.110.186807).
- [128] A. Figueroa, F. Bonell, M. Cuxart, M. Valvidares, P. Gargiani, G. van der Laan, A. Mugarza, and S. Valenzuela, “Absence of magnetic proximity effect at the interface of bi_2se_3 and $(\text{bi},\text{sb})_2\text{te}_3$ with EuS ,” *Physical Review Letters*, vol. 125, no. 22, p. 226 801, 2020, ISSN: 0031-9007. DOI: [10.1103/physrevlett.125.226801](https://doi.org/10.1103/physrevlett.125.226801).

- [129] F. Wang, D. Xiao, W. Yuan, J. Jiang, Y.-F. Zhao, L. Zhang, Y. Yao, W. Liu, Z. Zhang, C. Liu, J. Shi, W. Han, M. H. W. Chan, N. Samarth, and C.-Z. Chang, “Observation of interfacial antiferromagnetic coupling between magnetic topological insulator and antiferromagnetic insulator,” *Nano Letters*, vol. 19, no. 5, pp. 2945–2952, Jan. 9, 2019. DOI: [10.1021/acs.nanolett.9b00027](https://doi.org/10.1021/acs.nanolett.9b00027).
- [130] Q. L. He, X. Kou, A. J. Grutter, G. Yin, L. Pan, X. Che, Y. Liu, T. Nie, B. Zhang, S. M. Disseler, B. J. Kirby, W. R. II, Q. Shao, K. Murata, X. Zhu, G. Yu, Y. Fan, M. Montazeri, X. Han, J. A. Borchers, and K. L. Wang, “Tailoring exchange couplings in magnetic topological-insulator/antiferromagnet heterostructures,” *Nature Materials*, vol. 16, no. 1, pp. 94–100, May 16, 2016. DOI: [10.1038/nmat4783](https://doi.org/10.1038/nmat4783).
- [131] A. Mauger and C. Godart, “The magnetic, optical, and transport properties of representatives of a class of magnetic semiconductors: The europium chalcogenides,” *Physics Reports*, vol. 141, no. 2-3, pp. 51–176, 1986, ISSN: 0370-1573. DOI: [10.1016/0370-1573\(86\)90139-0](https://doi.org/10.1016/0370-1573(86)90139-0).
- [132] I. Sanger, V. V. Pavlov, M. Bayer, and M. Fiebig, “Distribution of antiferromagnetic spin and twin domains in NiO,” *Physical Review B*, vol. 74, no. 14, Oct. 2006, ISSN: 1098-0121. DOI: [10.1103/physrevb.74.144401](https://doi.org/10.1103/physrevb.74.144401).
- [133] R. T. Lechner, G. Springholz, T. U. Sch?lli, J. Stangl, T. Schwarzl, and G. Bauer, “Strain induced changes in the magnetic phase diagram of metamagnetic HeteroepitaxialEuSe/PbSe_{1-x}TexMultilayers,” *Physical Review Letters*, vol. 94, no. 15, p. 157201, Apr. 2005, ISSN: 0031-9007. DOI: [10.1103/physrevlett.94.157201](https://doi.org/10.1103/physrevlett.94.157201).
- [134] R. Lechner, G. Springholz, T. Sch?lli, J. Stangl, T. Schwarzl, D. Lott, V. Leiner, A. Schreyer, H. Clemens, and G. Bauer, “Spin configurations in strained magnetic superlattices grown by molecular beam epitaxy,” *Physica E: Low-dimensional Systems and Nanostructures*, vol. 32, no. 1-2, pp. 379–382, 2006. DOI: [10.1016/j.physe.2005.12.075](https://doi.org/10.1016/j.physe.2005.12.075).
- [135] R. Griessen, M. Landolt, and H. Ott, “A new antiferromagnetic phase in EuSe below 1.8 k,” *Solid State Communications*, vol. 9, no. 24, pp. 2219–2223, 1971. DOI: [10.1016/0038-1098\(71\)90634-x](https://doi.org/10.1016/0038-1098(71)90634-x).
- [136] U. Kobler, R. Mueller, L. Smardz, D. Maier, K. Fischer, B. Olefs, and W. Zinn, “Biquadratic exchange interactions in the europium monochalcogenides,” *Zeitschrift fur Physik B Condensed Matter*, vol. 100, no. 4, pp. 497–506, Dec. 1996. DOI: [10.1007/s002570050153](https://doi.org/10.1007/s002570050153).

- [137] X. Liux, J. Wangx, L. Riney, S. Bac, D. J. Smith, M. McCartney, I. Khan, A. Hoffman, M. Dobrowolska, J. Furdyna, and B. Assaf, “Unraveling the structural and electronic properties of strained PbSe on GaAs,” *Journal of Crystal Growth*, p. 126 235, 2021. DOI: [10.1016/j.jcrysgro.2021.126235](https://doi.org/10.1016/j.jcrysgro.2021.126235).
- [138] X. Liu, D. J. Smith, J. Fan, Y.-H. Zhang, H. Cao, Y. P. Chen, J. Leiner, B. J. Kirby, M. Dobrowolska, and J. K. Furdyna, “Structural properties of bi2te3 and bi2se3 topological insulators grown by molecular beam epitaxy on GaAs(001) substrates,” *Applied Physics Letters*, vol. 99, no. 17, p. 171 903, Oct. 2011. DOI: [10.1063/1.3655995](https://doi.org/10.1063/1.3655995).
- [139] A. Richardella, D. M. Zhang, J. S. Lee, A. Koser, D. W. Rench, A. L. Yeats, B. B. Buckley, D. D. Awschalom, and N. Samarth, “Coherent heteroepitaxy of bi2se3 on GaAs (111)b,” *Applied Physics Letters*, vol. 97, no. 26, p. 262 104, 2010, ISSN: 0003-6951. DOI: [10.1063/1.3532845](https://doi.org/10.1063/1.3532845).
- [140] J. Kim, K.-W. Kim, H. Wang, J. Sinova, and R. Wu, “Understanding the giant enhancement of exchange interaction in bi2se3-EuS heterostructures,” *Physical Review Letters*, vol. 119, no. 2, p. 027 201, 2017. DOI: [10.1103/physrevlett.119.027201](https://doi.org/10.1103/physrevlett.119.027201).
- [141] R. Kirchschlager, W. Heiss, R. T. Lechner, G. Bauer, and G. Springholz, “Hysteresis loops of the energy band gap and effective g factor up to 18 000 for metamagnetic EuSe epilayers,” *Applied Physics Letters*, vol. 85, no. 1, pp. 67–69, 2004, ISSN: 0003-6951. DOI: [10.1063/1.1771454](https://doi.org/10.1063/1.1771454).
- [142] I. Suzuki, T. Koike, M. Itoh, T. Taniyama, and T. Sato, “Stability of ferromagnetic state of epitaxially grown ordered FeRh thin films,” *Journal of Applied Physics*, vol. 105, no. 7, 07E501, 2009, ISSN: 0021-8979. DOI: [10.1063/1.3054386](https://doi.org/10.1063/1.3054386).
- [143] T. A. Ostler, C. Barton, T. Thomson, and G. Hrkac, “Modeling the thickness dependence of the magnetic phase transition temperature in thin FeRh films,” *Physical Review B*, vol. 95, no. 6, p. 064 415, 2017, ISSN: 2469-9950. DOI: [10.1103/physrevb.95.064415](https://doi.org/10.1103/physrevb.95.064415).
- [144] C. Yu, H. Li, Y. Luo, L. Zhu, Z. Qian, and T. Zhou, “Thickness-dependent magnetic order and phase-transition dynamics in epitaxial fe-rich FeRh thin films,” *Physics Letters A*, vol. 383, no. 20, pp. 2424–2428, 2019, ISSN: 0375-9601. DOI: [10.1016/j.physleta.2019.04.058](https://doi.org/10.1016/j.physleta.2019.04.058).
- [145] U. Köbler, R. Mueller, L. Smardz, D. Maier, K. Fischer, B. Olefs, and W. Zinn, “Biquadratic exchange interactions in the europium monochalcogenides,” *Zeitschrift für Physik B Condensed Matter*, vol. 100, no. 4, pp. 497–506, 1996, ISSN: 0722-3277. DOI: [10.1007/s002570050153](https://doi.org/10.1007/s002570050153).

- [146] V. Lauter, H. Ambaye, R. Goyette, W.-T. H. Lee, and A. Parizzi, “Highlights from the magnetism reflectometer at the SNS,” *Physica B: Condensed Matter*, vol. 404, no. 17, pp. 2543–2546, Sep. 2009, ISSN: 0921-4526. DOI: [10.1016/j.physb.2009.06.021](https://doi.org/10.1016/j.physb.2009.06.021).
- [147] T. Zhu, Y. Yang, R. C. Yu, H. Ambaye, V. Lauter, and J. Q. Xiao, “The study of perpendicular magnetic anisotropy in CoFeB sandwiched by MgO and tantalum layers using polarized neutron reflectometry,” *Applied Physics Letters*, vol. 100, no. 20, p. 202 406, 2012, ISSN: 0003-6951. DOI: [10.1063/1.4718423](https://doi.org/10.1063/1.4718423).
- [148] S. Hikami, A. I. Larkin, and Y. Nagaoka, “Spin-orbit interaction and magnetoresistance in the two dimensional random system,” *Progress of Theoretical Physics*, vol. 63, no. 2, pp. 707–710, Feb. 1980, ISSN: 0033-068X. DOI: [10.1143/ptp.63.707](https://doi.org/10.1143/ptp.63.707).
- [149] J. Chen, H. J. Qin, F. Yang, J. Liu, T. Guan, F. M. Qu, G. H. Zhang, J. R. Shi, X. C. Xie, C. L. Yang, K. H. Wu, Y. Q. Li, and L. Lu, “Gate-voltage control of chemical potential and weak antilocalization in Bi₂Se₃,” *Physical Review Letters*, vol. 105, no. 17, p. 176 602, Oct. 2010. DOI: [10.1103/physrevlett.105.176602](https://doi.org/10.1103/physrevlett.105.176602).
- [150] H. Steinberg, J.-B. Laloë, V. Fatemi, J. S. Moodera, and P. Jarillo-Herrero, “Electrically tunable surface-to-bulk coherent coupling in topological insulator thin films,” *Physical Review B*, vol. 84, no. 23, p. 233 101, Dec. 2011, ISSN: 1098-0121. DOI: [10.1103/physrevb.84.233101](https://doi.org/10.1103/physrevb.84.233101).
- [151] J. G. Checkelsky, Y. S. Hor, R. J. Cava, and N. P. Ong, “Bulk band gap and surface state conduction observed in voltage-tuned crystals of the topological insulator Bi₂Se₃,” *Physical Review Letters*, vol. 106, no. 19, p. 196 801, May 2011, ISSN: 0031-9007. DOI: [10.1103/physrevlett.106.196801](https://doi.org/10.1103/physrevlett.106.196801).
- [152] M. Liu, C.-Z. Chang, Z. Zhang, Y. Zhang, W. Ruan, K. He, L.-l. Wang, X. Chen, J.-F. Jia, S.-C. Zhang, Q.-K. Xue, X. Ma, and Y. Wang, “Electron interaction-driven insulating ground state in Bi₂Se₃ topological insulators in the two-dimensional limit,” *Physical Review B*, vol. 83, no. 16, p. 165 440, Apr. 2011, ISSN: 1098-0121. DOI: [10.1103/physrevb.83.165440](https://doi.org/10.1103/physrevb.83.165440).
- [153] A. A. Taskin, S. Sasaki, K. Segawa, and Y. Ando, “Manifestation of topological protection in transport properties of Epitaxial Bi₂Se₃ thin films,” *Physical Review Letters*, vol. 109, no. 6, p. 066 803, Aug. 2012. DOI: [10.1103/physrevlett.109.066803](https://doi.org/10.1103/physrevlett.109.066803).
- [154] J. Tian, C. Chang, H. Cao, K. He, X. Ma, Q. Xue, and Y. P. Chen, “Quantum and classical magnetoresistance in ambipolar topological insulator transistors with gate-tunable bulk and surface conduction,” *Scientific Reports*, vol. 4, no. 1, p. 4859, May 2014. DOI: [10.1038/srep04859](https://doi.org/10.1038/srep04859).

- [155] B. L. Altshuler, A. G. Aronov, and D. E. Khmelnitsky, “Effects of electron-electron collisions with small energy transfers on quantum localisation,” *Journal of Physics C: Solid State Physics*, vol. 15, no. 36, pp. 7367–7386, Dec. 1982. DOI: [10.1088/0022-3719/15/36/018](https://doi.org/10.1088/0022-3719/15/36/018).
- [156] D. Natelson, R. L. Willett, K. W. West, and L. N. Pfeiffer, “Geometry-dependent dephasing in small metallic wires,” *Physical Review Letters*, vol. 86, no. 9, pp. 1821–1824, Jun. 20, 2000. DOI: [10.1103/physrevlett.86.1821](https://doi.org/10.1103/physrevlett.86.1821).
- [157] P. Mohanty, E. M. Q. Jariwala, and R. A. Webb, “Intrinsic decoherence in mesoscopic systems,” *Phys. Rev. Lett.* 77, 3366 (1997), vol. 78, no. 17, pp. 3366–3369, Oct. 10, 1997. DOI: [10.1103/physrevlett.78.3366](https://doi.org/10.1103/physrevlett.78.3366).
- [158] J. J. Lin and N. Giordano, “Electron scattering times from weak localization studies of au-pd films,” *Physical Review B*, vol. 35, p. 1071, 1987. DOI: [10.1103/?physrevb.35.1071](https://doi.org/10.1103/?physrevb.35.1071).
- [159] D. S. Golubev and A. D. Zaikin, “Quantum decoherence in disordered mesoscopic systems,” *Physical Review Letters*, vol. 81, no. 5, pp. 1074–1077, Oct. 8, 1997. DOI: [10.1103/physrevlett.81.1074](https://doi.org/10.1103/physrevlett.81.1074).
- [160] D. S. Golubev, A. D. Zaikin, and G. Schön, “On low-temperature dephasing by electron-electron interaction,” *Journal of Low Temperature Physics*, vol. 126, no. 3/4, pp. 1355–1376, 2002. DOI: [10.1023/a:1013800304448](https://doi.org/10.1023/a:1013800304448).
- [161] B. Altshuler, M. Gershenson, and I. Aleiner, “Phase relaxation of electrons in disordered conductors,” *Physica E: Low-dimensional Systems and Nanostructures*, vol. 3, no. 1-3, pp. 58–68, Oct. 1998, ISSN: 1386-9477. DOI: [10.1016/s1386-9477\(98\)00219-7](https://doi.org/10.1016/s1386-9477(98)00219-7).
- [162] M. Gershenson, “Low-temperature dephasing in disordered conductors: Experimental aspects,” *Annalen der Physik*, vol. 8, no. 7-9, pp. 559–568, Nov. 1999, ISSN: 0003-3804. DOI: [10.1002/\(sici\)1521-3889\(199911\)8:7/9<559::aid-andp559>3.0.co;2-7](https://doi.org/10.1002/(sici)1521-3889(199911)8:7/9<559::aid-andp559>3.0.co;2-7).
- [163] I. L. Aleiner, B. L. Altshuler, and M. G. Vavilov, “Absence of zero-temperature dephasing by electron-electron interaction,” *Journal of Low Temperature Physics*, vol. 126, no. 3/4, pp. 1377–1384, 2002. DOI: [10.1023/a:1013852321287](https://doi.org/10.1023/a:1013852321287).
- [164] Z. Ovadyahu, “Nonequilibrium dephasing in two-dimensional indium oxide films,” *Physical Review B*, vol. 63, no. 23, May 2001, ISSN: 0163-1829. DOI: [10.1103/physrevb.63.235403](https://doi.org/10.1103/physrevb.63.235403).
- [165] A. Kaminski and L. I. Glazman, “Electron energy relaxation in the presence of magnetic impurities,” *Phys. Rev. Lett.* 86, 2400 (2001), vol. 86, no. 11, pp. 2400–2403, Oct. 24, 2000. DOI: [10.1103/physrevlett.86.2400](https://doi.org/10.1103/physrevlett.86.2400).

- [166] A. B. Gougam, F. Pierre, H. Pothier, D. Esteve, and N. O. Birge, “Comparison of energy and phase relaxation in metallic wires,” *J. Low Temp. Phys.* *118*, 447–456 (2000), Dec. 8, 1999. arXiv: [cond-mat/9912137v1](https://arxiv.org/abs/cond-mat/9912137v1).
- [167] G. Göppert and H. Grabert, “Nonequilibrium electron distribution in the presence of kondo impurities,” *Phys. Rev. B* *64*, 033301 (2001), vol. 64, no. 3, Feb. 8, 2001. DOI: [10.1103/physrevb.64.033301](https://doi.org/10.1103/physrevb.64.033301).
- [168] J. J. Lin and J. P. Bird, “Recent experimental studies of electron dephasing in metal and semiconductor mesoscopic structures,” *Journal of Physics: Condensed Matter*, vol. 14, no. 18, R501–R596, Apr. 2002, ISSN: 0953-8984. DOI: [10.1088/0953-8984/14/18/201](https://doi.org/10.1088/0953-8984/14/18/201).
- [169] H. Tang, D. Liang, R. L. J. Qiu, and X. P. A. Gao, “Two-dimensional transport-induced linear magneto-resistance in topological insulator Bi_2Se_3 nanoribbons,” *ACS Nano*, vol. 5, no. 9, pp. 7510–7516, Aug. 2011, ISSN: 1936-0851. DOI: [10.1021/nm2024607](https://doi.org/10.1021/nm2024607).
- [170] Y. Yan, L.-X. Wang, D.-P. Yu, and Z.-M. Liao, “Large magnetoresistance in high mobility topological insulator Bi_2Se_3 ,” *Applied Physics Letters*, vol. 103, no. 3, p. 033 106, Jul. 2013, ISSN: 0003-6951. DOI: [10.1063/1.4813824](https://doi.org/10.1063/1.4813824).
- [171] H. T. He, H. C. Liu, B. K. Li, X. Guo, Z. J. Xu, M. H. Xie, and J. N. Wang, “Disorder-induced linear magnetoresistance in (221) topological insulator Bi_2Se_3 films,” *Applied Physics Letters*, vol. 103, no. 3, p. 031 606, Jul. 2013, ISSN: 0003-6951. DOI: [10.1063/1.4816078](https://doi.org/10.1063/1.4816078).
- [172] H. He, B. Li, H. Liu, X. Guo, Z. Wang, M. Xie, and J. Wang, “High-field linear magneto-resistance in topological insulator Bi_2Se_3 thin films,” *Applied Physics Letters*, vol. 100, no. 3, p. 032 105, Jan. 2012, ISSN: 0003-6951. DOI: [10.1063/1.3677669](https://doi.org/10.1063/1.3677669).
- [173] D. Kumar and A. Lakhani, “Large linear magnetoresistance from neutral defects in Bi_2Se_3 ,” *Physica Status Solidi-Rapid Research Letters*, vol. 12, p. 1 800 088, Jun. 29, 2016. arXiv: [1606.09059v1](https://arxiv.org/abs/1606.09059v1).
- [174] A. A. Abrikosov, “Quantum linear magnetoresistance; solution of an old mystery,” *Journal of Physics A: Mathematical and General*, vol. 36, no. 35, pp. 9119–9131, Aug. 2003, ISSN: 0305-4470. DOI: [10.1088/0305-4470/36/35/301](https://doi.org/10.1088/0305-4470/36/35/301).
- [175] M. M. Parish and P. B. Littlewood, “Non-saturating magnetoresistance in heavily disordered semiconductors,” *Nature*, vol. 426, no. 6963, pp. 162–165, Nov. 2003, ISSN: 0028-0836. DOI: [10.1038/nature02073](https://doi.org/10.1038/nature02073).

- [176] M. M. Parish and P. B. Littlewood, “Classical magnetotransport of inhomogeneous conductors,” *Physical Review B*, vol. 72, no. 9, p. 094 417, Sep. 2005, ISSN: 1098-0121. DOI: [10.1103/physrevb.72.094417](https://doi.org/10.1103/physrevb.72.094417).
- [177] A. A. Abrikosov, “Quantum magnetoresistance,” *Physical Review B*, vol. 58, no. 5, pp. 2788–2794, Aug. 1998, ISSN: 0163-1829. DOI: [10.1103/physrevb.58.2788](https://doi.org/10.1103/physrevb.58.2788).
- [178] A. A. Abrikosov, “Quantum linear magnetoresistance,” *Europhysics Letters (EPL)*, vol. 49, no. 6, pp. 789–793, Mar. 2000, ISSN: 0295-5075. DOI: [10.1209/epl/i2000-00220-2](https://doi.org/10.1209/epl/i2000-00220-2).
- [179] Y. Cohen, Y. Ronen, W. Yang, D. Banitt, J. Park, M. Heiblum, A. D. Mirlin, Y. Gefen, and V. Umansky, “Synthesizing a $\nu=2/3$ fractional quantum hall effect edge state from counter-propagating $\nu=1$ and $\nu=1/3$ states,” *Nature Communications*, vol. 10, no. 1, 2019, ISSN: 2041-1723. DOI: [10.1038/s41467-019-09920-5](https://doi.org/10.1038/s41467-019-09920-5).
- [180] F. Vigneau, R. Mizokuchi, D. C. Zanuz, X. Huang, S. Tan, R. Maurand, S. Frolov, A. Sammak, G. Scappucci, F. Lefloch, and S. D. Franceschi, “Germanium quantum-well josephson field-effect transistors and interferometers,” *Nano Letters*, vol. 19, no. 2, pp. 1023–1027, Oct. 11, 2018. DOI: [10.1021/acs.nanolett.8b04275](https://doi.org/10.1021/acs.nanolett.8b04275).
- [181] T. M. Lu, L. A. Tracy, D. Laroche, S.-H. Huang, Y. Chuang, Y.-H. Su, J.-Y. Li, and C. W. Liu, “Density-controlled quantum hall ferromagnetic transition in a two-dimensional hole system,” *Scientific Reports* 7, 2468 (2017), vol. 7, no. 1, Jun. 7, 2017. DOI: [10.1038/s41598-017-02757-2](https://doi.org/10.1038/s41598-017-02757-2).
- [182] P. K. Lam and S. M. Girvin, “Liquid-solid transition and the fractional quantum-hall effect,” *Physical Review B*, vol. 30, no. 1, pp. 473–475, Jul. 1984, ISSN: 0163-1829. DOI: [10.1103/physrevb.30.473](https://doi.org/10.1103/physrevb.30.473).
- [183] K. Yang, F. D. M. Haldane, and E. H. Rezayi, “Wigner crystals in the lowest landau level at low-filling factors,” *Physical Review B*, vol. 64, no. 8, May 8, 2001. DOI: [10.1103/physrevb.64.081301](https://doi.org/10.1103/physrevb.64.081301).
- [184] E. Fradkin and S. A. Kivelson, “Liquid-crystal phases of quantum hall systems,” *Physical Review B*, vol. 59, no. 12, p. 8065, 1999. DOI: [10.1103/physrevb.59.8065](https://doi.org/10.1103/physrevb.59.8065).
- [185] A. Schmeller, J. P. Eisenstein, L. N. Pfeiffer, and K. W. West, “Evidence for skyrmions and single spin flips in the integer quantized hall effect,” *Physical Review Letters*, vol. 75, no. 23, pp. 4290–4293, Jun. 28, 1995. DOI: [10.1103/physrevlett.75.4290](https://doi.org/10.1103/physrevlett.75.4290).

- [186] E. H. Aifer, B. B. Goldberg, and D. A. Broido, “Evidence of skyrmion excitations about $\nu=1$ in n-modulation-doped single quantum wells by interband optical transmission,” *Physical Review Letters*, vol. 76, no. 4, pp. 680–683, Jul. 18, 1995. DOI: [10.1103/physrevlett.76.680](https://doi.org/10.1103/physrevlett.76.680).
- [187] H. Zhou, H. Polshyn, T. Taniguchi, K. Watanabe, and A. F. Young, “Solids of quantum hall skyrmions in graphene,” *Nature Physics*, vol. 16, no. 2, pp. 154–158, Dec. 2019. DOI: [10.1038/s41567-019-0729-8](https://doi.org/10.1038/s41567-019-0729-8).

A. LIST OF QUANTUM WELL (QW) WAFERS USED IN THIS THESIS

Table A.1. List of samples used in this thesis.

Sample	n 10^{11}cm^{-2}	μ $10^6\text{cm}^2/\text{Vs}$	Spacer nm	depth nm	$\Delta B^*/\Delta B_{2/3}$
LE24	1.6	4.1	70	135	1
LE25	1.3	3.8	110	135	0.14
LE27	0.5	1.6	220	135	0.5
LE39	0.8	3.7	270	185	0.7
LE40	0.8	5	160	135	0.25

$\Delta B^*/\Delta B_{2/3}$ indicates the ratio of the width of spin transition to the width of the whole $\nu = 2/3$ quantum plateau.

B. DETAILED PROCESS OF DEVICE FABRICATION FOR WAFER A (LE40)

Mesa etching:

We etched the cap layer of sample by ~ 130 nm using a so-called deep-etching solution which consists of:

H_2O : 1000 ml

H_2O_2 : 8 ml

H_2SO_4 : 1 ml

This solution led to the following etching rates:

GaAs: 40 nm/min

AlGaAs: 60 nm/min

Contact etching:

Prior to the contact evaporation, we removed the possible residue of photo-resist by O_2 plasma in few seconds. Then we cleaned sample with and HCl or we first etched away ~ 80 nm at the position of the contacts followed by immediate cleaning with HCl for assuring diffusion of thinner contact material down to the QW.

Ni/Ge/Au contact evaporation:

The Ni/Ge/Au contacts were evaporated by using e-beam or thermal evaporator in the following order:

E-beam evaporator

Ni: 30 nm, Rate: 1.2 nm/min

Ge: 50 nm, Rate: 1.2 nm/min

Au: 100 nm, Rate: 1.2 nm/min

Thermal evaporator

Ni: 30 nm, Rate: 0.6 nm/min

AuGe alloy (weight ratio: Au:Ge = 88:12): 150 nm, Rate: 1.2 nm/min

The saw-tooth shape contacts (see Figure. 2.1) increase the area connecting the 2DEG with the contacts. Contacts are formed by annealing in a $H_2/N_2(10\%/90\%)$ atmosphere at $T = 450^\circ C$ for 240 s – 450 s.

Oxide growth 1:

Al_2O_3 was grown by atomic layer deposition (ALD) at $T = 250^\circ C$ using standard recipe.

Al_2O_3 : 50nm

The break down voltage for this thick oxide layer is $\sim 35V$

Front gate 1:

A thin 10 nm of Ti gate was evaporated at a rate of 0.1 nm/s.

10 nm Ti followed by 60.0 nm Au were used for bonding the sample to a chip carrier.

Oxide growth 2:

Al_2O_3 was grown by atomic layer deposition (ALD) at $T = 250^\circ C$ using standard recipe.

Al_2O_3 : 50nm

Remove of oxide for bonding sample:

The total thickness of Al_2O_3 grown on the sample was 100 nm in the end. This thick oxide layer can not be penetrated during wire bonding operation. We used oxide etching solution which consists of:

Buffered oxide etch (BOE) or buffered HF: 10ml

Deionized (DI) water: 50ml

The etching rate for oxide layer is ~ 20 nm/min.

A optical photoresist AZ1518 was used as a protection mask. Before etching oxide layer, we hard baked the photoresist at $T = 90^\circ C$ in oven for at least 2 hours.

Front gate 2:

A thin 10 nm of Ti gate was evaporated at a rate of 0.1 nm/s.

10 nm Ti followed by 60.0 nm Au were used for bonding the sample to a chip carrier. Contact pads area were also covered with Ti/Au at the same time for wire bonding.

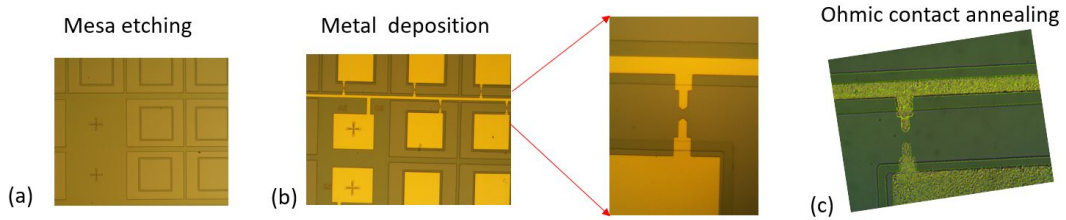


Figure B.1. Sample pictures during device fabrication for Ohmic contacts test: (a) Photo after mesa etching. (b) Photo after Ni/Ge/Au e-beam evaporation. (c) Photo after annealing contacts.

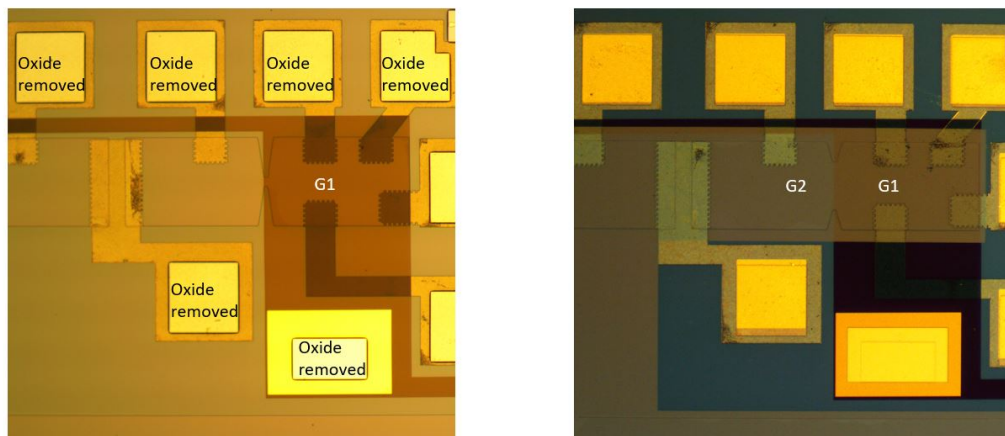


Figure B.2. Sample pictures during DW device fabrication after the second ALD growth: Left: Photo of device after BOE etching. The Al_2O_3 was removed by using BOE for bonding samples. Right: Photo of a completed device.

C. DETAILED PROCESS OF DEVICE FABRICATION FOR *EuSe*/*Bi₂Se₃*/Sapphire

Mesa etching:

We etched all layers down to sapphire substrate by ~ 40 nm in 200 s using Ar ion milling technique with the following parameters:

Ar (100 %) at a total pressure of 1.1 mTorr

Cathode filament current: 3.47 A

Discharge current and Discharge voltage: 0.70 A and 55 V

Beam current and Beam voltage: 36 mA and 400 V

Accelerator current and Accelerator voltage: 0 mA and 0 V

This recipe led to the following etching rates:

EuSe: 0.16 nm/s

Bi₂Se₃: 1 nm/s

Polymethyl methacrylate (PMMA): 0.5 nm/s

PMMA was used as a protection layer with ~ 500 nm thick. The total accumulated charge is $< 600\mu C$. PMMA was not "burned" and easy to be removed by acetone after Ar ion milling.

Contact pattern:

After mesa etching, small area of epilayers was left on top of sapphire substrate. Sapphire is super insulating and need to be coated with additional conductive polymer (aquaSAVE) for e-beam lithography.

Contact etching:

Prior to the contact evaporation, we removed the whole insulating *EuSe* layer by Ar ion milling.

Ti/Au or Nb/NbN contact evaporation:

The Ti/Au contacts were evaporated by using thermal evaporator in the following order:

Ti: 10 nm, Rate: 0.6-0.9 nm/min

Au: 70 nm, Rate: 1.2 nm/min

The Nb/NbN contacts were deposited by DC magnetron sputtering in the following order:

Nb: 10 nm, Rate: 1.8 nm/min

NbN: 15 nm, Rate: 1.8 nm/min

Nb (NbN) was sputtered in Ar (Ar/N₂ (85%/15%)) plasma at a total pressure of 2 mTorr.

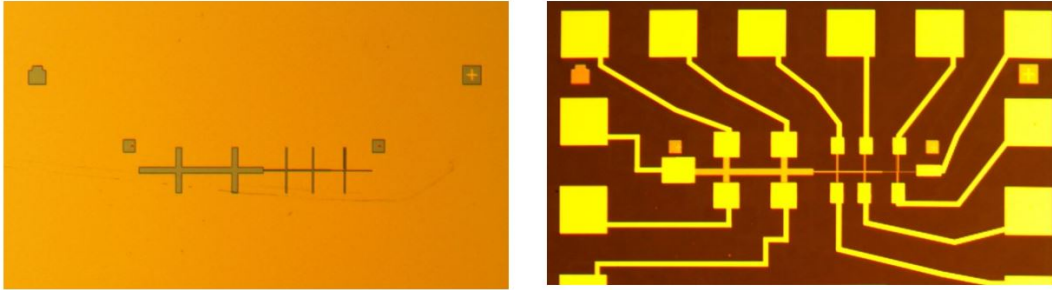


Figure C.1. Sample pictures during device fabrication: Left: Mesa etching pattern. A Hall bar geometry is patterned using e-beam lithography. Right: Completed Hall bar device with Ti/Au contacts.

VITA

Ying Wang

Department of Physics and Astronomy, Purdue University, 525 Northwestern Avenue, West
Lafayette, IN, 47906, USA

Education

Ph.D. Degree Program (2016-2021), Department of Physics, Purdue University, USA

M.S. Degree Program (2013-2016), Department of Physics, Florida State University, USA

B.S. Degree Program (2008-2013), Department of Physics, Shanghai Jiaotong University,
China

Employment

2017-2021 Research Assistant, Department of Physics, Purdue University

2016-2017 Teaching Assistant, Department of Physics, Purdue University

2014-2016 Research Assistant, Department of Physics, Florida state University

2013-2014 Teaching Assistant, Department of Physics, Florida state University

Publications

1. Ying Wang, Vadim Ponomarenko, Kenneth W. West, Kirk Baldwin, Loren N. Pfeiffer, Yuli Lyanda-Geller, and Leonid P. Rokhinson, Transport in helical Luttinger liquids in the fractional quantum Hall regime, submitted to Nature Communications (2021).

2. Ying Wang, Xinyu Liu, Seul-Ki Bac, Jacek K. Furdyna, Badih A. Assaf, Maksym Zhukovskiy, Tatyana Orlova, Neil R Dille, and Leonid P. Rokhinson, Epitaxial growth and magnetic characterization of EuSe thin films with various crystalline orientations, submitted to Physics review materials (2021).

3. Michele Kotiuga, Zhen Zhang, Jiarui Li, Fanny Rodolakis, Hua Zhou, Ronny Sutarto, Feizhou He, Qi Wang, Yifei Sun, Ying Wang, Neda Alsadat Aghamiri, Steven Bennett Hancock, Leonid P. Rokhinson, David P. Landau, Yohannes Abate, John W. Freeland, Riccardo Comin, Shriram Ramanathan, and Karin M. Rabe, Carrier localization in perovskite nikelates from oxygen vacancies, PNAS article 201910490 (2019).

4. Y. Shao, Z. Sun, Y. Wang, C. Xu, R. Sankar, A. J. Breindel, C. Cao, M. M. Fogler, Optical signatures of Dirac nodal lines in NbAs₂, PNAS 116 (4) 1168-1173 (2019).

5. Tailung Wu, Zhong Wan, Aleksandr Kazakov, Ying Wang, George Simion, Jingcheng Liang, Kenneth W. West, Kirk Baldwin, Loren N. Pfeiffer, Yuli Lyanda-Geller, and Leonid P. Rokhinson, Formation of helical domain walls in the fractional quantum Hall regime as a step toward realization of high-order non-Abelian excitations, Phys. Rev. B 97, 245304 (2018).

6. Ying Wang, Guoyu Luo, Junwei Liu, R. Sankar, Nan-Lin Wang, Fangcheng Chou, Liang Fu, Zhiqiang Li, Observation of ultrahigh mobility surface states in a topological crystalline insulator by infrared spectroscopy, Nature communications 8 (1), 1-8, (2017).

7. Xiao-Xiao Zhang, Ting Cao, Zhengguang Lu, Yu-Chuan Lin, Fan Zhang, Ying Wang, Zhiqiang Li, James C Hone, Joshua A Robinson, Dmitry Smirnov, Steven G Louie, Tony F Heinz, Magnetic brightening and control of dark excitons in monolayer WSe₂, Nature nanotechnology 12 (9), 883-888, (2017).